SINGLE PION PRODUCTION
IN
INTERMEDIATE ENERGY K^+d INTERACTIONS

by

ABUL KALAM MUHAMMAD AZHARUL ISLAM

A thesis submitted for the degree of
Doctor of Philosophy of the University of London

Department of Physics
Imperial College of Science
and Technology
London S.W.7 2BZ

October 1972.

ABSTRACT

The present study describes a deuterium bubble chamber experiment, together with technique of film analysis involving the automatic selection of GRIND hypotheses using the bubble density information obtained by HPD.

The results of an analysis of single pion production in K^+d interactions at 2.2 and 2.45 GeV/c based on $\sim$10% of the entire data are presented. Total channel cross sections for K^+N interactions are extracted from K^+d interactions. Each of the final states is found to be dominated by $K^*(892)$ production — whereas $\Delta^{++}(1230)$ is produced strongly only from the pure T=1 isospin state. Resonance production cross sections and other resonance parameters are obtained with the aid of Maximum Likelihood technique.

The Legendre polynomial coefficients are obtained from the production angular distributions of the resonances by the method of moments. The differential cross sections and the decay angular distributions are measured. Vector exchange (ω) dominates charged K^{*+} — whereas neutral K^{*o} is produced mainly via pion exchange. Some study of the asymmetry of the decay distribution of the $(K^+\pi^-)$ system from $K^+n \to K^+\pi^-p$ is made. The production and decay of $K^{*o} \to K^+\pi^-$ are compared with different refined one pion exchange models and an adequate description is obtained with such models atleast at small momentum transfer. The reaction $K^+n \to K^{*o}p$ is compared in some detail with the line reversed reaction $K^-p \to \bar{K}^{*o}n$. Production of K^* from the isospin 0 K^*N state is also discussed.

The production and decay of Δ^{++} are also studied and the predictions of the Stodolsky-Sakurai ρ-exchange model are compared with the data.

CONTENTS

FIGURE CAPTIONS

1. Data processing system.
2. Variation of bubble density of beam tracks as a function of x-coordinate of interaction vertex.
3. Bubble density χ^2 fit probability distribution.
4. 400 bubble density decisions between a π and a proton as a function of momentum of track.
5. Selection efficiency as a function of momentum of track.
6. 337 bubble density decisions between a π and a K-meson as a function of momentum of track.
7. 174 bubble density decisions between a K-meson and a proton as a function of momentum of track.
8. Properties of deuteron wavefunctions; (a) spatial distribution and (b) form factor from Hulthèn wavefunction. (c) Spectator momentum distributions from Hulthèn and McGee function.
9. Scatter plot of proton momentum versus neutron momentum for the reaction $K^+d \rightarrow K^0\pi^+pn$.
10. (a,b) Spectator proton momentum and angular distributions for the reaction $K^+n(p) \rightarrow K^+\pi^-p(p)$ at 2.2 GeV/c. Visible spectator momentum distribution for c) backward and d) forward spectators from the same reaction. The curve shown on each momentum distribution is the prediction of the Hulthèn wavefunction.
11. Spectator nucleon momentum and angular distributions for the reactions (a) $K^+n(p) \rightarrow K^0\pi^0p(p)$, (b) $K^+n(p) \rightarrow K^0\pi^+n(p)$ and (c) $K^+p(n) \rightarrow K^0\pi^+p(n)$. The shaded events correspond to visible proton spectators and the curves shown are the predictions of the Hulthèn wavefunction.

12. Effective mass distributions for events with a $K^+ - \pi^+$ ambiguity at 2.2 GeV/c. a) $(K^+\pi^-)$ combination when interpreted as $K^+n \rightarrow K^+\pi^-p$, b) $(\pi^+\pi^-)$ combination when interpreted as $\pi^+n \rightarrow \pi^+\pi^-p$.
    Distributions of the square of the missing mass to the c) $K^+\pi^-pp$, d) K^opp, e) $K^o\pi^+p$ and f) $K^o\pi^+p$ systems in the reactions $K^+n(p) \rightarrow K^+\pi^-p(p)$, $K^+n(p) \rightarrow K^o\pi^op$(+neutrals), $K^+n(p) \rightarrow K^o\pi^+n(p)$(+neutrals) and $K^+p(n) \rightarrow K^o\pi^+p(n)$(+neutrals) respectively at 2.2 GeV/c. The shaded area contains multineutral events.
13. Dalitz plots for different single pion production reactions. The boundary of each of the plots corresponds to the mean value of the centre of mass energy.
14. The $(K\pi)$ and $(p\pi)$ effective mass distributions for different single pion production reactions. The curve represents the result of the maximum likelihood fit of the respective Dalitz plot population (see text).
15. Production angular distributions for $K^*(892)$ produced in different reactions. The full curves represent Legendre polynomial fits.
16. Momentum dependence of the first four Legendre polynomial coefficients in the expansion of the production angular distribution of $K^{*+}(892)$ from $K^+p \rightarrow K^{*+}(892)p$.
    The interference due to $\Delta^{++}(1230)$ has little effect on the coefficients.
17. Differential cross section $d\sigma/dt$ for $K^*(892)$ produced in different reactions. The errors shown are statistical. The lines are the results of fits to $A\,e^{Bt}$ to the experimental distributions (see text).

18. Decay angular distributions ($\cos\theta$ and Φ) in the Jackson frame for $K^*(892)$ produced in different reactions. The solid and dashed curves represent the fit with P-wave and (S+P)-waves respectively.

19. a) Asymmetry parameter α of the $(K^+\pi^-)$ system in reaction $K^+n \to K^+\pi^-p$.

    b) $\langle Y_1^0 \rangle$ moments as a function of the $(K^+\pi^-)$ mass of the same reaction.

20. Momentum dependence of the density matrix element ρ_{00} of the K^{*+} $(K^+p \to K^{*+}p)$. Data are shown from this experiment and refs. [9,38,39].

21. σ^+, σ^- evaluated in the Helicity frame for $K^{*0}(892)$ and $K^{*+}(892)$. The curves are free-hand fit to the data.

22. a) OPE diagram and b) the inclusion of the absorption effects in the initial and final states for $K^+n \to K^+\pi^-p$.

    c) $d\sigma/dt$ for $K^{*0}(892) \to K^+\pi^-$. The curves are the predictions of OPEDP, OPEA and ROPE models (see text).

23. t-dependence of the density matrix elements of $K^{*0} \to K^+\pi^-$. The curves are the predictions of OPEA model.

24. a) Momentum dependence of $\sigma(K^+n \to \underset{K^+\pi^-}{K^{*0}}p)$ and $\sigma(K^-p \to \underset{K^-\pi^+}{\bar{K}^{*0}}n)$. The dashed and dotted curves are the predictions of OPEA model for the two reactions respectively. The solid line is obtained with $\sigma = 8.6 \cdot P_{lab}^{-2.15}$. The references of the data used in the plot can be found in ref. [42].

    b) Comparison of ρ_{00} for $K^{*0}(892)$ and $\bar{K}^{*0}(892)$ at different energies. See refs. [41,42,68].

25. a) $\frac{d\sigma}{dt}(K^+N \to K^*N)_{T=0}$ and $\frac{d\sigma}{dt}(K^+n \to \underset{K^+\pi^-}{K^{*0}}p)$. The solid curves are the fits with $d\sigma/dt = A\,e^{Bt}$ as described in the text.

b) $\cos\theta_J$ and c) Φ distributions in the Jackson frame for K^* produced in the T=0 K^*N state. The curves are to aid the eye.

d) Momentum dependence of σ_1 and σ_0. The curves are the fits with $\sigma = A\ P_{lab}^{-n}$ as described in the text.

26. Δ^{++} production angular distribution. The full curves represent Legendre polynomial fits.

27. Momentum dependence of the four Legendre polynomial coefficients in the expansion of the production angular distribution of Δ^{++}.

    The interference due to $K^{*+}(892)$ has little effect on the coefficients.

28. Differential cross section $d\sigma/dt'$ for Δ^{++}. The errors are statistical.

29. Decay angular distributions ($\cos\theta$ and Φ) in the Jackson frame for Δ^{++}. The solid curves represent the fit with P-wave and the dotted lines are the predictions of Stodolsky-Sakurai model.

Dedicated

to

my parents

CHAPTER 1

INTRODUCTION

The recent interest in the study of K^+N interactions is due to revelation a few years back of some structures in K^+p and K^+d total cross sections obtained by counter techniques(1,2). The small structures occur around 1.9 and 2.6 GeV/c in T=1 K^+p and substantial peaks around 1 GeV/c in both T=1 and T=0 K^+N total cross sections. The interpretation of these peaks in terms of s-channel positive strangeness baryon resonances, called Z^*'s would be exotic type — because on quark model classification they would then be required to be members of SU(3) [27] multiplets (e.g. Z_1^*) and antidecuplet $[\overline{10}]$ (e.g. Z_0^*), which can not be formed from three quarks alone (a five quark system is needed to explain such systems). The existence of these so-called 'exotic' resonances in both T=1 and T=0 states would prove fatal to the simple quark model and has thus provided the impetus for exploring this important possibility.

Around the time of observation of the above mentioned structures, there were only few experiments performed in the energy region of interest(3,4,5,6). These are mostly done at single energies in hydrogen bubble chamber and moreover there existed only one K^+d experiment at 2.3 GeV/c(7). Thus for a systematic survey of the K^+N system in the intermediate energy region the present high statistics K^+d experiment was proposed in summer 1967(8). According to the associated proposal, the 'control' exposures were made in hydrogen at similar energies in early 1968 and some of the results have already been published[9]. As reported by such study only $K^+p \rightarrow K^{*+}p$ states show indication of structure in A_4/A_0 Legendre polynomial coefficient of the production angular distribution, ρ_{00} density matrix element and slopes of differential cross sections around 2 Gev/c and all other features of data from 2 to 3 Gev/c show smooth energy behaviour. The authors, however, maintained that these phenomena showing qualitative evidence of s-channel resonance are not of great statistical weight but collectively they may be important.

Only recently results from two independent experiments of low energy K^+d interactions from 0.6 to 1.6 Gev/c have been published[10,11]. The up-to-date information obtained by all the experiments done so far can be summed up by saying that, resonance interpretation for both T=1 and T=0 peaks around 1 Gev/c, while possible, is not a compelling consequence of the data and that they can also be associated with the threshold effects.

However, the situation is still confused and more phase shift analysis with the existing data and new polarization data would hopefully help to clear up the situation both at low and intermediate energies.

The present experiment is a collaborative effort between Imperial College and Westfield College, London. In addition to looking systematically for the above-mentioned effects near the second and third 'Cool bumps' new data from the current high statistics experiment should serve to fill up the gap of knowledge of K^+d physics in the unexplored energy region.

The thesis is organized as follows: chapter 2 describes briefly the data taking and the data reduction procedures. Chapter 3 is devoted to the description of how we utilize the useful HPD bubble density measurements in an effort to automate the selection of GRIND hypotheses together with a discussion of selection efficiencies.

Chapter 4 outlines the techniques for deducing the properties of K^+-N physics from K^+-d interactions and the problems associated with these. Chapter 5 concerns with the measurement of cross section of stable final states whereas chapter 6 deals with the physics of single pion production.

The author took part in data-taking at Rutherford high energy laboratory and contributed personally much to the data processing of the experiment including successful application of the HPD measured bubble density information to achieve the automation of hypotheses selection as far as possible. The analysis of the single pion production is entirely done by the author himself.

CHAPTER 2

EXPERIMENTAL DETAILS

2.1 Data collection at RHEL:

The data for the present experiment were taken in an exposure of the British National 150 cm bubble chamber filled with deuterium to an electrostatically separated K^+ meson beam at Rutherford High Energy Laboratory. A total of 927,000 pictures were taken in three different exposures at nominal beam momenta of 2.2, 2.45 and 2.7 GeV/c. The summary of data-taking is given below in table I.

Table I. Summary of data-taking.

Run	Dates From - To	Momentum (GeV/c)	Number of pictures	Approx. K^+/pic.	Target size(mm^3)
1	21-11-69 30-12-69	2.2	400,000	12-14	Copper 4x4x100
2	12-03-70 5-04-70	2.7	327,000	12-14	
3	9-04-70 20-04-70	2.45	200,000	12-14	

The K^+ beam was produced at a copper target and transported to the bubble chamber in the NIMROD K9 beam. The description of the beam has been given elsewhere[12] and hence will not be repeated here. With 5.6×10^{11} protons per pulse in the X1 beam (X1 which feeds K9 shares the spill with X2 and works at $\sim 25\%$ efficiency) the average number of K^+ particles entering the chamber was about 12-14/pulse. During the exposures frequent checks were made so that the edge of the pion peak was in the same place and background count rate (due to pions and large part due to muons decaying from kaons in the drift space behind the separator) had not increased.

In order to measure the sign of the charge and the momentum of the particles, a 12.32 kilogauss magnetic field was applied across the chamber. Exposures were made on 35 mm film loaded in three cameras at the corners of an isosceles triangle. These were mounted with optic axes horizontal and perpendicular to the chamber windows. Dark field illumination provided by three flash tubes per camera was used. Constant checks on the bubble chamber operating conditions and on the quality of film were made to ensure that these would not present any serious problem for picture digitizing on the HPD (Hough Powell Device is an automatic film measuring machine similar to the so-called HPD2 at CERN) and hence would not affect the automatic selection of GRIND hypotheses on the basis of bubble density measured by HPD.

2.2 Data reduction procedures:

The data reduction procedures of bubble chamber experiments are roughly the same for all experiments. But since the author was actively involved in the day to day processing and since part of our processing system is quite different from previous experiments in this laboratory, a brief account will be given here.

A. Scanning and measuring:

Here we are concerned with only those topologies which include single pion production. All one-prong and two-prong events with a V^0 were scanned. But for non V^0 events we chose to scan only those events which are either clear or possible K^+n/coherent K^+d interactions. Thus for physics reasons only the following categories of events were scanned:

i) all 3-prong events — these are either tau decays or K^+n/coherent K^+d interactions where the spectator protons/deuterons are invisible.

ii) only those 4-prong events where atleast one of the positive secondaries could be identified as a proton/deuteron stopping inside the chamber. At this stage a 20 cm projected length cut-off on this heavily ionizing track corresponding to a spectator proton/deuteron of momentum of $\sim 340/560$ MeV/c was made.

The overall data flow of our adopted processing system is shown in fig. 1 . As is obvious in this self-explanatory figure we had two separate independent scans and a check scan to compare the two scans and the conflicts that were found to exist were resolved before the events were sent to the rough-digitizing table. In this stage, two fixed fiducial marks on each of the three views, the vertex and other two points on each track were measured and stored

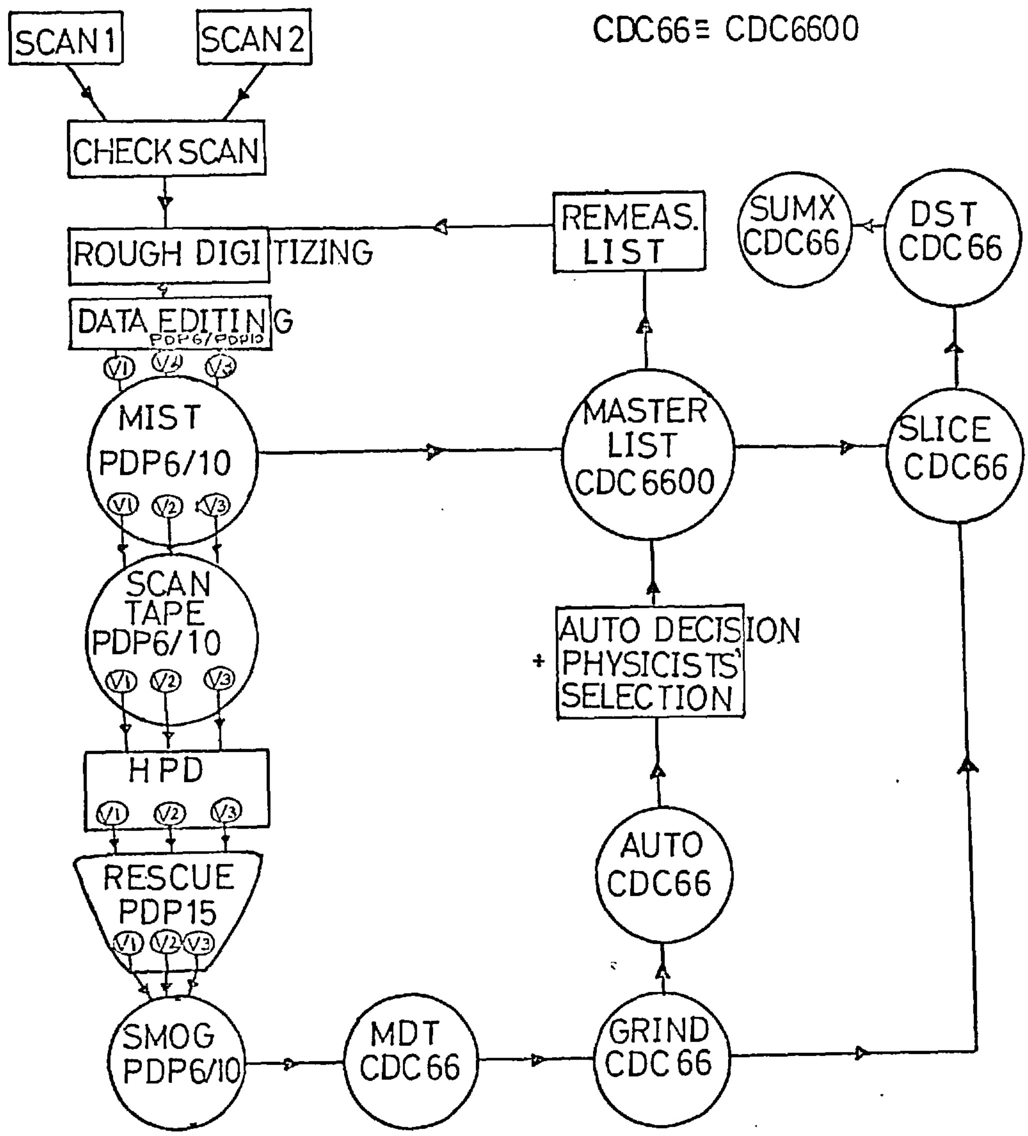
CDC66≡ CDC6600
SCAN 1
SCAN 2
CHECK SCAN
ROUGH DIGITIZING
REMEAS. LIST
SUMX CDC66
DST CDC 66
DATA EDITING PDP6/PDP10
V1 V2 V3
MIST PDP6/10
MASTER LIST CDC 6600
SLICE CDC66
SCAN TAPE PDP6/10
AUTO DECISION + PHYSICISTS' SELECTION
HPD
RESCUE PDP15
AUTO CDC66
SMOG PDP6/10
MDT CDC 66
GRIND CDC 66

FIGURE 1.

in a magnetic tape. Here the ONLINE program constantly checks the measurements and tells the operator when there is any mistake of the road-making. These data were edited and view by view were put on tapes which were subsequently read in by a program called MIST. This program first checks the data and then outputs the information on a scan tape in a format suitable for use by the HPD online program HAZE. MIST rejects an event if the points of a track (road) do not lie approximately on an arc of a circle. Now guided by the scan tape road the HPD, which is online to a PDP6/PDP10 computer of the physics department, scans and digitizes one view at a time so that 3 views of a roll of film are digitized one after another. In doing so it also performs some processing in the sense that it finds fiducial centres and rejects all digitizings that fall outside the circular road defined by the road-maker. The subprogram FILTER using all the digitizations in the road computes about 2 to 20 representative master points on each track depending upon the track length.

It sometimes happens that FILTER fails to give representative master points of a track either because of HAZE failure by confusion or a road badly defined by a human operator at the time of rough-digitization. In this case the program dumps all the necessary information about the track in question onto the output tape. The program RESCUE, which is online to a CRT device, used these output tapes as input. Here the road points of the track in question are displayed on the device and the operator takes appropriate action by means of a 'light pen' to which the program responds when it is applied to the CRT screen. If the operator decides to measure the track, she simply runs the light pen along the true bubble image of the track and on to the 'measure' button by which the program recalculates the master points and ionization of the track independently of the original measurements. The output tapes from RESCUE were then input to the view-merging program SMOG. It merged three tape files of three views onto one tape which then contained information of precision points on tracks and fiducials in all three views together. This output was subsequently processed by the program sequence Mass Dependent THRESH-GRIND-AUTO-SLICE-SUMX.

B. <u>Geometrical reconstruction</u>:

The geometrical reconstruction of charged tracks in space was done by the program Mass Dependent THRESH (MDT), which takes into account the energy loss of the particles in the liquid. The basic technique of reconstruction consists in projecting a five-parameter space curve onto each film-view and varying the parameters in order to minimize the perpendicular distances from the measured points to the projection. Beforethis could be done a first approximation is needed which is obtained by fitting a helix to a set of points in space reconstructed by the method of near corresponding point(13). The fitting procedure takes into account the optical distortions in the chamber lenses , the variation of magnetic field with position in the chamber and of course the energy loss. Histograms of residuals of beam tracks (measured by HPD) show that they peak at 2-3 μm.

The output of MDT consists of parameters which describe the space trajectory of charged track moving in the magnetic field of the chamber — these are space co-ordinates for all vertices, end of stopping tracks with their errors and the curvature ρ, dip angle λ, azimuth Φ at the vertex for each track with their errors, one set per mass assignment successfully tried.

C. GRIND and treatment of spectator proton:

GRIND uses the output tape from MDT as input and for each event performs a series of kinematic fits known as hypotheses, of which for each topology a list is supplied to the program as hypothesis block in titles. For events with failing beam or beam with large residual ($\geqslant 6.0$ μm) information from beam title values was used. The mean value of beam momentum with its error, obtained from previous averaging of raw data, was transformed to the interaction vertex and used as the starting value for the fit of such class of events.

For an even prong event there are four constraints present at each vertex corresponding to the conservation of energy and momenta; hence there is no difficulty in the fitting procedure. For odd prong event where the spectator is unseen, we could fit it by the conventional procedure by considering the proton as unmeasured and obtaining its momentum vector by a fit at the production vertex — this will then be a 1C fit at the production vertex and hence for events like $K^+n(p) \to K^0\pi^+n(p)$ or $K^+n(p) \to K^0\pi^0p(p)$ where there is one neutral particle in addition to the invisible spectator proton, it is impossible to get a fit. In order to overcome the situation, use of Hulthen wavefunction has been made to enlarge the number of constraints in the interaction. Since in the limit the spectator takes no part in the interaction, the mean value of each of the three components of the momentum in the deuteron c.m.s is zero, the program is supplied with a starting value of zero for each of these and an error to include the range of unseen tracks as $P_x = P_y = P_z = 0$; $\Delta P_x = \Delta P_y = \Delta P_z/1.37 = \pm 30$ MeV/c. The larger error on the z-component (z is the direction of camera axis) is used to take into account the fact that along the line of sight the probability of detection is less. The fit is performed in cartesian co-ordinate system to avoid the singularity when $|\bar{p}| = 0$ and finally the results are transformed back to p, λ, ϕ variables.

To judge the goodness of fit a χ^2 was calculated for each hypothesis of an event and the corresponding probability was then calculated using the theoretical χ^2 distribution function for the appropriate number of degrees of freedom.

One of the major tasks of the data reduction system is to minimize the number of kinematic fits obtained in the

GRIND stage. The choicing for best hypothesis or hypotheses was done by AUTOGRIND using bubble density information and procedures for doing so have been described and discussed in the next chapter.

D. Book-keeping, SLICE and DST:

The results of the initial road-making were recorded on a magnetic tape called MASTER LIST tape, thereby generating a short record of each event found during scan and its measuring history. The results of subsequent measurement for each cycle end up at the choicing stage with some selected slice cards corresponding to chosen hypotheses. These cards are then used to update the MASTER LIST from which one can determine the status of any given event at any time. The program SLICE uses either the slice cards or this list to pick off the necessary information from the GRIND Library Tape (GLT) to put on the Data Summary Tape (DST).

E. Remeasures and Rejects:

At the updating stage the MASTER LIST is also used to create a list of remeasures for the next cycle of measurements. All remeasurements were done on conventional measuring machines. An event is sent for remeasurement if one or more tracks failed to reconstruct or if no satisfactory kinematic fit was obtained. If it was decided that the event should not be included in subsequent analysis, it was rejected and some of the reasons are as follows:

UNMEASURABLE: the event can not be measured because the film is damaged between scanning and road-making or torn at some later stages, obscured by flares, or the like.

NON-BEAM EVENT: from the y-position in the chamber and measured momentum, the beam is classed as OFF beam.

NO EVENT: the event can not be located, but chance configuration of track simulates event or the event is secondary and primary is outside fiducial volume or the V^0 is not associated with the primary vertex.

WRONG-TYPE: K^+ is recognizable by ionization in one or two-prong topology with a V^0.

In addition to these, there are some well measured V^0 events whose V^0 does not fit a K^0_S or Λ^0 decay. Some of these may be unrecognized e^+e^- pair (but do not get a gamma materialization fit) and 3-body decay of K^0_L. If they failed on remeasurement, they were discarded.

CHAPTER 3

UTILIZATION OF HPD BUBBLE DENSITY MEASUREMENT

3.1 Introduction:

The conventional method of choosing the correct hypothesis among the several possible hypotheses of the bubble chamber events is manual inspection by a physicist on a scan table - where he eye-estimates the bubble density of a track by looking at the event and then compares this estimate with the expected value calculated from the velocity of the particle. But this eye estimation is slow and inaccurate and hence for a large bubble chamber experiment involving millions of pictures (like ours of ~ 1 million) this work alone may take months even years of physicist's time. Thus the need for using the additional information of the blackness of a track automatically and making the identification after kinematics automatic. The HPD at Imperial College physics department came into operation only in early 1969 and was doing K^+p experiment but no effort was made to use the bubble density information. The volume of the present K^+d experiment necessarily called for this automation. The author was entirely responsible for establishing the K^+d version of the bubble density fitting program AUTOGRIND by effecting all necessary changes to the existing CERN version and also adapting it to our system of analysis different from the CERN system as far as data flow from GLT to DST is concerned. So a brief account will be given here about how the bubble density information was utilized for correct mass assignments and the factors affecting the reliability of information together with a discussion of quality of information.

3.2 Bubble density fitting and hypothesis selection:

The bubble density of a track, k is calculated using the Strand's formula[14]:

$$\frac{M}{T} = \frac{T - H}{T} = e^{-ka/\cos\alpha} \qquad (3\text{-}1)$$

where T = total number of times the track is traversed by the HPD flying spot,

H = number of times the spot is sufficiently obscured to produce a digitizing (hit) on the track; M = T - H,

α = angle between the track and perpendicular to the scan direction,

and a = effective scan width approximately equal to the sum of the diameters of the spot and the bubble image which under usual condition ~40-50 μm.

The value of 'a' varies with the size and shape of the bubble which in turn depends on the operating condition of the chamber and also may vary with the position in the chamber. Another factor which may change 'a' is the track centre circuit. Thus in order to get consistent result for bubble density, one must keep an eye on the factors which make them unstable with time and space.

The program FILTER using HPD measurements of M, α calculates 'ka' along with errors for each track-view[15]. These are then transmitted to the GLT to be input to AUTOGRIND which then performs the bubble density fitting. The predicted bubble density of a track of velocity 'β' is proportional to β^{-2} and hence ka = α^o/β^2. This then allows one to write

$$\frac{M}{T} = e^{-\alpha^o/cg\beta^2} \qquad (3\text{-}2)$$

where α^o = normalization factor to be fitted for each event and on each view, g = geometrical correction factor which accounts for the demagnification of the spot and depends on the position in the chamber and c = correction for track not perpendicular to the scan direction.

To take into account the deviations of the bubble density measurements from that predicted by (3-2), a correction is applied to the above formula. This view-dependent correction factor 'v' is restricted to lie between 0.0 and 0.05 which ensures that the correction does not exceed 5% of the number of hits predicted. In the minimization 'M/T' is used as variable, rather than 'ka'. For each hypothesis and for each view the following χ^2 function is minimized with respect to α^o and v:

$$\chi^2 = \sum_{j=1}^{\text{TRK}} \left[\frac{(M/T)^m_{ij} - (M/T)^p_{ij}(\alpha^o_i,\ v_i)}{1.5 \times \delta\ (M/T)_{ij}} \right]^2 \qquad (3\text{-}3)$$

The factor 1.5 multiplying the error in the denominator is used to get a correct width of 'M/T' pull distribution[16].

From the minimum χ^2 found and the number of degrees of freedom, the corresponding probability of the fit is calculated for each view. The product of the probabilities of the three views, P_k is then calculated for each hypothesis for an event and a hypothesis is selected if $P_k \geqslant P_{max}/8$, where P_{max} is the maximum of P_k's of a given event. The empirical factor 8 is determined by the compromise between the number of wrong and ambiguous decisions and perhaps losing the correct decision. This selection procedure is not the only one - alternatively one can use the single view fit and calculate an overall χ^2 for the 3 views and hence an average probability for each hypothesis in order to compare the probability for different hypotheses to select the best one. Indeed this procedure was used by P.Duinker[17] who concludes that the result obtained by this method and single view fit probabilities are similar. Skillicorn[18] finds that the correlation between the fit probabilities for two views ~0.3 which indicates that ~10% (on the average) of the variance of the fit probability on one view can be related to the probability of the fit on another view; so according to him the measurement of each view gives independent measurement of the event to a good approximation.

The main reason for not using the beam track density in the fit for normalization is due to the fact that there are frequently overlapping beams on one or more views giving much higher bubble density. Thus in order to safeguard against this the beam has been left out. But beam track information will certainly be valuable if one takes precautions and applies some sophisticated tests before using it.

3.3 Quality of bubble density information:

In the following paragraphs we shall discuss the quality of bubble density information, some of the problems associated with their measurements, selection efficiencies between various mass assignments on the basis of bubble density information alone and some comments on the automatic selection of the hypotheses in the present experiment.

First to see whether there is any significant systematic variation of bubble density measurements in different regions of bubble chamber, we have shown in fig.2 the measured values of 'ka' of beam tracks as a function of x-coordinates of the interaction vertices of events for three views (this is the only set of data which were obtained by keeping the HPD digitizing level constant). The distributions of 'ka' obtained by projection of these scatter plots (not shown) are roughly Gaussian. Inspite of smaller statistics it is apparent from fig.2 that the beam track measures lighter in view 1 than in view 2 or view 3.

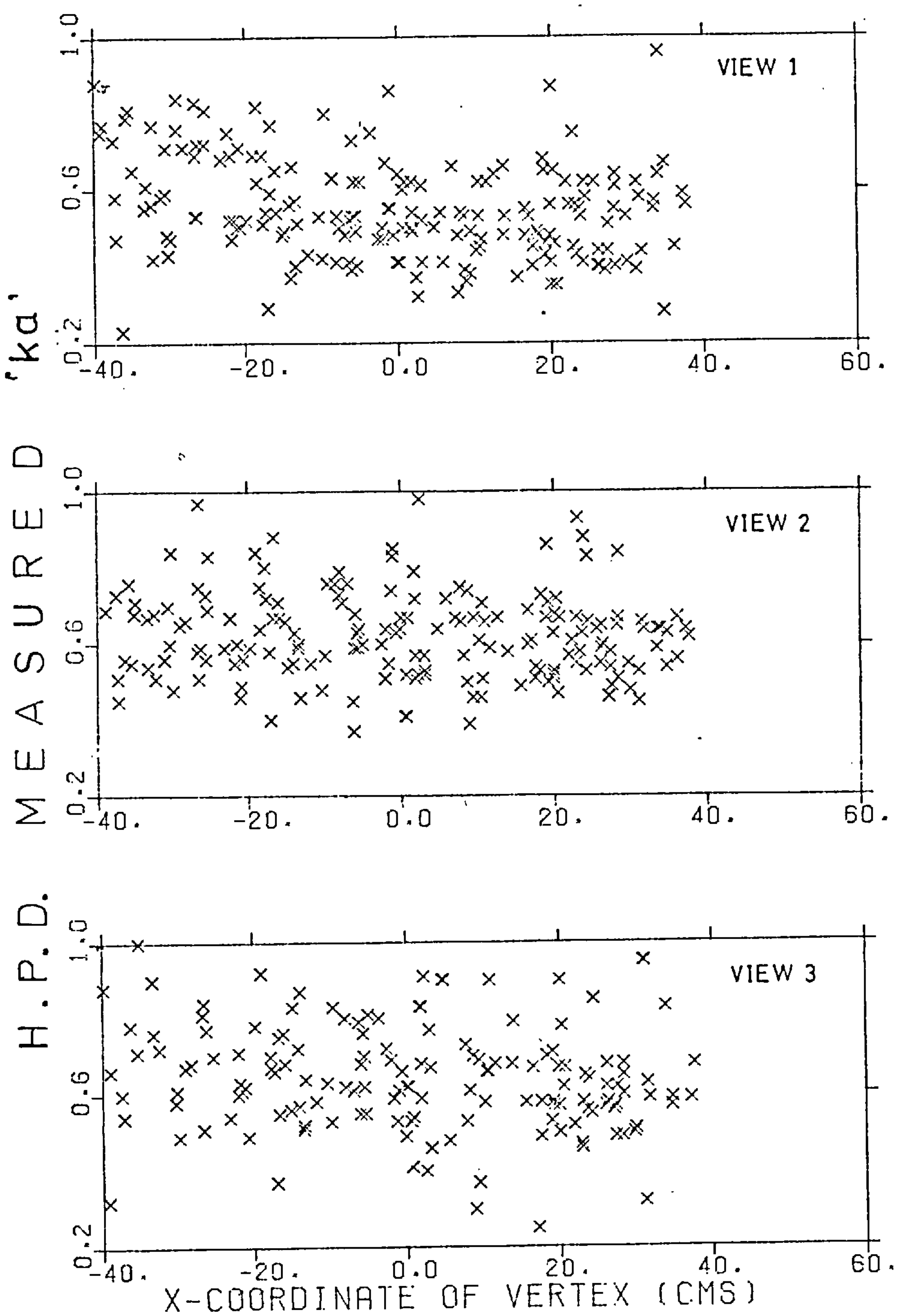
VIEW 1
VIEW 2
VIEW 3
H.P.D. MEASURED D 'ka'
1.0
0.6
0.2
-40.
-20.
0.0
20.
40.
60.
X-COORDINATE OF VERTEX (CMS)

FIGURE 2.

on view 2 the measurement looks better than the other two views. Also the bubble densities for beams having interaction points in $-40 \leqslant x \leqslant -15$ cm are not as good as those of beams having interaction points in $-15 \leqslant x \leqslant 40$ cm. In the first region the beam measures heavier than the second region - which is particularly seen on view 1. These may be due to the intensity of the region and also due to the short length of beam available. The difference in bubble chamber conditions arising from different expansions in different regions may also be responsible for these. The overall effect of poor film quality, intensity variation of HPD scan regions and some combinations of HPD and bubble chamber conditions may give rise to some systematic errors in track density measurements. The variation of effective bubble size has been shown to be correlated with the intensity of the spot(18). Skillicorn(18) again pointed out that in the central region of the scan lines there are no great systematic differences between normal and abnormal scans.

Figs 3a,b,c show the bubble density χ^2 fit probability for some 227 fits of 3- and 4-prong events to four constrained hypotheses and fig. 3d,e,f, the same distributions for 270 1C events for three views respectively. All the distributions are consistent with being flat.

In determining the selection efficiency, we have used only the bubble density fit results and other additional information has been ignored. In practical case, however, we

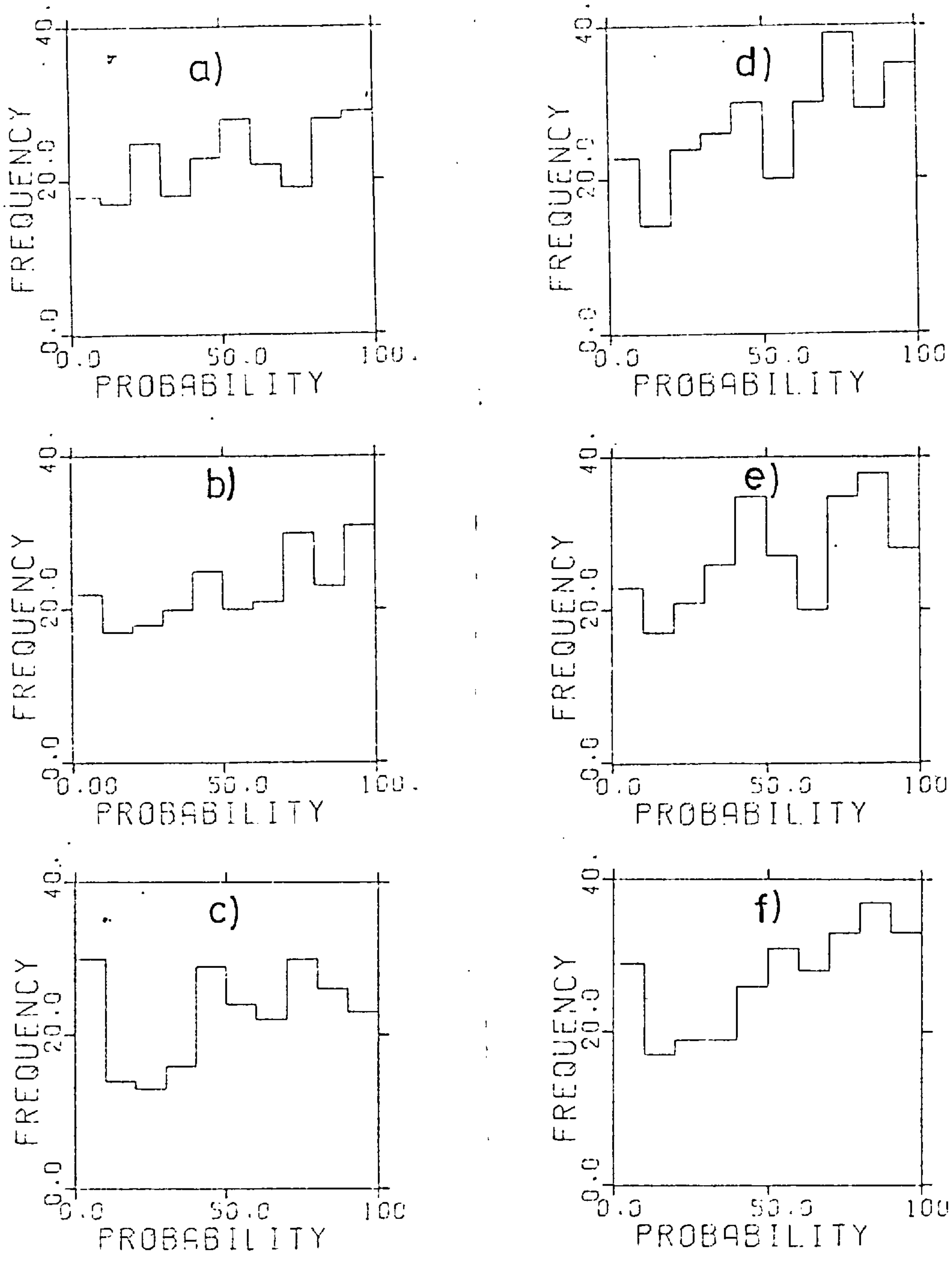

FIGURE 3.

have utilized other information like MM^2 cuts, kinematic probability cut, 4C fit fit preferred etc in order to further minimizing the ambiguities left after ionization decisions.

Consider that we know the particle configuration of an event as:

$$\begin{array}{cccccc} A1 & T & A2 & A3 & A4 & A5 \\ K^+ & d & \rightarrow p & p & K^+ & \pi^- \end{array} \qquad (A)$$

If we change the mass of the track A3 to π, the hypothesis becomes:

$$K^+ d \rightarrow p\ \pi^+\ K^+\ \pi^-\ n \qquad (B)$$

Now if we apply the same selection criteria as used with the hypothesis A, then we can test the reliability of the fitting procedure. If the program chooses only A or only B or both on the basis of bubble density fit results alone, then we call the decisions as good, wrong or ambiguous respectively. In order to study the reliability of the selection as a function of track momentum, we define the selection efficiency, e(P) as the number of good decisions to the total number of decisions (good+wrong+ambiguous) in the momentum interval. Fig. 4 shows the comparison between π and p for 400 tracks. The vertical line is the eye-level (i.e. momentum, P = 1.5 Gev/c for π and p tracks). Below this about 89% of the cases, pions can be distinguished from protons and vice-versa. In fig. 5a is shown the selection efficiency, e(P) as a function of track-momentum. The efficiency is $\sim$95-99% in the momentum interval 0.3 to 0.8

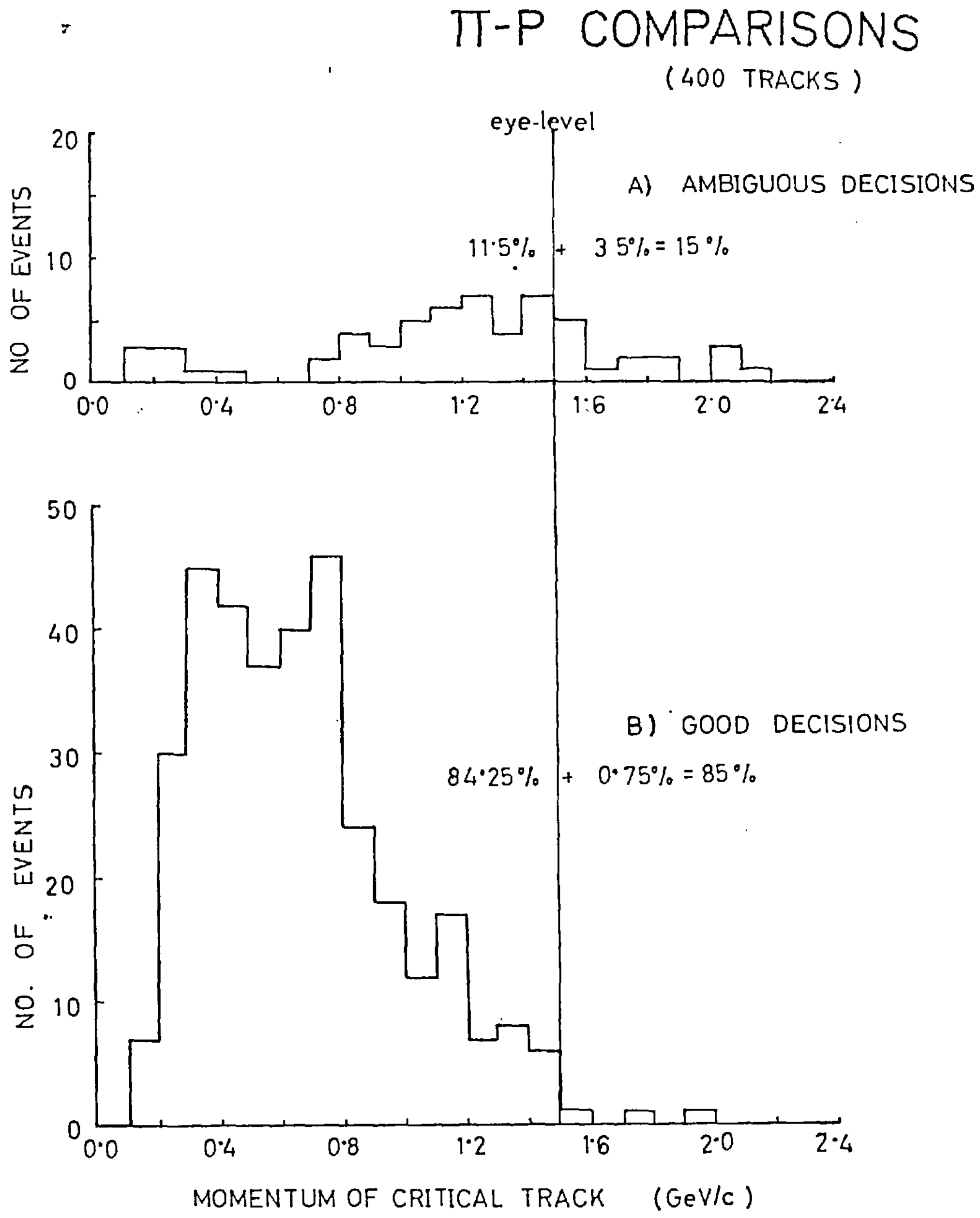
π-P COMPARISONS
(400 TRACKS)
eye-level
A) AMBIGUOUS DECISIONS
11·5% + 3 5% = 15 %
NO OF EVENTS
0 10 20
0·0 0·4 0·8 1·2 1·6 2·0 2·4
B) GOOD DECISIONS
84·25% + 0·75% = 85 %
NO. OF EVENTS
0 10 20 30 40 50
0·0 0·4 0·8 1·2 1·6 2·0 2·4
MOMENTUM OF CRITICAL TRACK (GeV/c)

FIGURE 4.

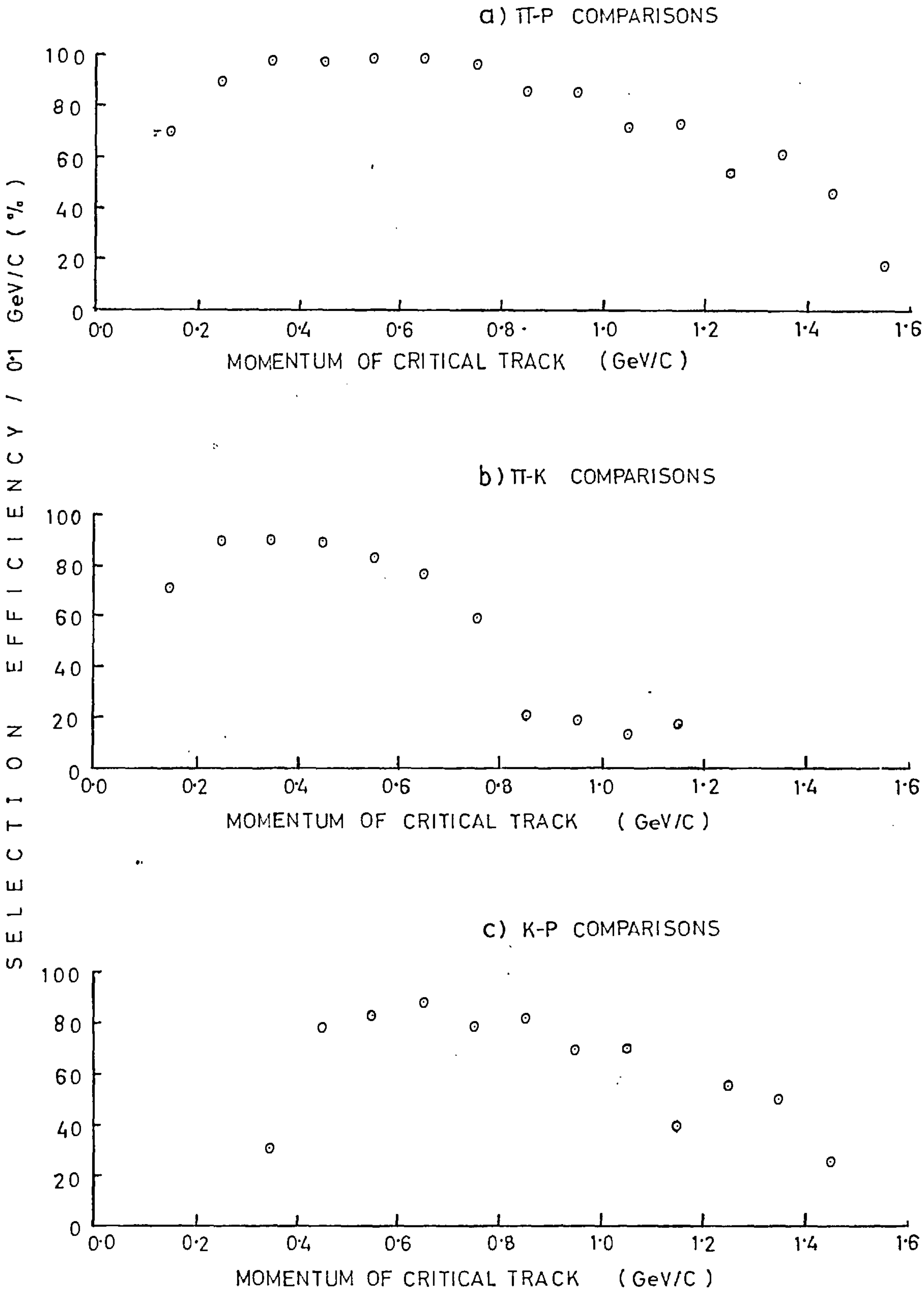
a) π-P COMPARISONS
b) π-K COMPARISONS
c) K-P COMPARISONS
SELECTION EFFICIENCY / 0·1 GeV/C (%)
MOMENTUM OF CRITICAL TRACK (GeV/C)
0·0
0·2
0·4
0·6
0·8
1·0
1·2
1·4
1·6
0
20
40
60
80
100

FIGURE 5.

GeV/c and from 0.8 to 1.5 GeV/c, it drops to ~50% starting from ~90%. In the sample studied for this purpose there was no single case of a wrong decision while distinguishing between π and p . Fig. 6 shows 337 decisions between π and K mesons as a function of momentum of track. Between 0.1 GeV/c and 0.8 GeV/c, in 133 of total 166 cases pions can be distinguished from kaons or vice-versa i.e. on average ~80% good decisions between 0.1 GeV/c and right upto the level where the bubble density difference between a π and a K meson is 40% . But above 0.8 GeV/c where this difference is less than 40%, the number of ambiguities in distinguishing a π from a K meson increases rapidly. This can also be seen from e(P) v.s. 'P' plot (fig. 5b) for π-K comparisons that the efficiency falls to ~20% .

For kaon-proton comparisons, we plot the decisions as a function of track-momentum in fig. 7 and the selection efficiency in fig. 5c . Below 0.4 GeV/c we can not unambiguously identify a kaon and a proton in ~70% of the total cases studied. The low efficiency ($\lesssim$30%) below 0.4 GeV/c is caused by a saturation effect which is due to the fact that the HPD and FILTER see a few gaps on a track left by a K-meson or a proton of momentum less than 0.4 GeV/c. Also the selection efficiency drops below 60% when the K-meson or the proton is in 1.1 GeV/c region or above.

We noted earlier that the selection of the best hypothesis is done not only by the bubble density fit results but also by some additional experiment dependent rules.

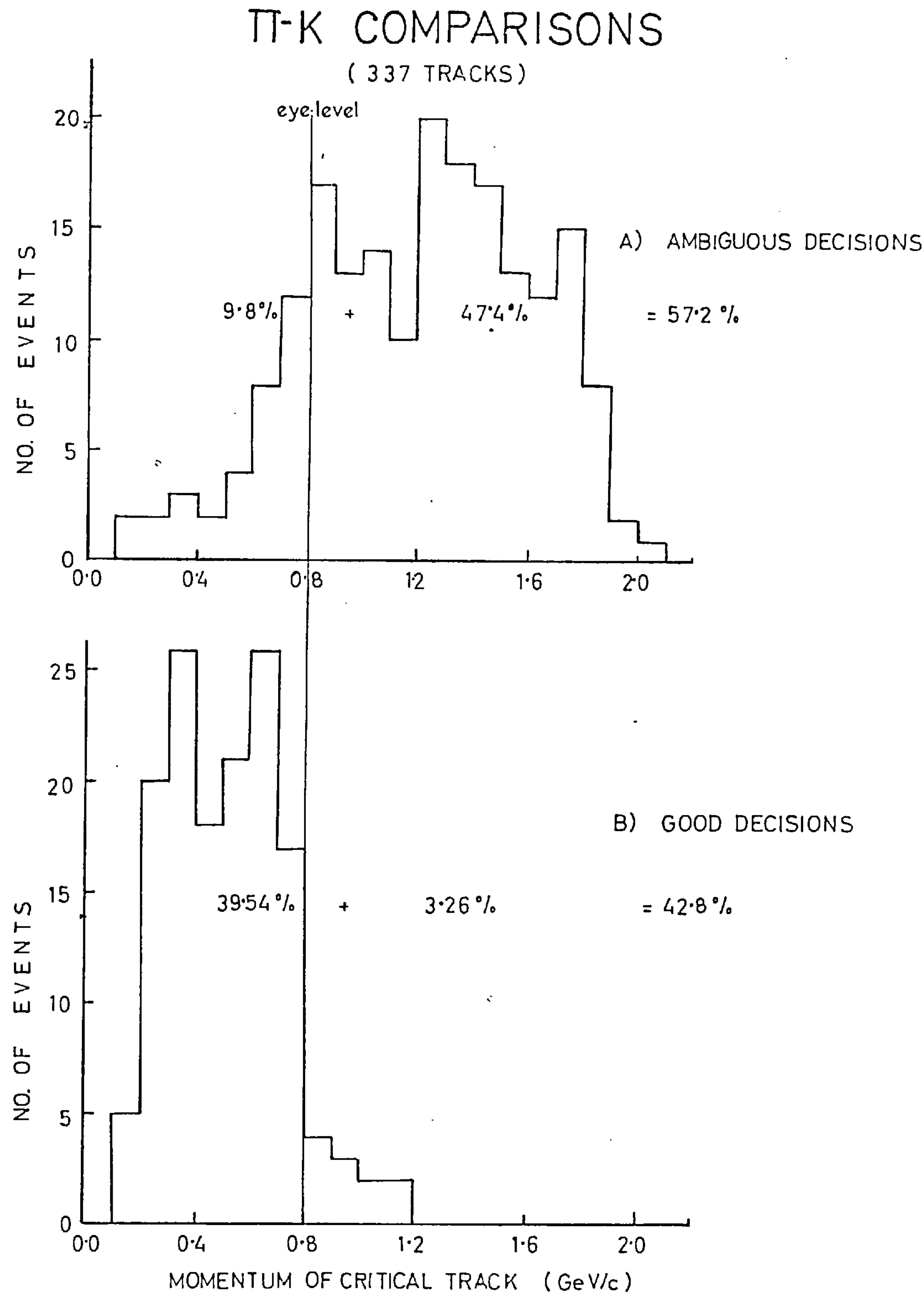

π-K COMPARISONS
(337 TRACKS)
eye-level
A) AMBIGUOUS DECISIONS
9·8%
+
47·4%
= 57·2 %
B) GOOD DECISIONS
39·54 %
+
3·26 %
= 42·8 %
NO. OF EVENTS
0
5
10
15
20
25
0·0
0·4
0·8
1·2
1·6
2·0
MOMENTUM OF CRITICAL TRACK (GeV/c)

FIGURE 6.

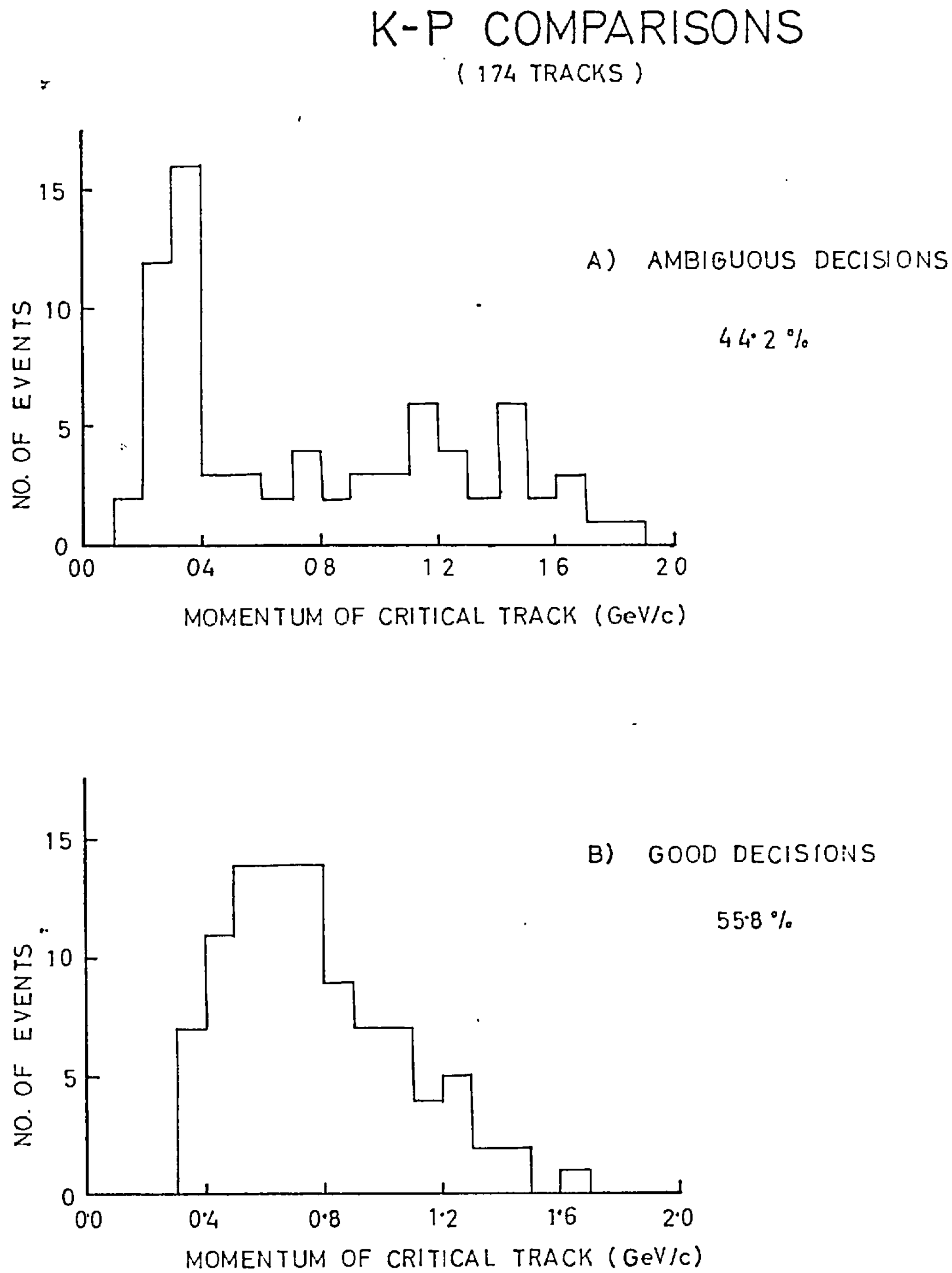
K-P COMPARISONS
(174 TRACKS)
A) AMBIGUOUS DECISIONS
44·2 %
NO. OF EVENTS
0
5
10
15
00
04
08
12
16
20
MOMENTUM OF CRITICAL TRACK (GeV/c)
B) GOOD DECISIONS
55·8 %
NO. OF EVENTS
0
5
10
15
0·0
0·4
0·8
1·2
1·6
2·0
MOMENTUM OF CRITICAL TRACK (GeV/c)

FIGURE 7.

But inspite of this we have found that there remains a sizeable (greater than reported by other experiments[16]) fraction of events which need post-kinematic re-examination on the table to resolve the ambiguities. This is due mainly to following reasons:

a) it is impossible even for a sophisticated co-ordinate digitizing machine like HPD to measure the bubble density of all tracks of all events accurately due to factors which are difficult to control all the time - among these are event-obscurity on the film, crossing tracks or variation in bubble size etc.

b) the above-mentioned reasons are more or less common for every experiment. But the other reason which is typical of K^+d experiment is that we have 4-way ambiguities, namely; $K^+\leftrightarrow\pi^+$, $K^+\leftrightarrow p$, $\pi^+\leftrightarrow p$, $p\leftrightarrow d$ — whereas π^+p or K^-p experiments (in our energy range) have $\pi^+\leftrightarrow p$ (for π^+p expt.); $K^-\leftrightarrow\pi^-$, $\pi^+\leftrightarrow p$ (K^-p expt.) ambiguities only.

In order to see the performance of the program under varying conditions of film and HPD measurements, we have checked every event (irrespective of whether it's a decided or check event) from 20 rolls on the table and found that on the average $\sim 5\%$ of events are wrongly decided- for these we replace the decision by the correct one. This percentage may seem high but one can easily understand it if one sees the difficulty of K^+d experiment where for K^+n or K^+d interactions $\sim 60\%$ of the time there is an unseen particle which is either a proton or a deuteron - this makes the decision between a proton or a pion sometimes difficult. Though the selection efficiency between a proton and a pion is very much higher, a few percent ambiguity is enough to make this level of wrong decisions. Indeed a further study revealed that almost all of the wrong decisions are from 300 topology with an unseen particle giving e.g. $K^+pp\pi^-$, $K^+\pi^+d\pi^-Z^0$, $\pi^+K^+d\pi^-Z^0$, where Z^0 represents more than one π^0. The pions and kaons are relatively fast tracks and due to slightly wrong ionization (caused either by wrong measurement or by tracks affected by being in flashed region of film), the NOFIT type hypothesis is being choiced (i.e. π^+ is chosen over p or else π^+ over K^+ and K^+ over p) in preference to the above 4C type hypothesis. Realizing that at our energy the cross section for 3-pion production with a deuteron is vanishingly small in comparison with the above 4C type hypothesis, we have decided to retain only the 4C deuteron hypothesis in the hypothesis title block - this would reduce the percentage of wrong decisions to a negligible level. Moreover, the program is at present under additional modifications to deal with these and other special deuteron problems.

Considering the number of decided events and check events (the effort needed for a physicist to select from check events is already down to ~30-40% of the original effort that would have been needed - this is because the program already has rejected most of other hypotheses on both ionization and other grounds) we can roughly say that for the same manual work on the scan tables, we shall be able to do the entire K^+d experiment in about less than 1/3 time using bubble density fitting than without it. Moreover, if we had no other reasons except only this for looking at an event on the table we could have further cut down the time needed to finish the experiment.

Finally, it appears obvious from what we have presented and discussed that the use of bubble density fitting for resolving kinematic ambiguities automatically seems to be a successful method and certainly worthwhile in the present experiment.

CHAPTER 4

DEUTERON TARGET AND FREE NUCLEON INTERACTION

4.1 Introduction.

Single nucleon collisions are best studied where free nucleon targets are available. But the difficulty of having a free neutron target has necessitated the use of deuteron as target - which is due to the fact that it has a loose structure consisting of lightly bound neutron and proton mostly in an S-wave. As one can see deuteron target offers the possibility of studying the interactions (a) where the single nucleon is a target and also (b) where the composite nucleus as a whole acts as a target. Understandably extraction of single nucleon interaction from that off the complex deuteron is not an easy task but beset with many difficulties which will be discussed in appropriate sections in the following pages.

4.2 The Impulse approximation:

We shall now describe in brief a method, due to Chew[19] called the Impulse approximation (sometimes called spectator model.) by which we can obtain the relevant information on the interaction of the incident K^+ with a single nucleon of the complex target. For processes in which the wavelength of the incident particle is short compared to the size of the deuteron (i.e. $\lambda_{inc} \ll r_{np}$), the assumptions of the model are: (i) the incident particle interacts with either neutron or proton one at a time, (ii) the amplitude of the incident wave on either nucleon may be approximated by the wave-function of the K^+, incident on a free target nucleon, and (iii) the binding forces between the nucleons in the deuteron can be neglected for the duration of actual interaction.

Thus for processes of the first kind (a), the second nucleon is not involved in the interaction and hence acts as a mere spectator to the interaction and comes out of the nucleus with the momentum it had originally inside deuteron.

In the experiment described in this thesis, the de Broglie wavelength of the incident K^+ in the K^+-N centre-of-mass system is ~0.2 fermi whereas the average neutron-proton separation in the deuteron is ~3-4 fermis (fig. 8). Moreover, the characteristic period of strong interaction ($\sim 10^{-23}$ sec.) is small compared to the deuteron period ($\sim 10^{-20}$ sec.). Thus the assumptions of the Impulse approximation certainly hold for our case i.e. kaons interact with nucleons singly, rather than together.

4.3 Deuteron wavefunction and spectator momentum:

There are many wavefunctions to describe the ground state of the deuteron - among these are McGee function[20] and Hulthén-Sugawara wavefunction[21]. McGee function simulates some hard-core behaviour and also some D-state admixture but the simple S-wave Hulthén-Sugawara (will be referred in future as Hulthén) wavefunction is more commonly used. It is given by

$$\psi(r) = N \left[\frac{e^{-\alpha r} - e^{-\beta r}}{r} \right] \qquad (4\text{-}1)$$

where r is the inter-nucleon distance and N is the normalization constant which is given by

$$N = \left[\frac{\alpha\beta(\alpha + \beta)}{2\pi(\beta - \alpha)^2}\right]^{\frac{1}{2}} \tag{4-2}$$

Here α is given in terms of the nucleon mass and the deuteron binding energy, i.e. $\alpha=(mB)^{\frac{1}{2}}$ (=45.7 MeV/c). In the literature β has been quoted as $\beta=5.18\alpha$[22] and 7α[23].

The Fourier transform of the Hulthen spatial wavefunction gives the momentum distribution of the two nucleons in the deuteron:

$$\phi\ (p) = N\sqrt{\frac{2}{\pi}}\left[\frac{1}{\alpha^2 + p^2} - \frac{1}{\beta^2 + p^2}\right] \tag{4-3}$$

This gives the normalized nucleon momentum distribution

$$P(p) = 4\pi p^2 \ \left|\phi(p)\right|^2 \tag{4-4}$$

In fig. 8 we show some of the properties of the deuteron wavefunctions. The wavefunction with $\beta=7\alpha$ gives less weight to lower momentum spectators whereas more spectators get higher momentum and hence it closely compares with the McGee distribution which is theoretically more correct. So we shall use the simple Hulthen wavefunction with $\beta=7\alpha$ throughout this thesis.

4.4 <u>Spectator angular distribution and Flux factor:</u>

Since the nucleons in the deuteron have no orientation with respect to the beam, the simplified Impulse model predicts that the angular distribution of the spectator

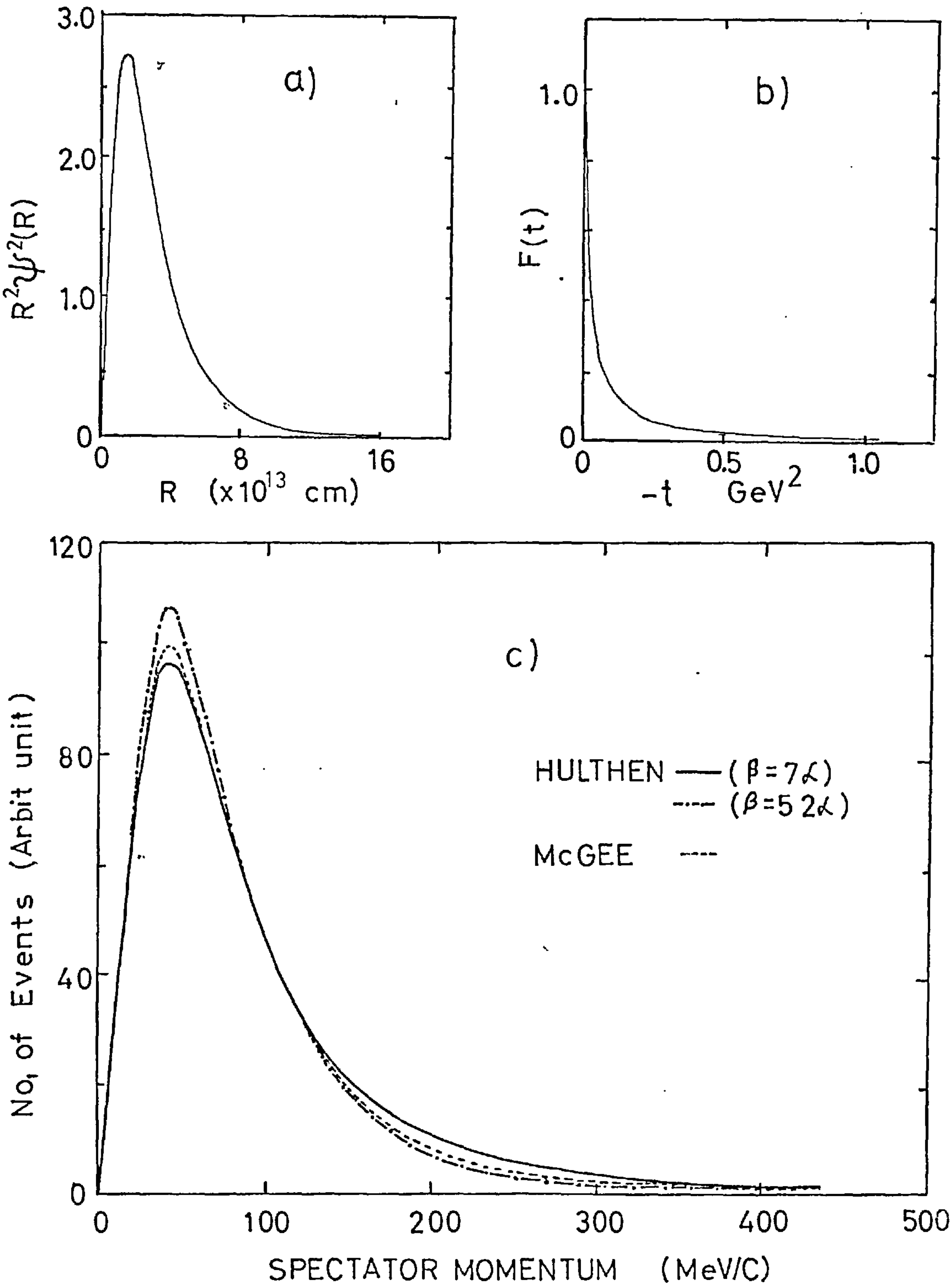
a)
b)
c)
3.0
2.0
1.0
0
8
16
$R^2\psi^2(R)$
R (x10^13 cm)
1.0
F(t)
0.5
-t GeV^2
120
80
40
0
100
200
300
400
500
No. of Events (Arbit unit)
SPECTATOR MOMENTUM (MeV/C)
HULTHEN (β=7α)
(β=5 2α)
McGEE

FIGURE 8.

around the beam is isotropic. We shall now see how two things modify this isotropy.

The number of events N_e observed in a definite final state is related to its cross section σ by

$$N_e = \sigma \rho_b \rho_t . F . VT \tag{4-5}$$

where ρ_b and ρ_t are the densities of beam and target particles in their own rest system, F is the Moller flux factor and 'VT' is the 4-dimensional observational volume. In the case where the target nucleon is moving inside the deuteron, the above formula modifies to

$$\frac{d^2N_e}{dp_s d(\cos\theta)} = \sigma' \rho_b \rho_t . F . VT \ \left|\phi(p_s, \cos\theta_s)\right|^2 \tag{4-6}$$

σ' differs from σ because of Glauber shadowing and off-mass-shell effect to be discussed later. The angular distribution thus takes the form

$$\frac{dN_e}{d(\cos\theta_s)} = \text{const.} \int F . \sigma' |\phi|^2 \ p_s^2 \ dp_s \tag{4-7}$$

Therefore, we see that that the spectator angular distribution depends explicitely on:

i) Flux factor, which is maximum when the beam and the target collide head-on and minimum when they collide while travelling in the same direction as is obvious from the expression: $F = \sqrt{(\tilde{P}_b . \tilde{P}_t)^2 - m_b{}^2 m_t^2} \ / \ m_b m_t$ ($\tilde{P}_b, \tilde{P}_t$ are the respective 4-vectors for the beam and the target of masses m_b and m_t).

and ii) variation of σ' with centre of mass energy — a rapid increase or decrease of σ with energy means more forward or backward spectators.

The effect of the flux factor is very much analogous to the familiar Doppler effect. Taking into account this effect and neglecting the variation of σ with centre of mass energy, we can write the spectator angular distribution in the form(10):

$$\frac{dN_e}{d(\cos\theta_s)} = \text{const.}\left[1 + \frac{\beta_s}{\beta_k}\cos\theta_s\right] \qquad (4\text{-}8)$$

where $\beta_s(\beta_k)$ are the spectator (beam) velocity. At 2.2 GeV/c this flux factor alone produces $\sim$10% variation in the angular distribution. The c.m. energy dependence can produce much larger variation or may cancel some anisotropy caused by the flux factor. We shall discuss this point further in a later section.

4.5 Assignment of $K^+d \rightarrow K\pi NN$ to $K^+N \rightarrow K\pi N$ channels:

The reactions of type $K^+d \rightarrow K\pi NN$ considered here are:

$$K^+d \rightarrow K^+\pi^- p\, p \qquad (4\text{-}9)$$

$$K^+d \rightarrow K^o\pi^o p\, p \qquad (4\text{-}10)$$

$$K^+d \rightarrow K^o\pi^+ p\, n \qquad (4\text{-}11)$$

The first two reactions have two protons in the final state — so the ambiguity does not arise as to which of the two nucleons in the deuteron was the target because here the incident K^+ must necessarily have interacted with the neutron. So according to the Impulse approximation these reactions can be thought of as neutron interactions:

$$K^+n \rightarrow K^+\pi^-p \qquad (4\text{-}9a)$$

$$K^+n \rightarrow K^o\pi^op \qquad (4\text{-}10a)$$

where the spectator proton momentum is less than the interacting proton. But in reaction (4-11) we have a neutron and a proton in the final state and hence this final state can result from the interactions of the incident K^+ with either of the target nucleons composing the deuteron. So acute ambiguity arises here - but, fortunately, we can separate the neutron reaction from the proton reaction on the basis of the probability distribution of the spectator momentum as given by the deuteron wavefunction. In inelastic scattering like this, the momentum difference of the two final nucleons is generally large and provides a convenient method of finding which nucleon is the target and which is the spectator. In fig. 9 we show the correlation between proton and neutron momenta for the $K^o\pi^+pn$ final state which illustrates the separation of neutron spectators from proton ones. The scatter plot for each of the incident beam momenta clearly shows the low momentum grouping of both neutron and proton whereas most of the other spaces are very much thinly populated. The identification of spectator is shown by a diagonal line and thus the events are assigned to either of the following two reactions according as:

$$K^+n \rightarrow K^o\pi^+n \quad (\text{when } p_n > p_p) \qquad (4\text{-}11a)$$

$$K^+p \rightarrow K^o\pi^+p \quad (\text{when } p_p > p_n) \qquad (4\text{-}11b)$$

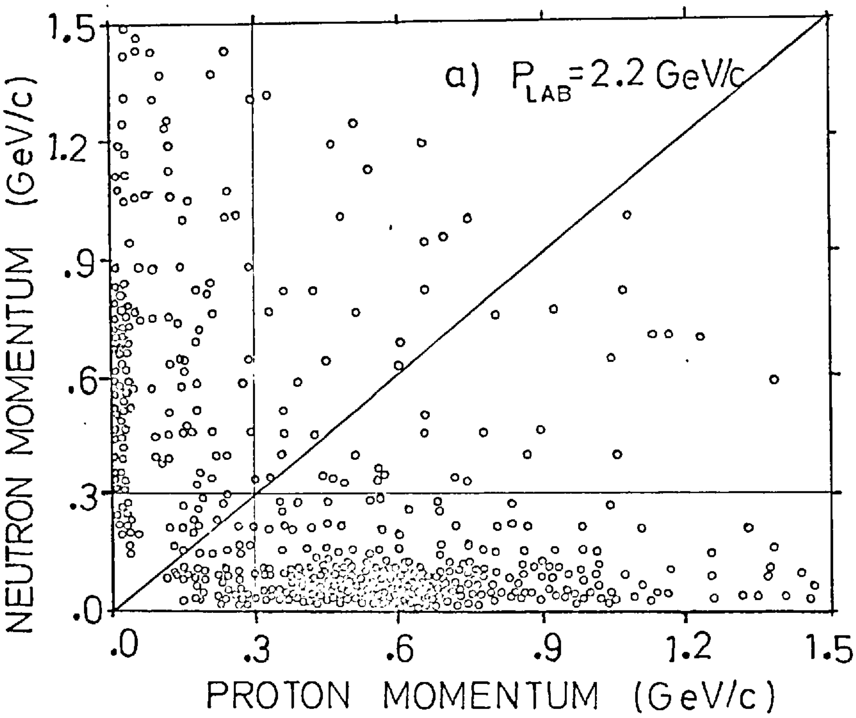
a) P_{LAB}=2.2 GeV/c
1.5
1.2
.9
.6
.3
.0
NEUTRON MOMENTUM (GeV/c)
.0
.3
.6
.9
1.2
1.5
PROTON MOMENTUM (GeV/c)

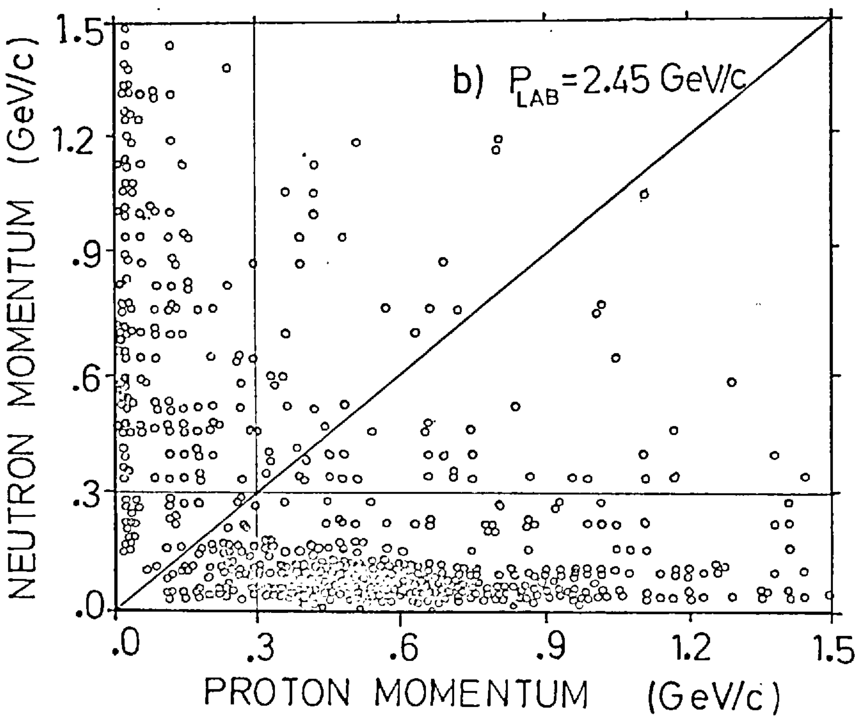
b) P_{LAB}=2.45 GeV/c
1.5
1.2
.9
.6
.3
.0
NEUTRON MOMENTUM (GeV/c)
.0
.3
.6
.9
1.2
1.5
PROTON MOMENTUM (GeV/c)

Fig. 9.

One should, however, note here that there is ambiguity between the spectator nucleon and the recoil nucleon near the diagonal line. But fortunately, there are few events near it and we estimate that $< 3\%$ spectators with momentum $\lesssim 300$ MeV/c might be defined wrongly by the above procedure.

4.6 <u>Experimental distributions of spectators</u>:

The definitions of spectators made in the previous section should now be tested by looking at the experimental momentum and angular distributions in the laboratory frame of reference and comparing these with the predictions of the Impulse model. If these are found to behave in the manner that can be expected of a spectator, then we can estimate the extent to which the conditions of the model are satisfied and hence we can put the degree of reliance on the method adopted.

Fig. 10 and 11 show the spectator momentum and angular distributions for all events of the four reactions measured in this experiment. The curves shown on momentum distributions are the predictions of the Hulthén wavefunction normalized to the number of events with spectator momentum below 300 Mev/c. We have used this upper cut on the spectator momentum because according to the model ~99% of the time the nucleons in the deuteron have a Fermi momentum less than 300 MeV/c. For reactions $K^+d \rightarrow K^+\pi^-p(p)$ and $K^+d \rightarrow K^0\pi^+p(n)$ (K^0 decay measured) the momentum distributions agree reasonably well with the predictions, although there is an excess of events

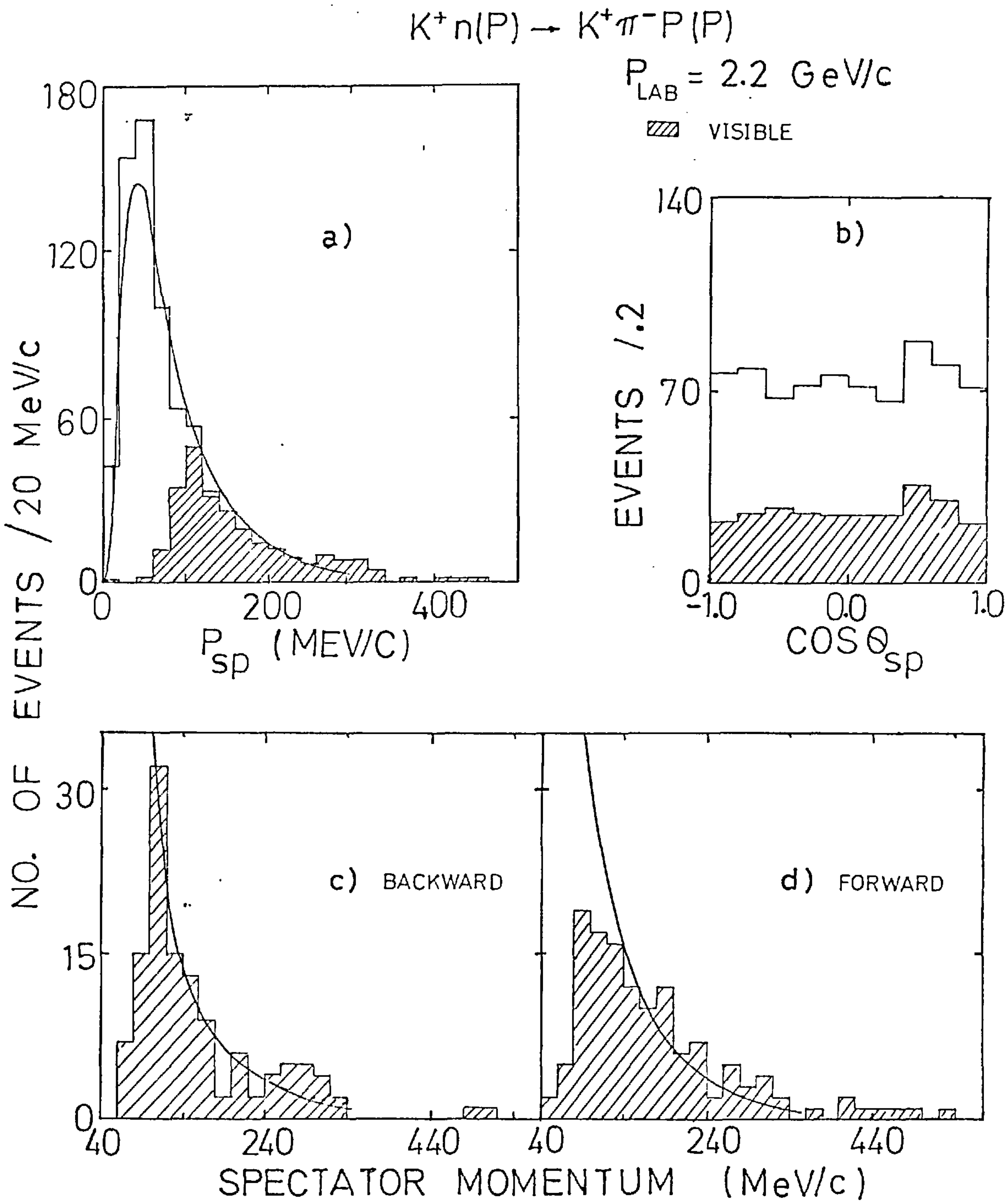
$K^+n(P) \to K^+\pi^-P(P)$
$P_{LAB} = 2.2$ GeV/c
VISIBLE
a)
b)
c) BACKWARD
d) FORWARD
NO. OF EVENTS /20 MeV/c
EVENTS /.2
P_{sp} (MEV/C)
$\cos\theta_{sp}$
SPECTATOR MOMENTUM (MeV/c)

FIGURE 10.

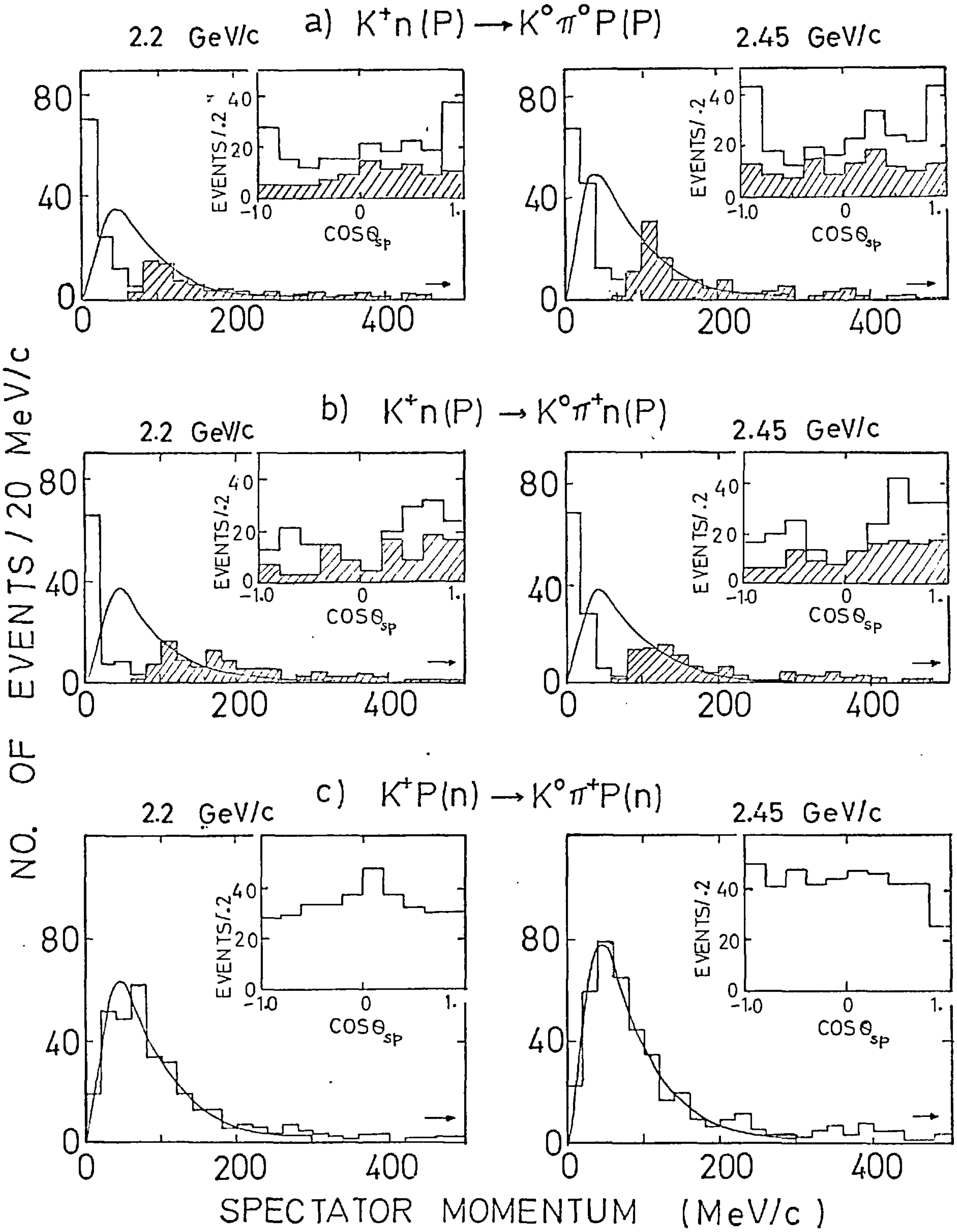

a) K+n(P) → K°π°P(P)
2.2 GeV/c
2.45 GeV/c
b) K+n(P) → K°π+n(P)
2.2 GeV/c
2.45 GeV/c
c) K+P(n) → K°π+P(n)
2.2 GeV/c
2.45 GeV/c
EVENTS/.2
COSθsp
NO. OF EVENTS / 20 MeV/c
SPECTATOR MOMENTUM (MeV/c)

FIGURE 11.

above 300 MeV/c (note, there are a very few events of the first reaction above 300 MeV/c simply because we eliminated most of these at the scanning and choicing stage by requiring that atleast one of the tracks of the event must be heavily ionizing and stopping inside the chamber with momentum less than approximately 350 MeV/c). But for the other two reactions, the data (except the visible spectator) do not agree with the prediction because of the way these kinematically under-constrained reactions, when the spectators are unseen, are handled in GRIND as mentioned earlier. The distortion of the spectator distribution toward zero momentum is due to fitting of an unseen spectator with assumed zero momentum in addition to fitting an extra neutral particle.

Now as regards angular distributions the data show the behaviour of spectators rather nicely except that the stated two reactions distributions for unseen spectators are again somewhat distorted. In all the reactions at both beam momenta we see an increase of events in the forward direction as expected because of the flux factor. But some of the anisotropy caused by the flux factor are cancelled out because of the fact that we are sitting in the energy region where the cross sections are all falling with energy.

Let us now examine the spectators from the reaction $K^+d \to K^+\pi^-p(p)$ more closely. Comparing the model separately with backward and forward seen spectators (see fig. 10c,d) we find that the model describes the backward hemisphere better than the forward one and the hemispheres are not equally populated. For forward going spectators there are more high momentum and fewer low momentum spectators relative to the prediction. We discuss below several effects which may contribute to an explanation of the behaviour of the spectators in this reaction as well as in other reactions under study.

The final state particles are almost always forward in the laboratory and for the spectator going in the forward direction, there is a few percent probability that it would scatter from one of these particles and pick up some additional momentum. This explains the reasons why the model describes the backward spectators better than the forward ones. But the excess over 300 MeV/c,as can be seen from fig. 11, can not be explained by this alone. From fig. 8a it is evident that the nucleons spend a certain amount of time very close together which means that there is a certain probability that the incident K^+ interacts with both nucleons simultaneously. This results in fast forward moving nucleons which is probably one of the major reasons for these spectators in the high momentum tail.

Finally, however, it is not well known how much of the excess large momentum spectators is due to a break-down of the Impulse approximation. In the absence of such knowledge, the model looks like a reasonable one for describing the single nucleon interaction as long as the events are restricted to those for which the model is valid i.e. spectator momentum less than 300 MeV/c. Using sample with this cut on spectator momentum the physics obtained will be the same, i.e. the physical quantities like production and decay angular distributions, effective mass spectra etc. would give us the picture of that of interaction of the incident K^+ with a single nucleon. However, as a check we have compared some detailed features like angular distributions and mass plots of the $K^o\pi^+p$ final state from K^+d interactions with those from K^+p interactions (using hydrogen bubble chamber) at close-by energies (see chapter 6) and found that the choice of spectators, we have made, is correct. This gives us confidence in the procedure we are using to extract the free nucleon reaction from K^+d data.

4.7 Some special problems in extracting K^+N physics from K^+d:

Obviously extraction of K^+N properties from K^+d data is not trivial but is beset with several problems. In what follows is a brief description of these with the means to correct for these effects.

A. Centre of mass energy smearing:

The c.m. energy shift and spread are important effects of the Fermi motion of nucleons inside the deuteron. The energy shift toward lower energy and the energy spread are given by[24]

$$\Delta E = E \frac{\langle p_s^2 \rangle}{2m^2}$$

$$\Gamma_F = 2\, P_{lab} \sqrt{\frac{\langle p_s^2 \rangle}{3m^2}}$$

where $\langle p_s^2 \rangle$ is the expectation value of the squared momentum in the deuteron state and E is the energy of the incident K^+ of momentum P_{lab} in the laboratory system of deuteron. Thus it follows that both the smearing and the energy shift are more important at high energies than at low energies and smearing will have effects on phenomena which have a strong energy dependence.

The cross section which we are measuring (chapter 5) represents an average over the distribution in c.m. energy (or alternatively, over the spectator momentum distribution). The relation between the measured cross section $\sigma\,[K^+d \to K\pi N(N_s)]$ and the real K^+N cross section is

$$\sigma\,[K^+d \to K\pi N(N_s)] = \int \sigma\,(N_s, K^+N \to K^+\pi N)\; p_s^2\, |\phi(p)|^2 dp_s - \sigma_c \quad (4\text{-}12)$$

where σ_c = Glauber shadow correction and Pauli exclusion correction to be discussed in later sections. Thus the correct procedure is to unfold $\sigma\,(N_s, K^+N \to K\pi N)$ from the above expression by an iterative procedure such as described by Lynch[25]. But, unfortunately, this procedure is not feasible in our case because the exposures in this experiment are separated by 250 MeV/c and that there are limited statistics in some channels in the present study. Therefore we take

$$\sigma\,(K^+N \to K\pi N) \cong \sigma\,[K^+d \to K\pi N(N_s)] + \sigma_c \quad (4\text{-}13)$$

which is then the cross section averaged over the Hulthén distribution for the central value of c.m. energy.

B. Glauber shadow effect:

The simple Impulse approximation picture that the total deuteron cross section should be equal to the sum of the free neutron and proton cross sections is not true in practice; because a reduction of cross section occurs which can be visualized by treating the deuteron as a rigid rotator in which, during incoherent processes, the neutron and the proton cast individual shadows. Thus for K^+-n interactions the neutron lies in the shadow cast by the proton (and vice versa) and it absorbs less effectively than when it is outside which means that the interaction probability is reduced.

In addition to the shadow effect when the amplitude is imaginary there may be non-negligible double-interaction effects such as double scattering and scattering followed by absorption. Moreover the interference effects of these amplitudes may contribute to the cross section defect. These corrections have been considered by Glauber[26] and Franco and Glauber[27]. Assuming the shadow effect to be dominant we get the simple expression for the cross section defect to the total cross section as

$$\delta\sigma = \sigma_T(K^+n)\ \sigma_T(K^+p)\ \langle r_d^{-2}\rangle/4\pi \qquad (4\text{-}14)$$

where $\langle r_d^{-2}\rangle$ is the inverse square of neutron-proton distance averaged over the deuteron ground state. This $\delta\sigma$ represents the shadowing of one nucleon by the other inside deuteron, each nucleon contributing '$\frac{1}{2}\delta\sigma$' to the total cross section defect . We do not know how this defect is distributed between the various partial cross sections. So in order to derive the true nucleon cross section from the measured value we assume that the shadow effect for every partial cross section is proportional to its share of the total cross section. Now if we want a real neutron cross section from the measured one, say for the final state f, then we have

$$\sigma_R(K^+n \to f) = \sigma_M(K^+n \to f) + \tfrac{1}{2}\,\delta\sigma' \qquad (4\text{-}15)$$

where $\frac{1}{2}\delta\sigma'$ is the Glauber shadow or screening correction to the neutron cross section due to the shadowing by proton of deuteron and $\delta\sigma = \sum_{\text{all ch.}} \delta\sigma'$. Hence we get

$$\delta\sigma' = \frac{1}{4\pi}\,\langle r_d^{-2}\rangle\,\sigma_R(K^+n \to f)\,\sigma_T(K^+p) \qquad (4\text{-}16)$$

One then finally finds the true neutron cross section (under the above mentioned assumption) using the formula:

$$\sigma_R(K^+n \to f) = \sigma_M(K^+n \to f)\,\left[1 - \frac{\langle r_d^{-2}\rangle}{8\pi}\,\sigma_T(K^+p)\right]^{-1} \qquad (4\text{-}17)$$

Taking $\langle r_d^{-2}\rangle = 0.0327$[28] this correction amounts to ~2-3% at our energies.

The validity of partial cross section determination rests on the correctness of the assumption of the distribution of $\delta\sigma'$ we made above. But even if it is not true the fractional depletion among different quasi two body states should not be greater than the total channel depletion and since this depletion is less than the statistical uncertainties involved, the Glauber correction will have almost no effect on resonance cross section determination.

We also estimate the overall effect of having a deuteron target by comparing the cross sections $\sigma(K^+p \to K^0\pi^+p)$

and $\sigma'[K^+p(n)\rightarrow K^o\pi^+p(n)]$ measured in hydrogen and the present experiment respectively. Although there are on the average ~10-15% events with a spectator faster than 300 MeV/c, the observed ratios, R_c $(=\sigma/\sigma')$, using ref.29 for K^+p cross sections, are 1.03 and 1.05 at 2.2 and 2.45 GeV/c respectively. These 3 and 5% corrections on the basis of the normalization of the cross sections with those of hydrogen experiments are not as large as we expected. The major factors which should affect R_c are systematic differences between the cross sections of this experiment and those of hydrogen experiments, spread of the c.m. energy in a K^+d interaction. Since the cross sections obtained by using the crude method of scaling the deuterium cross sections by R_c (as was done in refs. 10, 11) and those obtained by formal deuteron correction do not differ significantly (atleast in the present calculations with our rather limited statistics) and that there is uncertainty in all these calculations, we will only quote results using the formal deuteron correction.

C. Pauli exclusion effect:

For the exact shape of differential cross sections and correct total cross sections of channels with two protons in the final state, one must also consider the effect of Fermi statistics which excludes certain angular momentum states between these two identical outgoing fermions. Let us consider the reactions $K^+d \rightarrow K^opp$, $K^+d \rightarrow K^+\pi^-pp$ and $K^+d \rightarrow K^o\pi^opp$ at very low four-momentum transfer square ($t\cong 0$). In each of these reactions the neutron in the deuteron has necessarily been transformed into a proton and the two protons are very close together in S-wave spin 1 configurations (neglecting ~4% D-wave). Thus the isospin of one of the nucleons flips and hence the spin of the nucleon must also flip in order that the reaction takes place without violating the symmetry requirements of spatial wavefunction of the two-nucleon system. Hence we see that there is a restriction on the non-spin-flip amplitude required by the Pauli exclusion principle for two very low momentum protons.

The expression for measured differential cross section of the final state with two protons in terms of the true neutron cross section is[30]:

$$\left(\frac{d\sigma_d}{dt}\right)_m = \left[1-F(q)\right]\left(\frac{d\sigma_n}{dt}\right)_{nf} + \left[1-\frac{F(q)}{3}\right]\left(\frac{d\sigma_n}{dt}\right)_{sf} \qquad (4\text{-}18)$$

where $q=\sqrt{-t}$ is the 3-momentum transfer in the collision. The deuteron form factor $F(t)$ with Hulthén wavefunction is shown in fig. 8b as a function of $-t$. At $-t \cong 0$, $F(t) \simeq 1$ and as $-t$ increases, $F(t)$ approaches zero but remains significant upto $-t \simeq .1$ GeV^2 and thus it follows that the exclusion effects should be noticeable in $0 \lesssim -t \lesssim .1$ GeV^2. But to make the correction one must know the relative amounts of the spin-flip and non-flip amplitudes. The correction in the differential cross section has been made using a tabulation[31] which involves a calculation of the spin-flip and spin-non-flip contributions to the amplitudes based on π exchange model. This correction amounts to $\approx 3\%$ to the total channel cross sections.

CHAPTER 5

CROSS SECTION MEASUREMENTS

5.1 Checks, biases and corrections:

In the following paragraphs checks for possible contamination in the beam, biases due to scanning, measuring and fitting and corrections due to finite size of the chamber will be studied and discussed in brief.

A. Beam characteristics and contamination:

The measured spread in momentum of a perfectly mono-energetic beam is determined by the finite momentum resolution of measurements. The larger width of the experimental distribution is caused by finite spread of the incident beam momenta, energy loss for different path length in the chamber and effects caused by small angle scattering at various points in the beam transport system. The mean beam parameters at the entrance window are:

$P = 2.18 \pm .03$ Gev/c ; $\lambda = -.005 \pm .004$ rad. ; $\phi = 3.123 \pm .005$ rad.

$P = 2.43 \pm .03$ GeV/c ; $\lambda = -.005 \pm .004$ rad. ; $\phi = 3.175 \pm .005$ rad.

Sometimes apparently onbeams are found to have wildly different beam parameters from the mean. These are either due to scattering in the beam window or small angle scattering of the beam in the bubble chamber before interactions. A correlation of dip angle λ and Z-coordinate of the interaction vertex of the beam exists for such beams. The spatial position of the beam in the chamber is well known. So in order that such beam and other non-beam events do not affect physics, we have applied fiducial criteria for the acceptance of a beam (see later).

From kaon separation curve taken during beam tuning we expect about 5-10% pion flux in the beam. Events with V^o's are hardly contaminated by pion events. But for 3- and 4-prong events without V^o's, the $K^+ - \pi^+$ ambiguity in many cases could not be resolved by fitting and ionization because the tracks are relativistic and hence pion contamination seems to present some difficulties. In order to estimate pion contamination, the latter category of events have been fitted to both incident kaon and pion beams. From χ^2 probability, MM^2 and from a host of other physical distributions (see also section 5.2), it has been found that almost all of the ambiguous events (between 4C K^+d and 4C π^+d hyp.) are produced by kaons. From the unique pion fits the contamination of pion events is estimated as $\lesssim 3\%$ in $K^+d \to K^+\pi^-pp$ at 2.18 GeV/c.

B. <u>Fiducial volume and K^o_S correction</u>:

<u>Fiducial Volume</u>: Events are difficult to measure well near the edge of the chamber. So a fiducial volume was chosen in the central region of the chamber so that all parts of the volume could be seen clearly by all three camera views. The events that have the interaction and K^o decay vertices within these volumes are said to satisfy INVOL and INLITE respectively. The coordinates of the boundaries of INVOL and INLITE are given in table II.

Table II INVOL and INLITE volumes.

P_{lab}	INVOL (cms)			INLITE (cms)		
GeV/c	X	Y	Z	X	Y	Z
2.2	-48,38;	-11,10 ;	-25.5,-19.5	-45,52;	-18,16;	-46,0
2.45	-43,36;	-7,12.5;	-25.5,-19.5	-45,52;	-18,16;	-46,0

K_s^o correction: We now consider the K_s^o decay correction. We note that K_s^o's produced in strong interaction have mean decay length of a few cms - so most of them would be detected inside the INLITE volume. But losses occur due to: i) escape loss, where K_s^o decays far from the primary vertex outside the bubble chamber, and ii) short-length scanning loss, where it decays so close to the production vertex that it is confused with the primary vertex and is thus lost.

These two losses were dealt with by using a cut-off and by weighting the remaining events by a weight 'W' as determined below:

Let l denote the mean decay length of K_s^o particle. The probability that it does not decay before reaching the minimum observable projected length, l_m is

$$P_1 = e^{-l_m/l\cos\lambda}$$

where λ is the dip angle of the K_s^o. Now the probability of decay during next $(l_p - l_m/\cos\lambda)$ cms is

$$P_2 = \left[1 - e^{-(l_p - l_m/\cos\lambda)/l}\right]$$

where l_p is the potential length i.e. the maximum possible length from the production vertex, along the line of flight of the K_s^o, to the INLITE volume. Thus the probability that a K_s^o does not decay in the first $(l_m/\cos\lambda)$ cm but does so in the next $(l_p-l_m/\cos\lambda)$ cms is

$$P = e^{-l_m/l\cos\lambda}\left[1 - e^{-(l_p-l_m/\cos\lambda)/l}\right] \qquad (5\text{-}1)$$

The reciprocal of this factor was used as a weighting factor to compensate for those K_s^o's which decayed outside the prescribed length interval. The weight assigned to each event is:

$$W = \left[e^{l_m/l\cos\lambda} - e^{-l_p/l}\right]^{-1} \qquad (5\text{-}2)$$

All analysis were carried out on the weighted events.

To determine the short-length cut-off l_m, we assumed a series of values for l_m, and plotted the total weighted number of events at each momentum as a function of l_m. We chose that value of l_m at which the total weighted number stopped increasing and remained approximately constant with increasing value of l_m. We found $l_m \cong 0.4$ cm for both 2.2 and 2.45 GeV/c.

The corrections for $K_s^o \to \pi^o\pi^o$ and $K_L^o \to 3\pi$ decay modes will be considered in section 5.3.

C. Biases in scanning, measuring and fitting:

There is a certain class of events with particular spatial configurations which are harder to see and to measure than others. The biases which might be present due to these are minimized by using the fiducial volume cut as described in the previous section. As noted earlier all our film is double-scanned and the overall scanning efficiency varies between 98-99% for all topologies at both momenta. The plots of K^o disintegration angle for K^o events (not shown) do not show any significant sign of bias in the data.

As mentioned earlier GRIND uses the track variables ρ (=1/p), λ and ϕ (reconstructed by MDT) as the starting point in carrying out the minimization of χ^2 function. So by studying the amount by which these variables are moved from their measured values, a check for biases or errors in the measuring and fitting procedure can be made. The pull for any variable 'X' is defined to be

$$(\mathrm{Pull})_X = \frac{X_m - X_f}{\delta(X_m - X_f)}$$

where X_m and X_f are the measured and fitted values of the variable respectively. If X_m has a Gaussian distribution, then the resulting pull is normally distributed with mean zero and standard deviation one, provided there are no uncorrected systematic biases and that the measured errors are correctly estimated[32] (the latter point is checked from probability distribution). The pull distributions for the three variables ρ, λ, ϕ of all tracks are Gaussian like — for beam tracks at 2.2 Gev/c, the mean values for these are 0.05, -.01, -.04 with standard deviations of 1.07, 1.11 and 1.08 respectively. From these and similar observed values at 2.45 Gev/c, we can say that the biases are negligible and the smaller shifts reflect the degree of accuracy to which optical constants used in reconstructing the tracks in space are known.

5.2 Final state separation:

Most of our well measured events are found to be assigned to a single hypothesis. But a small fraction of well measured events and some of the badly measured events remained kinematically ambiguous even after a further check on a scan table. For accurate cross section calculation, one should separate these ambiguous events into a given final state and estimate the amount of contamination introduced in the final state by unresolved ambiguous as well as multi-neutral events. In the following paragraphs we shall deal with these in brief.

A. Final state $K^+\pi^-pp$:

Because of the smaller amount of phase space available it is difficult for final state like $K^+\pi^-\pi^0pp$ (or multi-neutral events) to fake 4C $K^+\pi^-pp$ fits and hence the final state is believed to be negligibly contaminated. The only ambiguity comes from $\pi^+d\rightarrow\pi^+\pi^-pp$ (and negligibly few $K^+\pi^+\pi^-d$ i.e. 0.5%) as $K^+-\pi^+$ ambiguity can not be resolved because the track in question is relativistic. For these ambiguous events, we compare in fig. 12a,b the $K^+\pi^-$ effective mass distribution assuming reaction $K^+d\rightarrow K^+\pi^-pp$ with $\pi^+\pi^-$ distribution for the same tracks assuming $\pi^+d\rightarrow\pi^+\pi^-pp$. In fig. 12a, we see a strong $K^{*o}(892)$ of width ~60 MeV — this striking resonance structure is the same as seen in the unambiguous events. But the $(\pi^+\pi^-)$ effective mass distribution (fig.12b) shows an enhancement at ~710 MeV and of width ~120 MeV which is clearly incompatible with the ρ^o mass of 765 MeV. So from these studies of ambiguous K^+d and the unambiguous π^+d events, other experimental features of the data and expected yields for both reactions, we find that almost all of these ambiguous events are really K^+d events and estimate that the remaining pion contamination in this final state at 2.2 GeV/c is less than 3%.

The quality of the data can also be inferred from the plot of missing mass square (MM^2) to $K^+\pi^-pp$ (fig. 12c). The very sharp peak near zero is a consequence of the highly constrained class of events and the distribution clearly shows that there is almost no contamination of the sample by events with an additional π^o.

B. <u>One-, two-prong K^o events:</u>

The one- and two-prong events with a seen K^o can be any of the following reactions:

$$K^+n(p) \rightarrow K^o\pi^o p(p) \qquad \text{(B-1)}$$

$$K^+n(p) \rightarrow K^o\pi^+ n(p) \qquad \text{(B-2)}$$

$$K^+p(n) \rightarrow K^o\pi^+ p(n) \qquad \text{(B-3)}$$

$$K^+d \rightarrow K^o\pi^+ d(+\pi^o) \qquad \text{(B-4)}$$

and missing mass events where more than one π^o are produced. The above reactions are almost free from pion contamination.

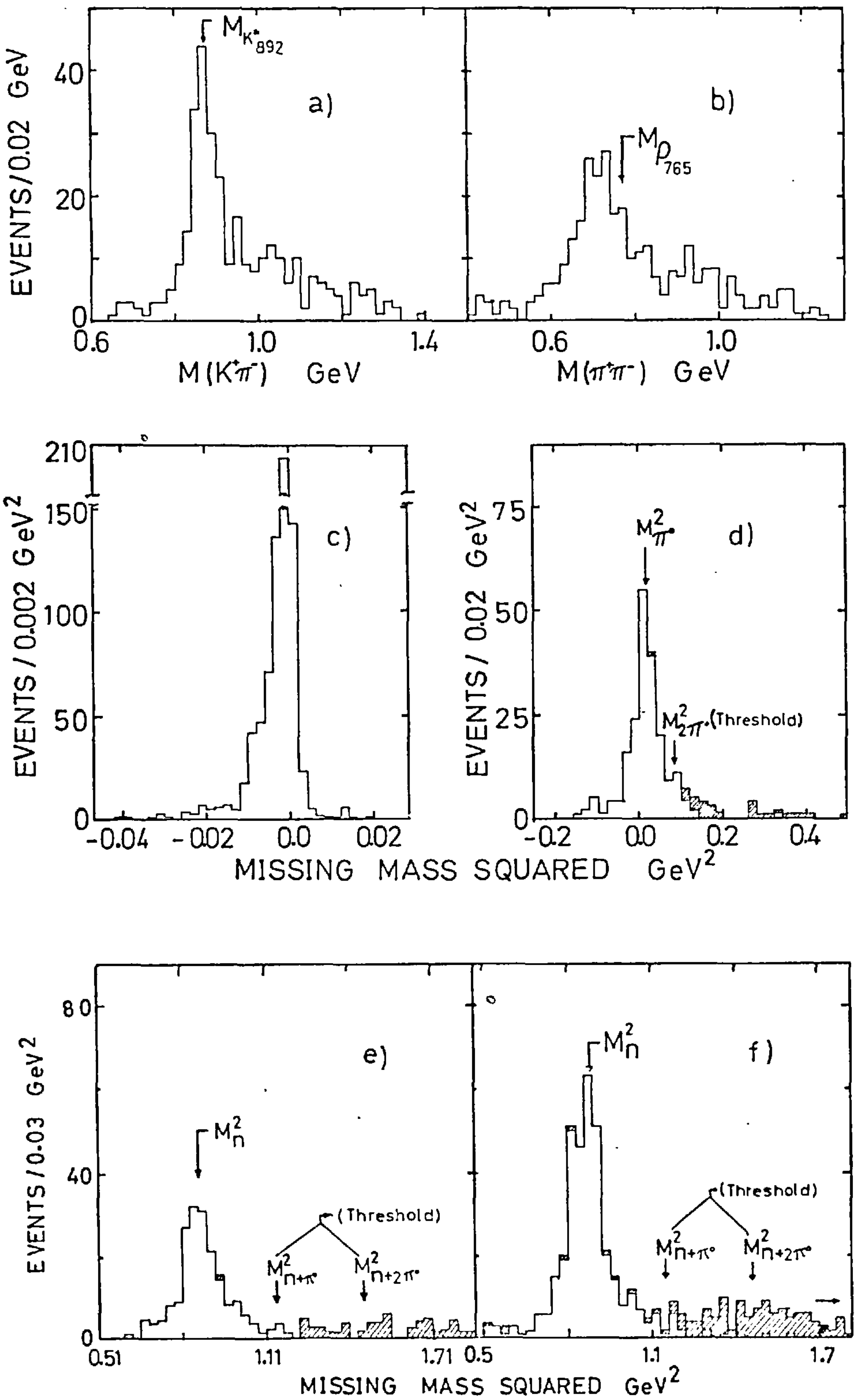

$M_{K^*_{892}}$
a)
b)
$M_{\rho_{765}}$
EVENTS/0.02 GeV
40
20
0
0.6
1.0
1.4
$M(K^+\pi^-)$ GeV
$M(\pi^+\pi^-)$ GeV
210
150
100
50
c)
d)
$M^2_{\pi^0}$
$M^2_{2\pi^0}$ (Threshold)
EVENTS / 0.002 GeV^2
EVENTS / 0.02 GeV^2
75
25
-0.04
-0.02
0.0
0.02
-0.2
0.2
0.4
MISSING MASS SQUARED GeV^2
e)
f)
M^2_n
(Threshold)
$M^2_{n+\pi^0}$
$M^2_{n+2\pi^0}$
EVENTS / 0.03 GeV^2
80
0.51
1.11
1.71
0.5
1.1
1.7

FIGURE 12

Some of the pion produced V^o reactions are $\pi^+p \rightarrow K^+\Lambda^o\pi^+$, $\pi^+n \rightarrow K^+\Lambda^o\pi^o$ etc. The Λ^o's so produced are readily distinguished from K^o's because a pion and a proton from a V^o decay could be identified easily. Moreover, as mentioned earlier, the pion flux in the beam is believed to be less than ~10% and the cross sections for these associated production reactions are small at our energy. So the pion contamination does not present any problem and hence events with a seen K^o in the final state can be said to be free from non-kaon events. Similarly because of energy consideration, presence of final states like $K^+p \rightarrow K^+K^+\Lambda^o$, $K^+p \rightarrow K^+K^+\Lambda^o\pi^o$ etc. can be overlooked.

Now we want to separate $K^+d \rightarrow K^o\pi^+pn$ from coherent $K^+d \rightarrow K^o\pi^+d(+\pi^o)$ events. A total of 32 events at 2.2 GeV/c (50 events at 2.45 GeV/c) made both $K^+d \rightarrow K^o\pi^+pn$ and coherent deuteron fits. Of these 5 events at 2.2 GeV/c and 10 events at 2.45 GeV/c satisfied usual deuteron testing criteria that in the $K^o\pi^+pn$ fit, the effective mass of the two nucleons was small, $M_{pn} < 1.885$ GeV and the fitted laboratory angle, θ_{pn} between the two nucleons was nearly zero ($\cos\theta_{pn} > 0.8$) .

The above separation leaves a small fraction of the $K^+d \rightarrow K^o\pi^+pn$ final state which is ambiguous with other final states including the multineutral events. With spectator cut at 300 MeV/c the ambiguity here moves down to ~3% at both momenta. As for the $K^+d \rightarrow K^o\pi^opp$ final state with the same cut on the momentum of the spectator the ambiguity contaminations are 2.5% and 3% at 2.2 and 2.45 GeV/c respectively.

Now to estimate the extent of contamination of the 1C events under study from the unfitted multineutral (NOFIT) events, we show in fig. 12 (d-f) the missing mass squared (MM^2) distributions for the different reactions at 2.2 GeV/c (the 2.45 distributions not shown). The shaded events correspond to NOFIT events. The MM^2 to the reactions $K^+n(p) \rightarrow K^o\pi^o p(p)$, $K^+n(p) \rightarrow K^o\pi^+ n(p)$ and $K^+p(n) \rightarrow K^o\pi^+ p(n)$ should peak at $M^2_{\pi^o}$, M^2_n, M^2_n respectively, whereas for the NOFIT events, the corresponding quantities should lie above the kinematic threshold of 0.073, 1.15 and 1.15 GeV^2 respectively. It is seen from the plots that the distributions peak at the right value of the mass squared of the respective neutral particles — but there is a slight right hand tail of each of these distributions. From the shape of these distributions one can see that there is negligible contamination of the different 1C reactions from the multineutral events (also true at 2.45 GeV/c).

5.3 Total channel cross sections:

The cross section for a particular stable final state is related to the mean free path, λ by

$$\sigma = \frac{1}{n\,\lambda}$$

where n is the number of nuclei per cm^3 which is related to the density of deuterium, ρ_d by $n = N_o\,\rho_d/A$. Here N_o and 'A' are the Avogadro's number ($=6.02\times10^{23}$ mol^{-1}) and gram per mol. of the target (=2.01 gm/mol) respectively.

If there are N_i interactions in total K^+_{inc} path length of L cms, then $\lambda = L/N_i$. Thus for cross section calculation, we ought to know the only unknown quantity L. Since we do not know the exact amount of π^+ and μ^+ contamination in the beam, the observed number of tau decays, N_τ in the same volume has been used to determine L from

$$L = \frac{P_{K^+}\ c\ \tau_{K^+}}{B\ m_{K^+}} .\ N_\tau$$

where m_{K^+} = mass of the incident particle of momentum, P_{K^+},

τ_{K^+} = K^+ life time ($c\tau_{K^+} = 370.8$),

$B = (K^+ \rightarrow \pi^+\pi^+\pi^-)/(K^+ \rightarrow \text{all}) = 0.0558 \pm .0003$.

Using the numerical values we finally get σ in terms of N_i, N_τ and P_{K^+} as

$$\sigma_i\ (\text{mb}) = \frac{N_i}{N_\tau} . \frac{1.837}{\langle P_{K^+}(\text{GeV/c})\rangle} \qquad (5\text{-}3)$$

where the density of deuterium ρ_d has been taken as 0.135 gm/cm^3. The numbers N_i and N_τ have been corrected for the scanning and the measuring efficiencies. For final states with a K^0, a weight 'WT' was assigned to each event to allow for the probability that the K^0 does decay visibly. The factor WT = 1/(0.342 P), where P is the probability for the K^0 to decay visibly (via two-body) inside the bubble chamber and the factor 0.342 is the branching ratio for decay of the K^0 into two charged particle (i.e. $[K^0_s \rightarrow \pi^+\pi^-] / [K^0 \rightarrow \text{all}]$).

The results of the calculation are given in table III. The errors quoted are the statistical uncertainty contributed by the number of interactions and the number of taus in the sample.

Table III. Total channel cross sections.

Reactions	CROSS SECTION (mb)	
	P=2.2 GeV/c	P=2.45 GeV/c
$K^+n \rightarrow K^+ \pi^- p$	3.00 ± 0.20	--
$K^+n \rightarrow K^0 \pi^0 p$	2.10 ± 0.20	1.72 ± 0.15
$K^+n \rightarrow K^0 \pi^+ n$	1.80 ± 0.20	1.30 ± 0.12
$K^+p \rightarrow K^0 \pi^+ p$	3.50 ± 0.30	2.65 ± 0.21

T=0 total $K\pi N$ cross section:

The measured partial cross sections of K^+n and K^+p allow us to deduce the total single pion production cross section for the pure T=0 isospin state. Using the method of Shmushkevich[33] one can very easily get the following expression for the total cross section in terms of the individual channel cross section:

$$\sigma_0(K^+N-K\pi N) = 3\left[\sigma(K^+n\rightarrow K^+\pi^-p)+\sigma(K^+n\rightarrow K^0\pi^+n)-\tfrac{1}{2}\sigma(K^+p\rightarrow K^0\pi^+p)\right] \quad (5\text{-}4)$$

Using this relation and the measured cross sections of table III, we calculate σ_0 to be 9.15 ± 0.95 mb at 2.2 GeV/c.

CHAPTER 6

RESONANCE PRODUCTION

6.1 General features of the Dalitz plots:

The single pion production reactions studied in this thesis are:

$$K^+n \rightarrow K^+\pi^-p \quad \text{(only at 2.2 GeV/c)} \qquad (6\text{-}1)$$

$$\left.\begin{array}{l} K^+n \rightarrow K^0\pi^0p \\ K^+n \rightarrow K^0\pi^+n \\ K^+p \rightarrow K^0\pi^+p \end{array}\right\}\text{(at 2.2,2.45 GeV/c)} \qquad \begin{array}{r}(6\text{-}2)\\(6\text{-}3)\\(6\text{-}4)\end{array}$$

produced by 2.2 and 2.45 GeV/c K^+d interactions only. Unlike a two-particle final state the information contained in a three-particle final state is difficult to present and to interpret. In this case the Dalitz plot gives indication of interaction between any two of the three particles. Fig. 13 shows the Dalitz plots for these reactions from which the following features of the data may be observed:

i) All of the final states are dominated by quasi-two-body intermediate states.

ii) In K^+n channels there are copious production of $K^{*+}(892)$, $K^{*0}(892)$ - but the $\Delta(1230)$ production is very small as is expected from isospin invariance. In $K^+n \rightarrow K^0\pi^+n$, there is some indication of $N^{*+}(1688)$.

iii) There is strong $K^{*+}(892)$ and $\Delta^{++}(1230)$ production in K^+p channel.

iv) There is no evidence for $K^*(1420)$ production because of the availabity of phase space.

v) Evidence for a Z^* decaying into KN is absent.

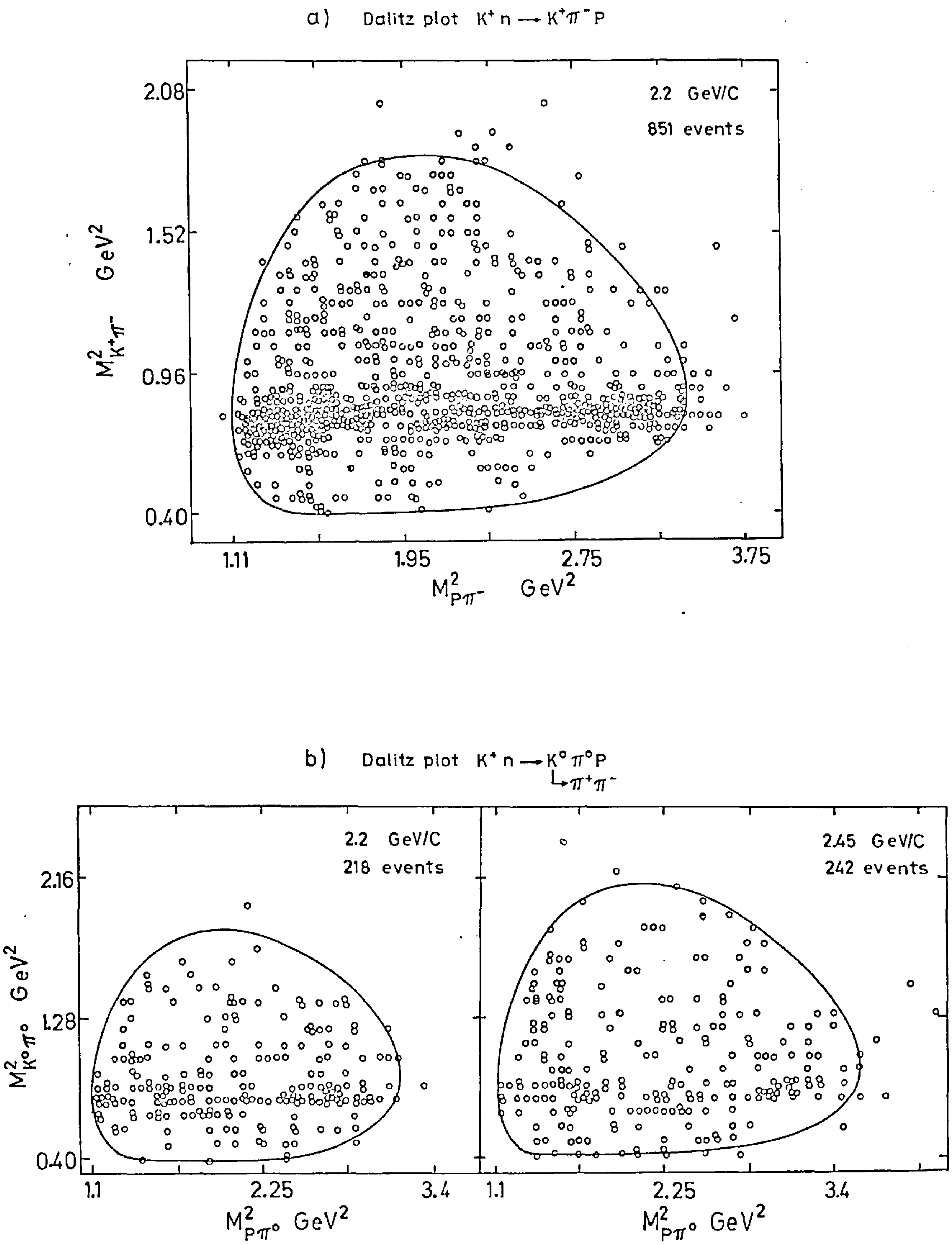
a) Dalitz plot $K^+ n \to K^+ \pi^- P$
2.2 GeV/C
851 events
2.08
1.52
0.96
0.40
$M^2_{K^+\pi^-}$ GeV^2
1.11
1.95
2.75
3.75
$M^2_{P\pi^-}$ GeV^2
b) Dalitz plot $K^+ n \to K^0 \pi^0 P$, $K^0 \to \pi^+\pi^-$
2.2 GeV/C
218 events
2.45 GeV/C
242 events
2.16
1.28
0.40
$M^2_{K^0\pi^0}$ GeV^2
1.1
2.25
3.4
$M^2_{P\pi^0}$ GeV^2
1.1
2.25
3.4
$M^2_{P\pi^0}$ GeV^2

FIGURE 13

c) Dalitz plot $K^+n \longrightarrow K^0\pi^+n$, $\hookrightarrow \pi^+\pi^-$

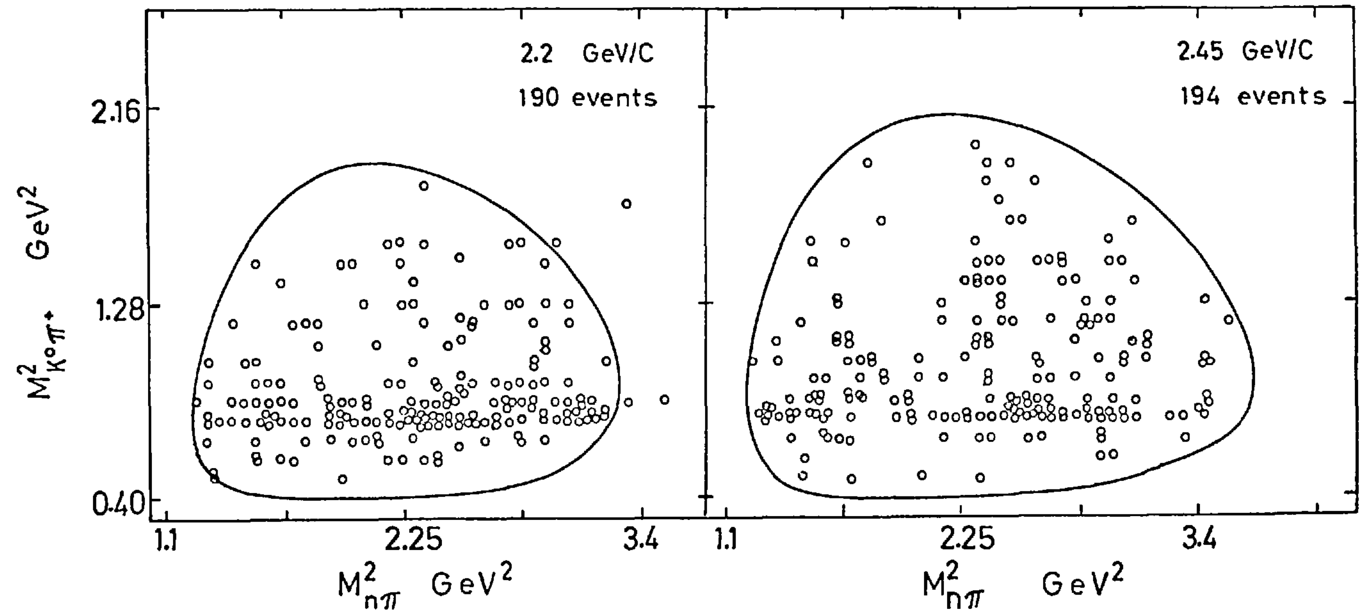

d) Dalitz plot $K^+P(n) \longrightarrow K^0\pi^+P(n)$, $\hookrightarrow \pi^+\pi^-$

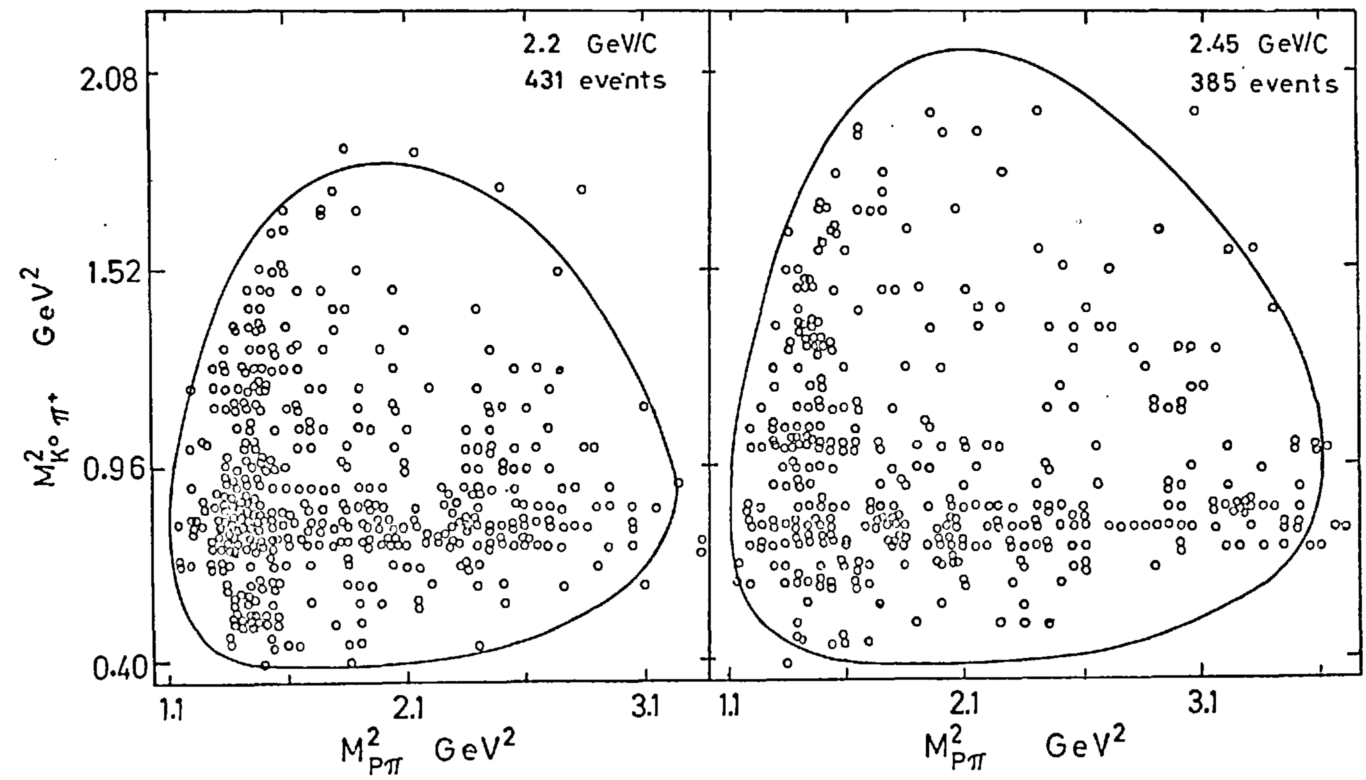

FIGURE 13

6.2 Fitting of the Dalitz plots:

To know the cross section for the various resonant processes involved, it is necessary to estimate the fraction of events in a given final state which belong to the resonance. For this purpose we represent the event population of the Dalitz plots by a function which is the incoherent sum of the processes involved plus the phase space. For each event the function has the form:

$$L = \frac{1 - \sum_i \alpha_i}{A} + \sum_i \alpha_i \frac{(BW)_i \ (PH)_i}{N} \qquad (6\text{-}5)$$

The first term is the genuine 3-body phase space (i.e. final state with no intermediate resonance state), where α_i is the fraction of events in which the ith resonance is produced and A is the area of the Dalitz plot. The second term gives the sum of the intensities of the resonances considered. BW is the Breit-Wigner factor given by[34]

$$BW = \pi^{-1} \frac{M_o \ \Gamma(M)}{(M^2-M_o^2)^2 + M_o^2 \Gamma^2} \qquad (6\text{-}6)$$

The phase space factor, $PH = M/q$, where q is the 3-momentum of the decay particle in the rest system of mass M; M_o being the mass of the resonance.

The energy variation of Γ for two-body decay is of the form

$$\Gamma = \Gamma_o \ (q/q_o)^{2l+1} \ \frac{\rho_M}{\rho_{M_o}} \qquad (6\text{-}7)$$

where l is the relative orbital angular momentum of the decay particles and $\Gamma = \Gamma_o$, $q = q_o$ for $M = M_o$. ρ_M is a slowly varying factor. For $J^P=1^-$ $K^*\to K\pi$ proceeding via pseudoscalar exchange

$$\Gamma = \Gamma_o (q/q_o)^3 \frac{M}{M_o} \qquad (6\text{-}7a)$$

For 1^- $K^*\to K\pi$ proceeding via vector exchange the right hand side of (6-7a) is further multiplied by p_p^2, the square of the recoil nucleon momentum in the overall c.m. system. For P-wave $\Delta\to N\pi$ we have

$$\Gamma = \Gamma_o(q/q_o)^3 \frac{(M+m_p)^2-m_\pi^2}{(M_o+m_p)^2-m_\pi^2} \frac{M_o}{M} p_K^2 \qquad (6\text{-}7b)$$

And for F-wave $N^*(1688)$ we used the fixed value of Γ. p_K is the recoil kaon momentum in the overall c.m. system. In the two expressions above, the variables have their usual significance appropriate for K^* and Δ. For vector exchange there is the need for an appropriate overall factor of $p^{3(5)}$ instead of the usual phase space factor p obtained when one integrates (BW.PH) over a strip of Dalitz plot - so the presence of p^2 term in the expressions (6-7a) and (6-7b).

We have neglected the interference term in the expression (6-5) but for the $K^+p \to K^o\pi^+p$ final state there may be non-negligible interference between K^{*+} and Δ^{++}. Again a resonance which does not decay isotropically in its rest system will introduce structure in the Dalitz plot which is not taken into account in the Breit-Wigner function. To be exact, one must multiply (BW) by the appropriate angular distribution $W(\cos\theta_d)$ (θ_d= angle between the direction of the decay particle in the resonance rest system and the line of flight of the resonance in the overall c.m. system). If one takes all these into account, then it would necessitate the inclusion of more adjustable parameters in the fit which considering the statistics of the present data do not provide a meaningful simultaneous determination of all the required parameters. As is seen from the Dalitz plots there seems to be negligible interference in the $K^{*+}-\Delta^{++}$ overlap region. Therefore we neglect these considerations from the fitting.

From the probability density function (6-5) we now construct the likelihood function for n events and i resonances as

$$L(\alpha_i, \Gamma_i, M_i) = \prod_{K=1}^{n} W_K \, L_K \qquad (6\text{-}8)$$

where W_K is the weight associated with each event.

The area $A = \iint dM_{12}^2 dM_{23}^2$ of the Dalitz plot is calculated using Simpson's rule and the normalization factor is given by

$$N = \iint BW(M_{12}).PH.\ dM_{12}^2 dM_{23}^2 \qquad (6\text{-}9)$$

To ensure correct allowance for the spread in the c.m. energy in K^+d interactions one should calculate the integral for each event individually which means several thousand calculations of (BW.PH) for each resonance and for each event. Thus in order to save computing time as well as allowing for proper c.m. energy variation, the whole c.m. energy range was divided into several intervals and the normalization was performed using these different energies weighted according to the number of events near each chosen energy.

For convenience the negative of the logarithm of the likelihood function (6-8) was minimized in the space of the varied parameters with the aid of the CERN program MINUITS[35]. For resonances weakly produced, the mass and the width have been kept fixed during the fitting. The widths of K^*'s in reactions (6-2), (6-3) and (6-4) were varied at first in the fitting -- although the fit gave reasonable widths, the errors on the widths were rather large particularly in reactions (6-2) and (6-3). So fits were also per~~for~~formed fixing the widths of the resonances and it was found that the fractions of resonances remain same within errors. The results obtained using only those events having spectator momentum $\lesssim 300$ MeV/c are given in table IV. It should be pointed out here that the numbers of events used in the fitting at 2.2 GeV/c are higher than the numbers used in the cross section calculations and other physics studies. These extra events came from the volume of the bubble chamber where taus needed for normalization of cross sections were not processed at the time of writing the thesis. We also tried the fitting without these events and found that the parameters do not change appreciably.

When a minimum is found the second derivative matrix is calculated and the error matrix is obtained by inverting it. The errors quoted in the table are defined for a function change of 0.5 i.e. δ log L = 0.5. In order to see how well

Table IV.. Results of Dalitz plot fits. F ≡ fixed.

P_{lab} (GeV/c)	Reaction	Fraction (%)	Mass (MeV)	Width (MeV)
2.2	$K^+n \rightarrow K^{*0}(K^+\pi^-)p$	55.9 ± 3.5	901.4 ± 2.3	63.0 ± 7.3
	$\rightarrow \Delta^0(p\pi^-)K^+$	9.8 ± 2.0	1224.0 ± 9.2	100 (F)
	$K^+n \rightarrow K^{*0}(K^0\pi^0)p$	42.3 ± 5.5	906.6 ± 4.7	55 (F)
	$\rightarrow \Delta^+(p\pi^0)K^0$	5.0 ± 3.6	1220.0 (F)	100 (F)
	$K^+n \rightarrow K^{*+}(K^0\pi^+)n$	53.9 ± 5.5	905.9 ± 4.4	55 (F)
	$\rightarrow \Delta^+(n\pi^+)K^0$	2.6 ± 3.1	1220.0 (F)	100 (F)
	$\rightarrow N^{*+}(n\pi^+)K^0$	9.8 ± 3.9	1688.0 (F)	100 (F)
	$K^+p \rightarrow K^{*+}(K^0\pi^+)p$	42.0 ± 3.8	898.5 ± 4.0	55 (F)
	$\rightarrow \Delta^{++}(p\pi^+)K^0$	40.0 ± 3.7	1224.4 ± 1.1	100 (F)
2.45	$K^+n \rightarrow K^{*0}(K^0\pi^0)p$	29.5 ± 4.8	907.8 ± 3.7	55 (F)
	$\rightarrow \Delta^+(p\pi^0)K^0$	11.5 ± 3.9	1220.0 (F)	100 (F)
	$K^+n \rightarrow K^{*+}(K^0\pi^+)n$	43.5 ± 5.9	899.1 ± 5.4	55 (F)
	$\rightarrow \Delta^+(n\pi^+)K^0$	4.7 ± 3.6	1220.0 (F)	100 (F)
	$\rightarrow N^{*+}(n\pi^+)K^0$	9.6 ± 4.4	1688.0 (F)	100 (F)
	$K^+p \rightarrow K^{*+}(K^0\pi^+)p$	42.0 ± 3.7	898.5 ± 3.8	55 (F)
	$\rightarrow \Delta^{++}(p\pi^+)K^0$	33.8 ± 3.6	1220.0 ± 5.3	100 (F)

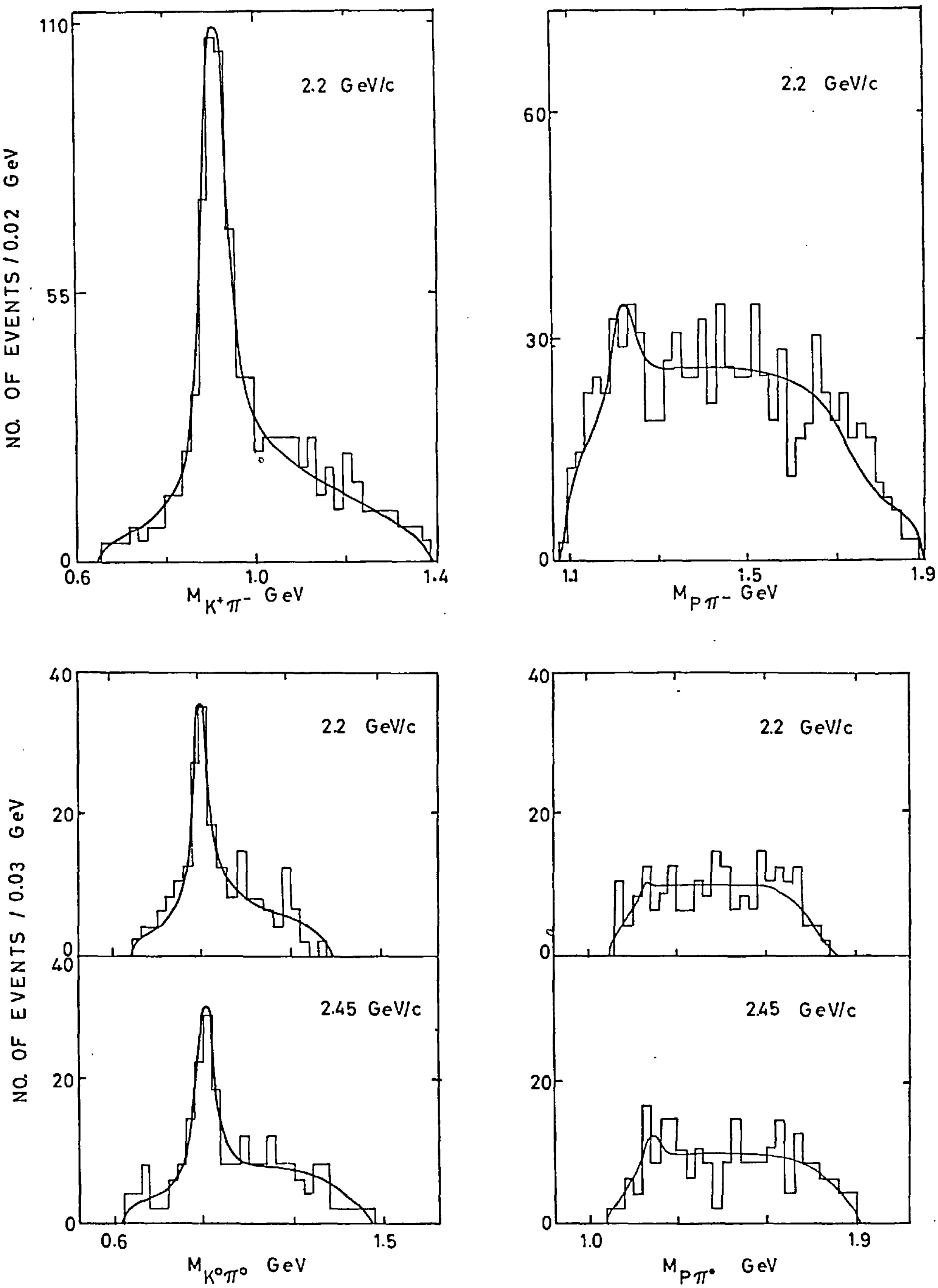
110
55
0
NO. OF EVENTS / 0.02 GeV
2.2 GeV/c
0.6
1.0
1.4
$M_{K^+\pi^-}$ GeV
60
30
0
2.2 GeV/c
1.1
1.5
1.9
$M_{P\pi^-}$ GeV
40
20
0
NO. OF EVENTS / 0.03 GeV
2.2 GeV/c
2.45 GeV/c
0.6
1.5
$M_{K^\circ\pi^\circ}$ GeV
2.2 GeV/c
2.45 GeV/c
1.0
1.9
$M_{P\pi^\circ}$ GeV

FIGURE 14.

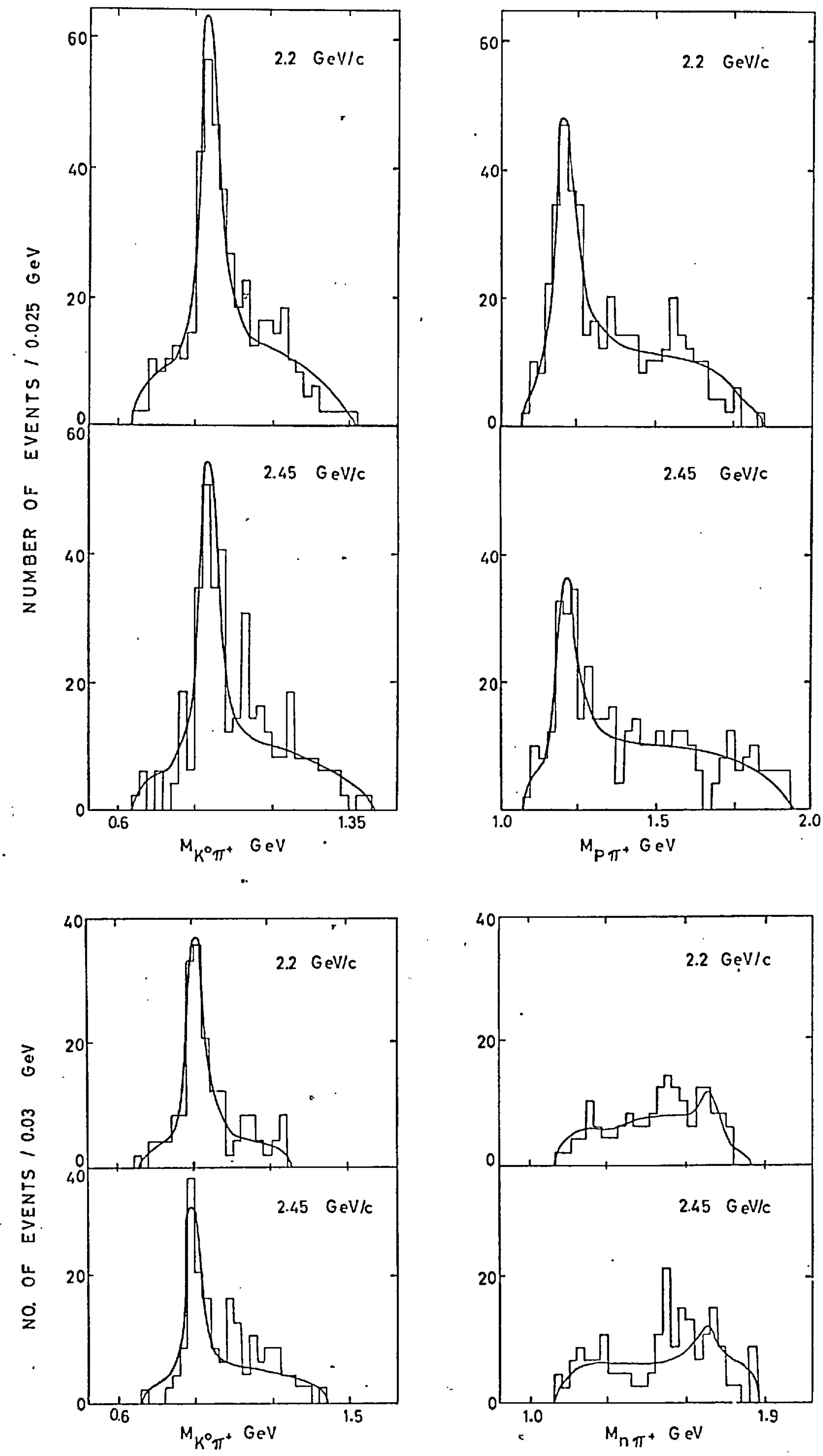

FIGURE 14 (cont.)

the fit describes the data, we have displayed in fig. 14 the two effective mass projections of the Dalitz plots along with the projection of the fits.

6.3 Quasi two body cross sections:

The results of the Dalitz plot fitting in the previous section have been used to calculate the quasi two body cross sections from the product of the proportion of resonance production in the quasi two body reaction and the total cross section of the channel. The results are given in table V.

Table V. Quasi two body cross sections.

Reactions	Cross sections (mb)	
	$P = 2.2$ GeV/c	$P = 2.45$ GeV/c
$K^+n \to K^{*o}(K^+\pi^-)p$	1.67 ± 0.16	—
$\to \Delta^o\ (p\pi^-)K^+$	$.29\pm0.06$	—
$K^+n \to K^{*o}(K^o\pi^o)p$	$.88\pm0.13$	$.51\pm0.09$
$\to \Delta^+\ (p\pi^o)K^o$	$.10\pm0.08$	$.19\pm0.07$
$K^+n \to K^{*+}(K^o\pi^+)n$	$.97\pm0.15$	$.57\pm0.09$
$\to \Delta^+(n\pi^+)K^o$	$.05\pm0.06$	$.06\pm0.05$
$\to N^{*+}(n\pi^+)K^o$	$.17\pm0.07$	$.12\pm0.06$
$K^+p \to K^{*+}(K^o\pi^+)p$	1.47 ± 0.18	1.11 ± 0.13
$\to \Delta^{++}(p\pi^+)K^o$	1.40 ± 0.18	$.90\pm0.12$

We note that the Clebsch-Gordan coefficients for the decay of isospin-$\frac{1}{2}$ K^{*o} into $K^+\pi^-$ and $K^o\pi^o$ predict $\frac{K^{*o} \to K^+\pi^-}{K^{*o} \to K^o\pi^o} = 2.$

The experimental value, $1.9\pm.3$ is in excellent agreement with the isospin prediction.

6.4 $K^*(892)$ production and decay:

The $K^*(892)$ events referred to here come from the reactions

$$K^+n \rightarrow K^{*0}(892)p \quad (K^{*0} \rightarrow K^+\pi^-) \tag{6-10}$$
$$K^+n \rightarrow K^{*0}(892)p \quad (K^{*0} \rightarrow K^0\pi^0) \tag{6-11}$$
$$K^+n \rightarrow K^{*+}(892)n \quad (K^{*+} \rightarrow K^0\pi^+) \tag{6-12}$$
$$K^+p \rightarrow K^{*+}(892)p \quad (K^{*+} \rightarrow K^0\pi^+) \tag{6-13}$$

where the events with $(K\pi)$ effective mass lies between 0.85 GeV and 0.95 GeV. The last reaction is a pure T=1 channel which has been extensively studied in hydrogen experiment at nearby energies. The other three reactions are a mixture of T=0 and T=1 isospin states. The study of K^+p reaction from K^+d interactions alongside K^+n reactions is a useful one in view of the fact that one already knows a lot of things about $K^{*+}(892)$ from hydrogen experiments.

The production and decay of $K^*(892)$ in the quasi two body reaction can provide us with very useful information about the reaction mechanism for these different processes. So the following sections we will devote to their production and decay studies in some details.

6.4.1 $K^*(892)$ production angular distributions:

The production angle is defined in the K^+N rest frame (the rest frame of the four vector $[P_K+P_d-P_{sp}]$) as the angle between the incoming K^+ beam and the outgoing $(K\pi)$ momentum vector.

a) <u>$dN/d(\cos\theta^*)$ and Legendre polynomial analysis</u>:

The experimental production angular distributions for K^* produced in the four reactions are shown in fig. 15. These are clearly peripheral. One should, however, remember at this point that the dominance of peripheral mechanism is not inconsistent with the existence of the direct channel Z^* resonance because, as from the notion of duality(36), these two descriptions are related in an average way to one another.

The angular distributions were fit with expansions in Legendre polynomials of order n_{max}(fig. 15):

$$\frac{dN}{d(\cos\theta^*)} = \text{const.} \sum_{n=1}^{n_{max}} A_n P_n(\cos\theta^*) \qquad (6\text{-}14)$$

where the coefficients A_n's are related to the partial waves and the number of coefficients in a particular scattering indicates what partial waves must be present to describe the scattering. In the expression above the highest order n_{max} $=2l_{max}$(if n_{max} even) or $=2l_{max}-1$ (if n_{max}odd), where l_{max} is the highest orbital angular momentum. Even A_n's are contributed by the pure waves of the same parity, and the odd A_n's are contributed by only the interference of partial waves of opposite parity.

For simplicity one calculates the normalized coefficients, A_n/A_o, where A_o is related to the partial cross section. The coefficients obtained by the method of moments are shown in table VI. In $K^+n \rightarrow K^{*o}p$, coefficients upto A_8

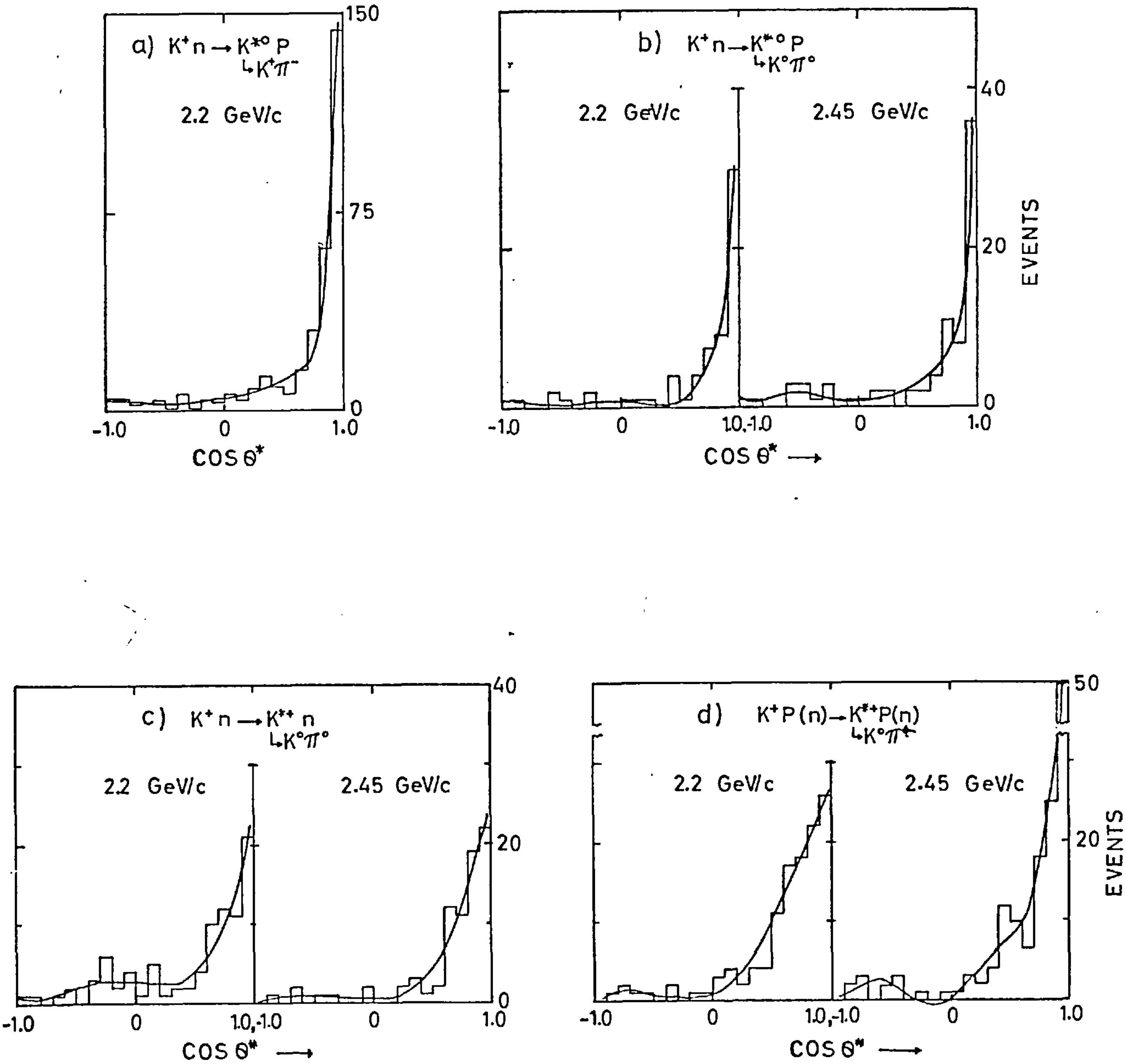
a) $K^+n \to K^{*o}P$ $\hookrightarrow K^+\pi^-$
2.2 GeV/c
150
75
0
-1.0
0
1.0
COS θ*
b) $K^+n \to K^{*o}P$ $\hookrightarrow K^o\pi^o$
2.2 GeV/c
2.45 GeV/c
40
20
0
EVENTS
-1.0
0
1.0,-1.0
0
1.0
COS θ* ⟶
c) $K^+n \to K^{*+}n$ $\hookrightarrow K^o\pi^o$
2.2 GeV/c
2.45 GeV/c
40
20
0
-1.0
0
1.0,-1.0
0
1.0
COS θ* ⟶
d) $K^+P(n) \to K^{*+}P(n)$ $\hookrightarrow K^o\pi^+$
2.2 GeV/c
2.45 GeV/c
50
20
EVENTS
-1.0
0
1.0,-1.0
0
1.0
COS θ* ⟶

FIGURE 15.

TABLE VI.

Legendre Polynomial coefficients (A_n/A_o).

Reactions / A_n/A_o \ p_{Lab} (GeV/c)	$K^+n \to K^{*o}(K^+\pi^-)p$	$K^+n \to K^{*o}(K^o\pi^o)p$		$K^+n \to K^{*+}(K^o\pi^+)n$		$K^+p \to K^{*+}(K^o\pi^+)p$	
	2.2	2.2	2.45	2.2	2.45	2.2	2.45
A_1/A_o	2.04 ± .08	1.99 ± .22	1.78 ± .20	1.47 ± .16	2.01 ± .13	1.82 ± .12	1.96 ± .12
A_2/A_o	2.54 ± .14	2.72 ± .32	2.30 ± .30	1.19 ± .26	2.07 ± .23	1.54 ± .20	2.12 ± .20
A_3/A_o	2.49 ± .19	2.60 ± .44	2.46 ± .39	1.16 ± .31	1.35 ± .34	.52 ± .27	1.55 ± .29
A_4/A_o	2.27 ± .23	2.28 ± .55	1.91 ± .49	.60 ± .38	.35 ± .43	-.29 ± .32	.88 ± .34
A_5/A_o	1.92 ± .27	1.10 ± .66	1.44 ± .55				1.00 ± .37
A_6/A_o	1.40 ± .31	.98 ± .70	1.65 ± .57				.81 ± .43
A_7/A_o	.93 ± .34	.48 ± .77	1.30 ± .61				
A_8/A_o	.63 ± .46	.48 ± .83	.89 ± .65				

are needed to describe the data as is evident from the highly forward-peaked distributions. But only coefficients upto A_4 are needed to describe both $K^+p \to K^{*+}p$ and $K^+n \to K^{*+}n$ production angular distributions at 2.2 GeV/c which correspond to only S, P and D waves. The distribution for $K^+p \to K^{*+}p$ becomes more peripheral at 2.45 GeV/c as evident from the need for more coefficients. Hirata[10] also noted that the peripheralism increases with increasing energy right from the threshold. The coefficients for this particular reaction are available at nearby energies[9]. From the energy dependence of these coefficients, one can have idea regarding the behaviour of various partial waves. So the first four coefficients are plotted as a function of incident beam momentum in fig. 16 . As can be seen A_1, A_2, A_3 all appear to vary smoothly over the momentum range and show no qualitative evidence for an s-channel resonance upto 3 GeV/c. But this regular behaviour is not obeyed by A_4 coefficient which shows a dip around 2 GeV/c and then rises again. The extent of this structure depends on 1.97 GeV/c point. Assuming the presence of the structure a rudimentary partial wave analysis has been done by G. Thompson[12] and the candidates that would cause such structure are shown to be due to PP1, FP5 and PF3. It is to be noted here that the last mentioned candidate is compatible with the resonating inelastic $P\frac{3}{2}$ wave as proposed by the phase shift analysis of Asbury et al[37].

Last year in the Amsterdam International Conference two more experiments[38,39] reported A_n/A_o's of $K^{*+}p$ production. The data of Loken et al.[38] have given rise to doubts

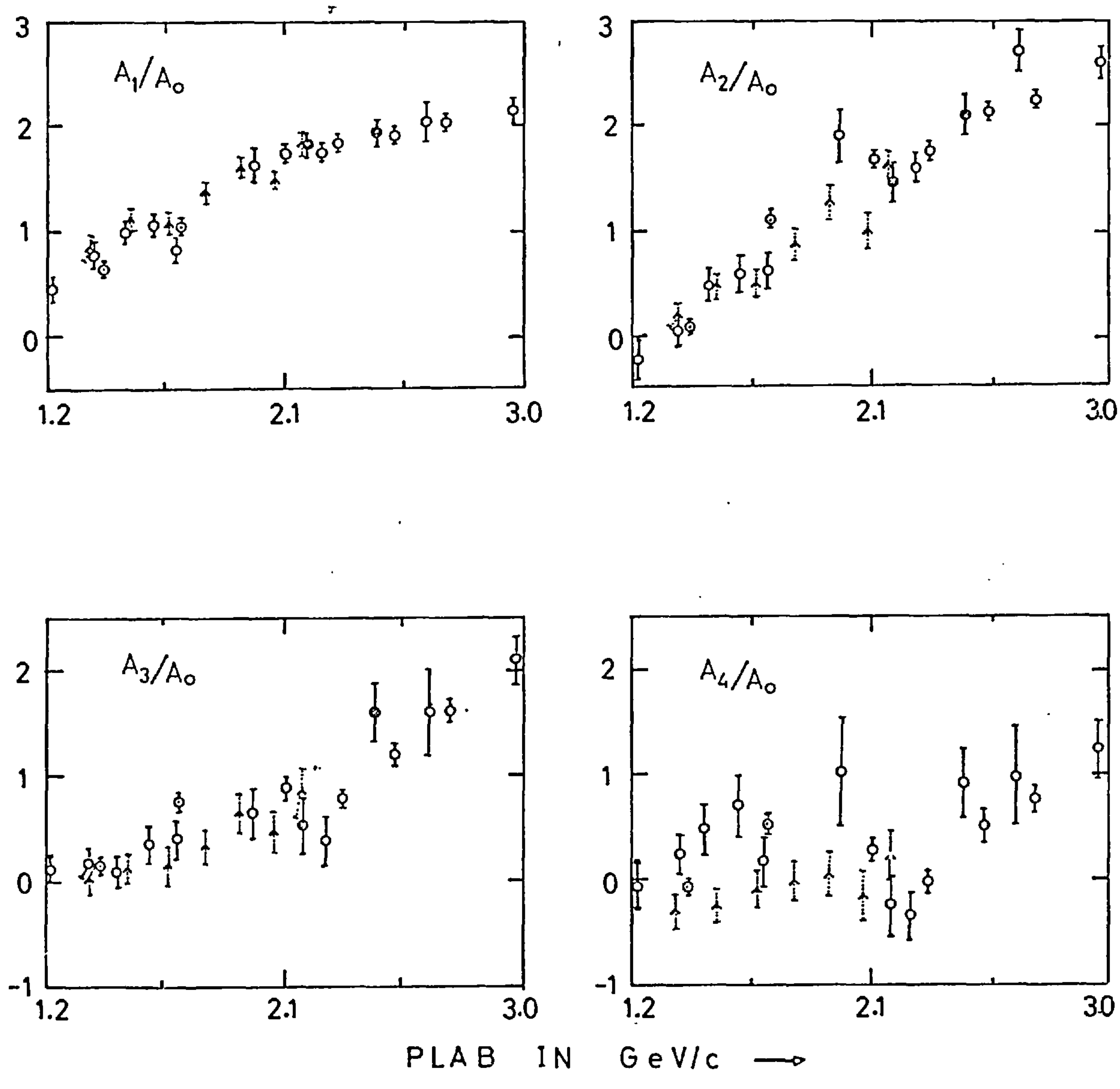

FIGURE 16.

as to the existence of the above mentioned structure. But points at 1.4 and 1.7 GeV/c from the very high statistics experiment of Lesquoy et al.[39] agree within errors with the old data points and the second data point (i.e. A_4 at 1.7 GeV/c) certainly disagrees with the values of A_4 around this energy reported by the relatively small statistics experiment of Loken et al. The A_4/A_0 values given by the latter experiment are all below zero or consistent with zero from 1.37 to 2.07 GeV/c. Inspite of large errors our new $K^{*+}p$ data points at 2.18 and 2.43 GeV/c favour the presence of the dip if the old data points, more crucially the 1.97 GeV/c point, are correct. Also the two $K^{*+}n$ data points are not incompatible with the $K^{*+}p$ points and so it is possible that the effect is also present in $K^+n \rightarrow K^{*+}n$. Further statistics (an increase by an order of magnitude) will become available when the present experiment is completed. It would then be possible to make more detailed statements about the state of affairs in the energy region of interest. But more data between 1.5 and 2.2 GeV/c with increased statistics should certainly be made available to finally prove or disprove the existence of the structure.

b) Momentum transfer distributions: ($d\sigma/dt$)

The other way of studying the production of $K^*(892)$ is by looking at the $d\sigma/dt$ distributions. From the Chew-Low plots (not shown) we find $K^*(892)$ to be produced peripherally with some non K^* events at low -t values. In fig. 17 we show the $d\sigma/dt$ distributions for different $K^*(892)$ productions. Since the shapes of these distributions are not distorted noticeably by the few background events, we did not attempt to correct for the non K^* background events. The neutral K^{*o} events show forward peaking and a faster fall with $-t$ whereas the charged K^{*+} show decrease of cross section at $-t \simeq 0$ and a broad spectrum. At 2.2 and 2.45 GeV/c, the minimum momentum transfers, $-t_m$ from the incoming K^+ to the $(K\pi)$ combination (taking central mass value of 0.892) are $\simeq 0.02$ and $\simeq 0.015$ GeV^2 respectively. The slight reduction in the differential cross sections for K^{*o} near $-t \simeq 0$ (fig. 17b) is completely removed when the distributions in $|t'| = |t-t_m|$ are considered (not shown). But for the charged K^{*+} production the forward turnover still remains even for the $d\sigma/dt'$ distributions (not shown). Since $K^*(892)$ is not a broad resonance the shapes for $d\sigma/dt$ and $d\sigma/dt'$ distributions are not expected to be much different (e.g. $K^{*o} \rightarrow K^+\pi^-$ slopes at small $-t$ are 7.05 and 7.1 GeV^{-2} for the $d\sigma/dt$ and $d\sigma/dt'$ distributions respectively). The dip or atleast the shoulder near $-t \simeq 0$ for K^{*+} is indicative of vector exchange process because if a reaction proceeds by exchange of vector or tensor meson, the spin flip is important and the differential cross section varies as $\sin\frac{\theta}{2}$. This turnover is a feature of physical process as mentioned, and is not associated with scanning loss or spectator identification problem. Other experiments also observed similar turnover at $-t \simeq 0$ (40).

Inspite of such small dip or flattening of the $d\sigma/dt$ distributions for K^{*+} production at very low $-t$, we can still consider them as having broad peaks. Thus the forward peak

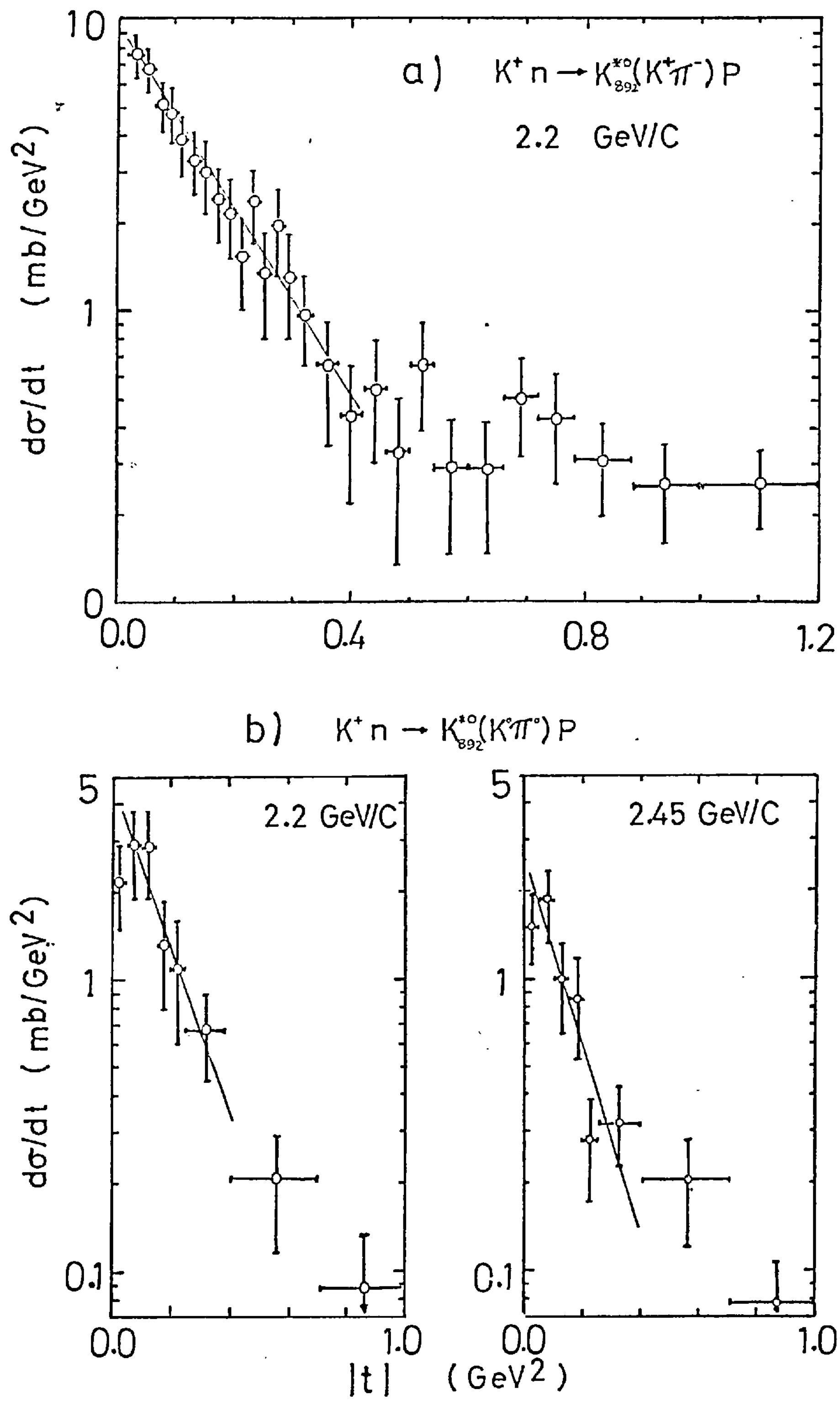

a) $K^+ n \to K^{*0}_{892}(K^+\pi^-) P$
2.2 GeV/C
$d\sigma/dt$ (mb/GeV^2)
10
1
0
0.0
0.4
0.8
1.2
b) $K^+ n \to K^{*0}_{892}(K^0\pi^0) P$
2.2 GeV/C
2.45 GeV/C
$d\sigma/dt$ (mb/GeV^2)
5
1
0.1
0.0
1.0
|t| (GeV^2)

FIGURE 17

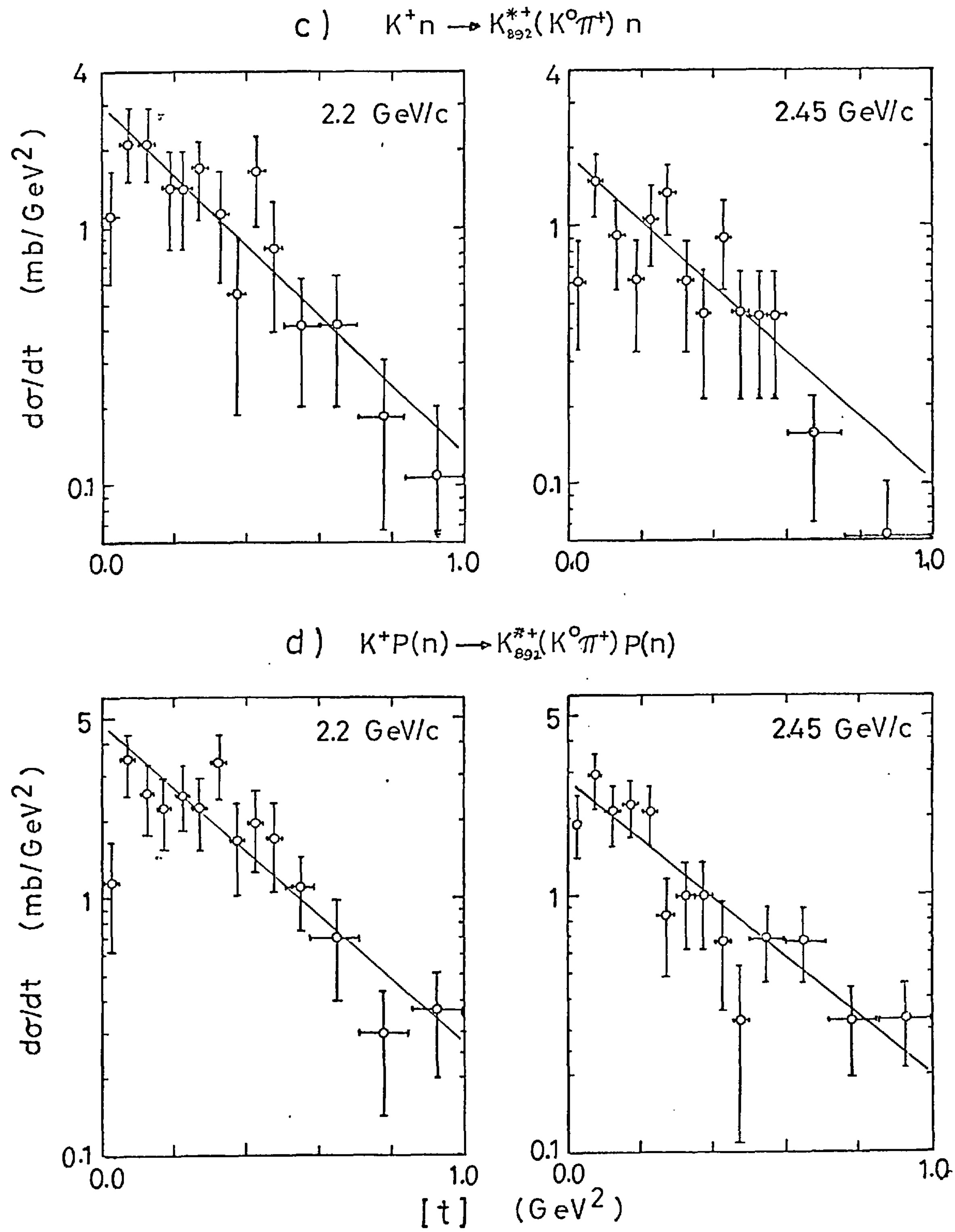
c) $K^+n \rightarrow K^{*+}_{892}(K^0\pi^+)\,n$
2.2 GeV/c
2.45 GeV/c
d) $K^+P(n) \rightarrow K^{*+}_{892}(K^0\pi^+)\,P(n)$
2.2 GeV/c
2.45 GeV/c
dσ/dt (mb/GeV²)
[t] (GeV²)

FIGURE 17.

of all K^* production, regarded as "diffraction peak", are described quite well at low t by a function of the form

$$\frac{d\sigma}{dt} = A\ e^{Bt} \qquad (6\text{-}15)$$

The intercepts and slopes obtained by fitting the data with the above function are given in table VII below and the fitted curves are shown superimposed on the respective $d\sigma/dt$ distribution (figs. 17a - d).

Table VII. Intercepts and slopes of $\frac{d\sigma}{dt}(K^*)$.

t range used: $|t_m| \leqslant |t| \leqslant |t_u|$.

Reactions	PLAB GeV/c	$-t_u$ GeV^2	Intercepts A (mb/GeV^2)	slopes B GeV^{-2}	χ^2/NDF
$K^+n \to K^{*o}p$, $\hookrightarrow K^+\pi^-$	2.2	0.42	9.2 ± 1.0	$7.05 \pm .39$	5.3/15
$K^+n \to K^{*o}p$, $\hookrightarrow K^o\pi^o$	2.2	0.42	4.9 ± 1.3	6.2 ± 1.4	2.1/4
	2.45	0.42	2.7 ± 1.2	$7.2 \pm .96$	2.5/4
$K^+n \to K^{*+}n$, $\hookrightarrow K^o\pi^+$	2.2	1.0	3.0 ± 1.2	$3.0 \pm .56$	7.8/12
	2.45	1.0	1.7 ± 1.2	$2.7 \pm .57$	14.0/12
$K^+p \to K^{*+}p$, $\hookrightarrow K^o\pi^+$	2.2	1.0	4.5 ± 1.2	$2.6 \pm .40$	12.5/12
	2.45	1.0	3.0 ± 1.1	$2.7 \pm .33$	9.7/12

The slopes for $K^{*o}(892)$, known to be produced through pseudoscalar exchange, are larger than those for $K^{*+}(892)$ production where vector exchange is dominant.

6.4.2 $K^{*}(892)$ decay:

The decay angular characteristics of the $(K\pi)$ system are usually expressed in the $(K\pi)$ rest system instead of the overall c.m. system. Here we shall use the Gottfried-Jackson frame (see section 6.4.2c). The resonance decay distribution is expressed in terms of the polar and azimuthal angles, θ_J and Φ made by one of the decay products, say the K-meson. The angle θ_J and Φ are commonly called the Jackson and Treiman-Yang angles respectively.

a) Cos θ_J and Φ distributions:

In fig. 18 we present the distributions of $\cos\theta_J$ and Φ for different K^{*} production reactions, where only events with $-t \leq 1.0$ GeV^2 are shown. The Treiman-Yang distributions have been folded in Φ according to parity conservation in the decay of K^{*}. The solid (and the dashed) curves correspond to the density matrix elements determined by the method of moments as described later. The polar decay angular distributions of the neutral K^{*o} vary mainly as $\cos^2\theta_J$, whereas those of K^{*+} are predominantly $\sin^2\theta_J$. But the azimuthal decay angular distributions of K^{*o} are rather flat while those of K^{*+} are clearly nonflat and each of them displays an inverted parabola.

b) Asymmetry and moments across the $K\pi$ mass:

In view of relatively large sample of events we will consider here only the $K^+n \rightarrow K^+\pi^-p$ final state. The fact that the $\cos\theta_J$ distribution of K^{*} prominently in the above

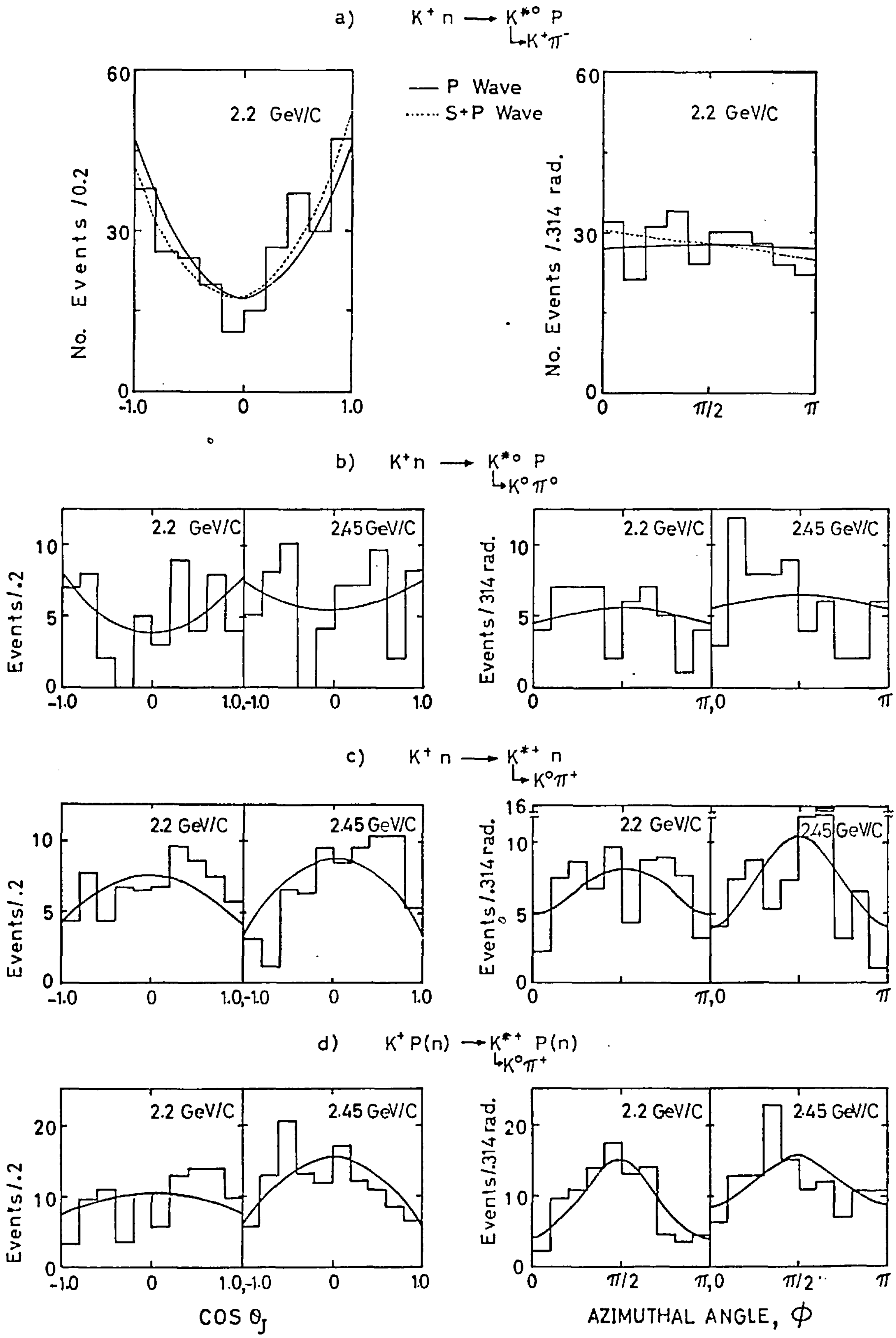
a) K⁺ n → K*° P
↳K⁺π⁻
— P Wave
······ S+P Wave
2.2 GeV/C
No. Events /0.2
No. Events /.314 rad.
b) K⁺n → K*° P
↳K°π°
2.2 GeV/C
2.45 GeV/C
Events/.2
Events/.314 rad.
c) K⁺ n → K*⁺ n
↳K°π⁺
d) K⁺ P(n) → K*⁺ P(n)
↳K°π⁺
COS θ_J
AZIMUTHAL ANGLE, φ

FIGURE 18.

reaction is peaked in the forward direction indicates the presence of other wave or waves of the ($K\pi$) system in the $K^*(892)$ region. This asymmetry is not certainly due to statistical fluctuations. The Dalitz plot also shows that the $\Delta^0(1236)$ production is very small. So the possibility of the asymmetry resulting from the reflection of $\Delta^0(1236)$ can immediately be ruled out.

The asymmetry parameter, α is defined as

$$\alpha = \frac{F - B}{F + B} \tag{6-16}$$

where F and B are the numbers of events in the forward and backward hemispheres respectively of the $\cos\theta_J$ distribution. We show α as a function of the ($K\pi$) effective mass in fig. 19a. As can be observed the asymmetry parameter becomes positive just after ($K\pi$) threshold, stays rather large and then changes sign at $M(K^+\pi^-) \simeq 0.930$ GeV. It becomes positive again at about 1.07 GeV. The same behaviour of the asymmetry parameter was observed in the same reaction at 2.3 GeV/c(7), 3.0 GeV/c(41), 4.6 GeV/c(42), 9.0 GeV/c(43) and 12 GeV/c(44) and also in other reactions, for example, in $K^-p \rightarrow K^-\pi^+n$ at 3.0 GeV/c(45), 3.9, 4.6 GeV/c(46) and in $K^+p \rightarrow K^+\pi^-\Delta^{++}$ at 9 incident beam momenta(9,47). Thus it is clear that the asymmetry does not depend on the reaction considered. With our limited statistics it is difficult to see clearly the trend of ($K^0\pi^0$) data from the $K^+n \rightarrow K^0\pi^0p$ channel (not shown) but it has been shown in the case of $K^+p \rightarrow K^0\pi^0\Delta^{++}$(45) that the asymmetry α has the same general behaviour but is significantly different, i.e. the similarity vanishes for

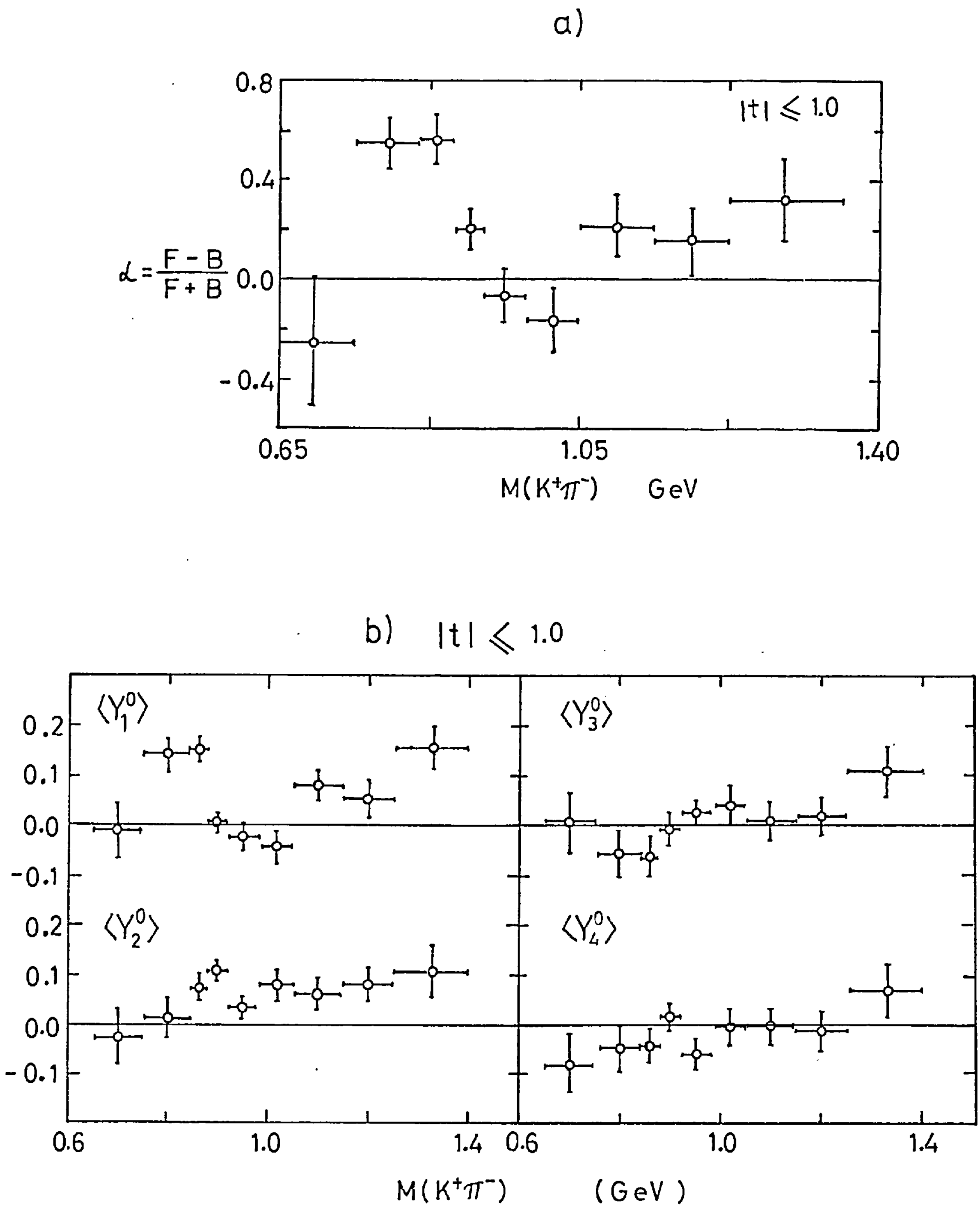
a)
0.8
0.4
0.0
- 0.4
$\alpha = \frac{F - B}{F + B}$
$|t| \leqslant 1.0$
0.65
1.05
1.40
$M(K^+\pi^-)$ GeV
b) $|t| \leqslant 1.0$
$\langle Y_1^0 \rangle$
$\langle Y_2^0 \rangle$
$\langle Y_3^0 \rangle$
$\langle Y_4^0 \rangle$
0.2
0.1
0.0
-0.1
0.6
1.0
1.4
$M(K^+\pi^-)$ (GeV)

FIGURE 19.

$M(K\pi) \gtrsim 0.95$ GeV where $\alpha > 0$ for $K^+\pi^-$ and $\alpha < 0$ for $K^0\pi^0$.

The $K\pi$ amplitudes in terms of pure isotopic spin amplitudes are:

$$F_{el} = \frac{2}{3} \left(T_{\frac{1}{2}} + \frac{1}{2} T_{3/2} \right)$$
$$F_{ce} = -\frac{\sqrt{2}}{3} \left(T_{\frac{1}{2}} - T_{3/2} \right)$$

Thus we see that isotopic spin 3/2 contributes more to the charge exchange than to the elastic amplitude. So the difference between the $(K^{\pm}\pi^{\mp})$ and the $(K^0\pi^0)$ system may be explained by the non negligible contribution of the isospin 3/2 amplitude. A qualitative explanation of the observation can be given by assuming a modest negative $\beta_s^{3/2}$ of about, say, -20^o(48) — F^s_{ce} will then lag behind F^s_{el} in phase when $\beta_s^{\frac{1}{2}} \simeq 90^o$ which results in a smaller algebraic value for $\mathrm{Re}(F^S F^{P*})$ and hence α for $K^0\pi^0$ on the high side of $K^*(892)$.

Let us further explore the asymmetric $(K\pi)$ system in terms of the spherical harmonic moments. The $K^*(892)$ decay angular distribution should give rise to non-zero spherical harmonic moments only for $\langle Y_2^0 \rangle$, $\langle \mathrm{Re} Y_2^1 \rangle$, $\langle \mathrm{Re} Y_2^2 \rangle$ etc. but an S-wave $(K\pi)$ background interfering with the resonant P-wave amplitude would produce non-zero $\langle Y_1^0 \rangle$ (or, $\langle \mathrm{Re} Y_1^1 \rangle$) and a P-D wave interference will show up in $\langle Y_3^0 \rangle$. For $K^{*0} \rightarrow K^+\pi^-$ we have calculated the m=0, l=1,2,3,4 spherical harmonics as a function of the $(K^+\pi^-)$ effective mass using

$$\langle Y_1^0 \rangle = \frac{1}{N} \sum_{i=1}^{N} Y_1^0 (\theta_i, \Phi_i) \qquad (6\text{-}17)$$

and show these in fig. 19b . From these it can be seen that the region of $K^{*o}(892)$ is dominated by P-wave but the non vanishing $\langle Y_1^0 \rangle$ moment indicates the existence of a peripheral S-wave background interfering with this P-wave. The higher moments $(l=3,4)$ are of no significance and found to be consistent with zero around $K^{*o}(892)$. Therefore a P-D wave interference can be thought to be negligible in the $K^{*o}(892)$ region.

The S-wave phase shift $\beta_s^{\frac{1}{2}}$ (ignoring the 3/2 component) can roughly be calculated by noting that $\langle Y_1^0 \rangle$ goes to zero around $M(K^+\pi^-) = 0.930$ GeV. This gives $\mathrm{Cos}(\beta_p-\beta_s) \cong 0$ at $M(K^+\pi^-) \simeq 0.930$ GeV —— and also one gets $\beta_p \cong 150^o$ if one assumes P-wave to have a Breit-Wigner shape centred at 0.892 GeV with a width of 50 MeV. Hence there are two solutins for β_s, e.g. $\simeq 60^o$ and $\simeq 210^o$ corresponding to $\beta_p \cong 150^o$.

The experimental observation that there exists an S-wave $K\pi$ interaction in the $K^*(892)$ region has been established some time ago(49). Since then attempts have been made to establish it as a resonance and to find its properties, e.g. mass, width etc. Many phase shift analyses have been performed and two acceptable ambiguous solutions are obtained(50). One of them is a sharp resonance near the $K^*(892)$ and the other rises monotonically to 60^o at 1.1 GeV. Very recently D. Cords et. al.(51) claimed that they found (independent of any particular assumption of the production mechanism) unambiguous evidence for a broad S-wave enhancement at 1.3 GeV and interpret the enhancement as resonance of $M = 1.305 \pm .03$ GeV and $\Gamma = 0.330 \pm .06$ GeV. Soon much more data will be available from this experiment at 2.2, 2.45 and 2.7 GeV/c, and a more detailed study of the $K\pi$ interaction is postponed until this data is available.

c) Density Matrix elements (no interference):

The decay angular distribution for $K^*(892)$ allows us to measure the density matrix elements ρ_{oo}, $\rho_{1,-1}$ and $Re\,\rho_{10}$. Assuming that the $K^*(892)$ is dominated by P-wave the $K^*(892)$ decay distribution in terms of the density matrix elements is given by

$$W(Cos\theta,\Phi) = \frac{3}{8\pi}\Big[(1-\rho_{oo})+(3\rho_{oo}-1)Cos^2\theta - 2\rho_{1,-1}Sin^2\theta\, Cos2\Phi - 2\sqrt{2}\, Re\rho_{10}\, Sin2\theta\, Cos\Phi\Big] \qquad (6\text{-}18)$$

The $Cos\theta$ and Φ projections are

$$W(Cos\theta) = \frac{3}{4}\Big[(1-\rho_{oo})+(3\rho_{oo}-1)Cos^2\theta\Big] \qquad (6\text{-}18a)$$

$$W(\Phi) = \frac{1}{2\pi}\Big[(1+2\rho_{1,-1})-4\rho_{1,-1}Cos^2\Phi\Big] \qquad (6\text{-}18b)$$

The method of moments has been used to obtain ρ_{oo}, $\rho_{1,-1}$ and $Re\rho_{10}$ as a function of t and integrated over all t.

For $K^{*o} \to K^+\pi^-$, we have determined the elements ρ_{ij} using different quantization axis (different frame) e.g;[41]

a) Gottfried-Jackson (t-channel) system: z-axis is the direction of the incident K^+ in the K^* rest system.

b) Helicity (s-channel) system: z-axis is the direction of the K^* in the overall K^+n c.m. system.

c) Adair System : z-axis is the direction of the incident K^+ in the overall K^+n c.m. system.

In all these cases, the y-axis is always normal to the production plane and the x-axis is given by $\hat{x} = \hat{y} \times \hat{z}$. The decay angles θ, ϕ are the polar and azimuth angles of the direction of flight, $\hat{k}$ of the outgoing K^+ in the K^* rest system.

The density matrix elements evaluated in the Jackson (ρ^J_{ij}), Helicity (ρ^H_{ij}) and Adair (ρ^A_{ij}) frames are shown in table VIII. One should note here that t- and s-dependent structures e.g. dips, breaks etc. of t- and s-channel amplitudes will be reflected in ρ^J_{ij} and ρ^H_{ij} respectively[52]. Our density matrix elements in any of these frames do not show any obvious structures -- atleast not detectable with the present data. In s- and t-channel frames, we see that ρ_{00} decreases with increasing $|t|$ — ρ^H_{00} decreasing faster than ρ^J_{00}. But in the Adair system ρ^A_{00} does not vary much over the t-range considered. It should be pointed out here that $(\rho_{11}+\rho_{1,-1})$ has the same value in the three frames since the y-axis is the same in all these three reference frames[53]. For $-t \lesssim 1.0$ GeV^2 the values are $0.22 \pm .039$, $0.22 \pm .04$ and $0.226 \pm .039$ in the Jackson, Helicity and Adair systems respectively.

For the $K^{*0} \to K^0\pi^0$ case we have determined the density matrix elements averaged over $0.0 \lesssim -t \lesssim 1.0$ GeV^2 only in the Jackson system and these are shown in table IX.

The density matrix elements for the K^{*+} produced in the K^+n and K^+p channels, calculated only in the Jackson frame, are given in table X. In the K^+p channel we have followed the suggestion of Eberhard and Pripstein[54] in order to avoid any bias that may influence the K^* angular

TABLE VIII

Density Matrix elements in different systems.

$$K^+n \rightarrow K^{*o}\,p \quad K^{*o} \rightarrow K^+\pi^-$$

(P-wave: No interference)

-t interval (GeV^2)	JACKSON ρ_{oo}	JACKSON ρ_{1-1}	JACKSON $Re\rho_{10}$	HELICITY ρ_{oo}	HELICITY ρ_{1-1}	HELICITY $Re\rho_{10}$	ADAIR ρ_{oo}	ADAIR ρ_{1-1}	ADAIR $Re\rho_{10}$
.02-.07	.560±.087	.038±.070	-.147±.055	.619±.095	.049±.07	.008±.049	.606±.090	.061±.069	.063±.056
.07-.15	.608±.09	.061±.064	-.183±.049	.602±.085	.059±.065	-.201±.05	.742±.086	.128±.059	-.044±.053
.15-.30	.568±.095	-.068±.071	-.167±.058	.449±.093	-.122±.069	-.197±.055	.692±.095	-.001±.061	-.067±.057
.30-1.0	.544±.094	-.019±.068	-.146±.052	.178±.081	-.179±.078	-.077±.053	.574±.087	.019±.064	-.089±.056
.02-1.0	.571±.045	.005±.033	-.161±.026	.463±.045	-.048±.035	-.117±.027	.654±.045	.053±.032	-.034±.028

Table IX. Jackson system density matrix elements
$K^+n \rightarrow K^{*o}(K^o\pi^o)\ p$. P-wave.

PLAB (GeV/c)	-t interval (GeV2)	ρ_{oo}	$\rho_{1,-1}$	Re ρ_{10}
2.2	0.0 - 1.0	$.52\pm.11$	$.06\pm.08$	$-.09\pm.06$
2.45	0.0 - 1.0	$.40\pm.09$	$.04\pm.07$	$-.13\pm.06$

distribution from the overlap of the $\Delta^{++}(1236)$ band. In order to carry out this, we have excluded the events altogether which lie in the overlap region and the loss of events is corrected for by repopulating the overlap region with conjugate events, the pure K^* i.e. the parity reversed region of the overlap region with the kaon and the pion interchanged in the rest frame of the K^*. The values of density matrix elements using this method and raw data are shown in table X as upper and lower entries. The elements are found to be compatible with those found for the same reaction in K^+p interactions[9].

It is interesting to note that the energy dependence of the density matrix element ρ_{oo} for the reaction $K^+p \rightarrow K^{*+}p$ shows a one standard deviation dip in the 2 to 2.5 GeV/c region[9]. We have plotted in fig. 20 the matrix element ρ_{oo} (obtained from the present experiment and from all other available data) as a function of incident beam momentum. As can be seen our new K^{*+} data on ρ_{oo} is compatible with the above mentioned structure (note, the A_4/A_o structure in the same energy region and also the sharpening of the $\cos\theta_j$

Table X. Jackson system density matrix elements (P-wave).

Reaction	Momentum (GeV/c)	-t interval (GeV^2)	ρ_{00}	$\rho_{1,-1}$	Re ρ_{10}
$K^+n-K^{*+}n$	2.2	.02-1.0	.211±.082	.119±.075	-.020±.056
	2.45	0 - 1.0	.160±.080	.219±.078	-.093±.043
$K^+p-K^{*+}p$	2.2	0 -.20	.513±.126 .626±.124	.262±.094 .276±.085	.025±.074 -.026±.067
		.2-.40	.198±.107 .137±.097	.359±.088 .272±.077	-.124±.053 -.144±.050
		.4-1.0	.050±.099 .066±.091	.287±.121 .120±.111	.102±.068 -.001±.072
		0 -1.0	.270±.069 .285±.066	.301±.059 .224±.050	.000±.040 -.058±.038
		all t	.267±.066 .255±.061	.269±.057 .200±.051	-.038±.039 -.060±.035
	2.45	0 - 1.	.265±.093 .350±.080	.116±.084 .112±.071	-.162±.063 -.232±.054
		.2-.40	-.109±.063 -.094±.060	.102±.137 .098±.131	-.213±.068 -.236±.066
		.4-1.0	.189±.085 .210±.085	.225±.098 .230±.100	.080±.067 .044±.070
		0 - 1.0	.158±.053 .212±.051	.147±.058 .142±.055	-.094±.039 -.151±.038
		all t	.160±.050 .206±.048	.166±.055 .157±.052	-.106±.035 -.150±.035

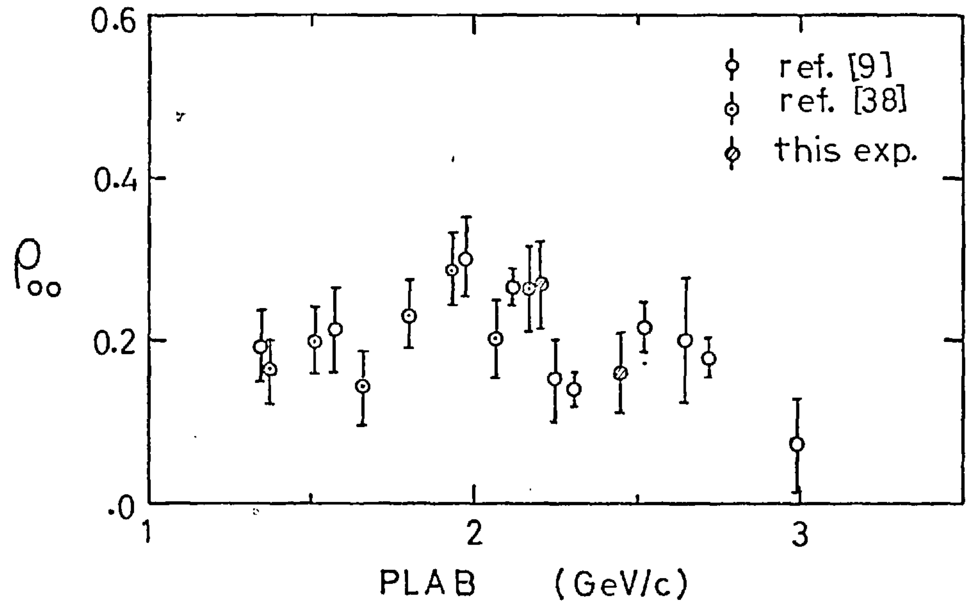

FIGURE 20.

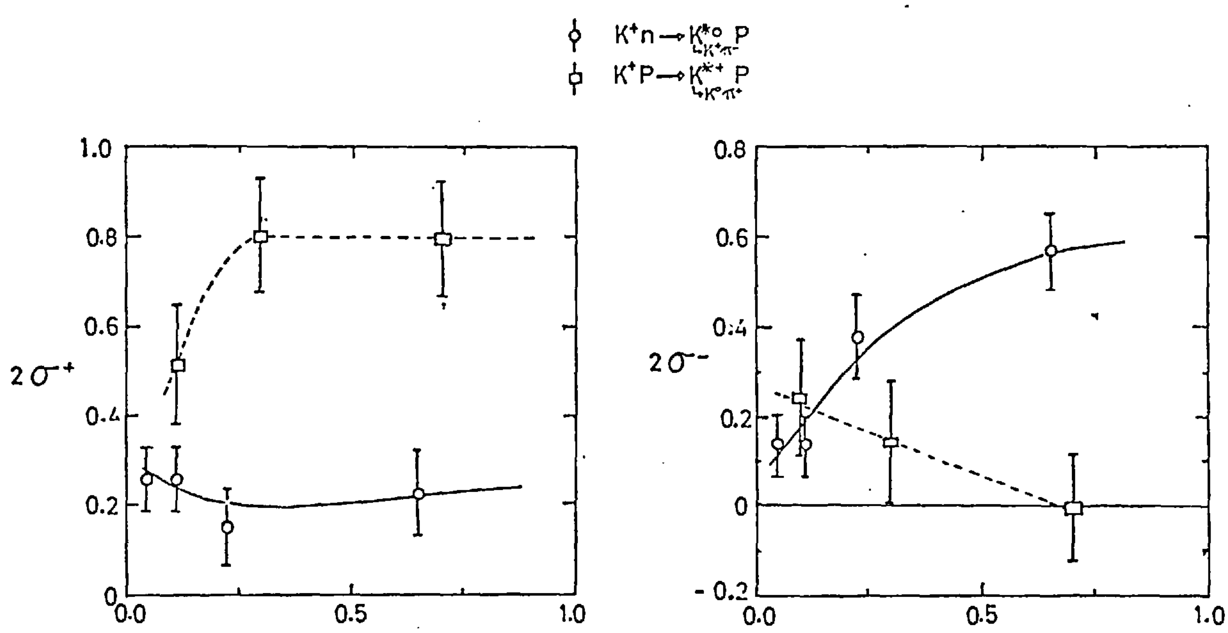

FIGURE 21.

distributions with energy in figs.16 and 18d respectively). The elements ρ_{oo} for the K^{*+} from the reaction $K^+n\to K^{*+}(892)n$ also show the similar trend.

d) $K^{*o}\to K^+\pi^-$ density matrix elements including the S-P wave interference:

As already noted the forward-backward asymmetry observed in the polar angular distribution indicates the S-P wave interference in the $K\pi$ system. So we shall now proceed to include the S-P wave interference in the decay angular distribution of the $(K^+\pi^-)$ system which is given by[41]:

$$W(\text{Cos}\theta,\Phi) = \frac{1}{4\pi}\Big[1+(\rho_{oo}-\rho_{11})(3\text{Cos}^2\theta-1)-3\rho_{1,-1}\text{Sin}^2\theta\ \text{Cos}2\Phi$$
$$-3\sqrt{2}\ \text{Re}\rho_{10}\text{Sin}2\theta\ \text{Cos}\Phi + 2\sqrt{3}\ \text{Re}\rho_{os}\text{Cos}\theta$$
$$-2\sqrt{6}\ \text{Re}\rho_{1s}\text{Sin}\theta\ \text{Cos}\Phi\Big] \tag{6-19}$$

where the S-P wave interference is represented by ρ_{os} and ρ_{1s}. The above distribution can alternatively be expressed in terms of the spherical harmonic moments $\langle Y_l^m\rangle$'s from which one can get

$$\rho_{oo}-\rho_{11} = (5\pi)^{\frac{1}{2}}\langle Y_2^o\rangle$$
$$\rho_{1,-1} = -(10\pi/3)^{\frac{1}{2}}\langle \text{Re}Y_2^2\rangle$$
$$\text{Re}\ \rho_{10} = (5\pi/3)^{\frac{1}{2}}\langle \text{Re}Y_2^1\rangle$$
$$\text{Re}\ \rho_{os} = (\pi)^{\frac{1}{2}}\langle Y_1^o\rangle$$
$$\text{Re}\ \rho_{1s} = (\pi)^{\frac{1}{2}}\langle \text{Re}Y_1^1\rangle$$

The normalization condition is $\rho_{oo}+2\rho_{11}+\rho_{ss}=1$. We do not have any information from $\langle Y_l^m\rangle$ about ρ_{ss}, the S-wave contribution to the angular distribution. So with the help of the trace condition, we removed ρ_{ss} from the expression of the decay distribution and obtained the other elements, e.g. the S-P wave interference elements. The results are given in table XI. The values of $\rho_{1,-1}$ and Re ρ_{10} in the (S+P) wave parameterization are the same as those obtained with the P-wave parameterization; so they are not repeated in the table. We note that the upper limit of ρ_{oo} obtained by putting $\rho_{ss}= 0$ agrees with the value obtained by ignoring the S-P wave interference. The dashed curves shown on the $\mathrm{Cos}\theta_J$ and the Φ distributions in fig. 18 are the fits with S+P waves.

Table XI. Jackson system density matrix elements.
$K^+n \rightarrow K^{*o}(K^+\pi^-)p$; (S+P)-wave. P=2.2 GeV/c.

-t interval (GeV^2)	$\rho_{oo}-\rho_{11}$	Re ρ_{os}	Re ρ_{1s}
.02 - .07	$.339\pm.134$	$.026\pm.065$	$-.011\pm.037$
.07 - .15	$.411\pm.134$	$.013\pm.067$	$-.002\pm.036$
.15 - .30	$.352\pm.142$	$.122\pm.068$	$-.031\pm.042$
.30 - 1.0	$.316\pm.142$	$.085\pm.067$	$-.033\pm.040$
.02 - 1.0	$.356\pm.067$	$.059\pm.033$	$-.019\pm.019$

6.4.3 Comparison between the charged and neutral $K^*(892)$:

The K^*N processes can be divided into the charge exchange (CEX) and non charge exchange (NCEX) reactions, e.g.

CEX , $\Delta Q = +1$ $\quad K^+n \rightarrow K^{*o}p$; $K^{*o} \rightarrow K^{\pm}\pi^{\mp}$

NCEX, $\Delta Q = 0$ $\quad K^+N \rightarrow K^{*+}N$; $K^{*+} \rightarrow K^o\pi^+$ (N=n,p)

As already noted the decay distributions of $K^{*}(892)$ produced in the CEX and NCEX reactions are markedly different. The distribution of the former is indicative of lighter pseudoscalar meson exchange and that of the latter is vector meson exchange. This observation is further supported by the production angular distributions shown earlier. The neutral K^{*o} is seen to have a sharper forward peaking than the charged K^{*+} suggesting that a lighter particle is exchanged in the former and heavier in the latter in the production process. Moreover in the case of charged K^{*+} one observes the characteristic turnover (near small $-t$) associated with vector exchange mechanism.

The density matrix elements determined in the previous section also give evidence for different exchange mechanisms in the two cases, e.g. the value of ρ_{oo} gives an indication of the relative importance of pseudoscalar meson exchange. For π exchange $\rho_{oo} = 1$ and all other elements are zero. But since absorption effects are important ρ_{oo} is less than 1 and non-zero values result for other elements. Thus pion exchange is important in K^{*o} although some vector exchange might be present. But the small value of ρ_{oo} coupled with the large value of $\rho_{1,-1}$ indicates strong contribution from vector meson exchange in the case of the NCEX process.

The isospin character of the exchanged vector meson in the NCEX reactions can be determined by the following arguments. From isospin considerations at the meson vertex we see that isoscalar exchange is forbidden in $K^{+}n \rightarrow K^{*o}p$. If only low mass particles are involved then π, ρ are responsible here. But both isoscalar (ω, ϕ etc.) and isovector (π, ρ etc.) exchange are possible in the case of the NCEX reactions. As pointed out ρ meson exchange is not predominant in the $K^{*o}(892)$ production. Moreover on the basis of isospin argument ρ-exchange contribution is expected to be four times less in the $K^{*+}(892)N$ (N=n,p) production, if we neglect any possible interference effect. Thus the predominant vector exchange contribution to the charged K^{*+} production is indicated to be primarily due to isoscalar 'ω' exchange. This is also consistent with the relativistic SU(6) prediction of couplings[55] that the ρ contribution to $K^{*}(892)$ production cross section is nine times smaller than the contribution from ω exchange. It is to be remarked also that the smallness or absence of ρ exchange provides support for the empirical selection rule of Bronzan and Low[56], called the 'A' parity invariance, which forbids $\rho K K^{*}_{892}$ coupling. The same rule forbids a $\phi K K^{*}_{892}$ coupling as well.

It is also interesting to compare the contributions of natural parity (NP; $P = (-1)^J$) and unnatural parity (UNP; $P = -(-1)^J$) exchanges to the charged and neutral $K^{*}(892)$ production. It has been shown at high energies[57] that, σ^+ and σ^- defined by

$$2\sigma^+ = \rho_{1,1} + \rho_{1,-1}$$

$$2\sigma^- = \rho_{1,1} - \rho_{1,-1}$$

measures the NP and UNP exchange contributions to the production of K^{*} mesons in the helicity one state (note, ρ_{oo} gives the UNP exchange contribution to the helicity zero state). At our incident momentum (only at 2.2 GeV/c) it will still be interesting to estimate the importance of the non-asymptotic contributions, σ^+ and σ^- to the charged and neutral K^*. In fig. 21 we plot σ^+ and σ^- as a function of $-t$ for these two K^* production. We have used the ρ^H_{ij} values and also ignored the S-P wave interference in the calculations. From the figure we note that σ^+ for K^{*+} rises rapidly from $\simeq .5$ to $\simeq .8$ and then stays rather constant; whereas that for K^{*o} is small ($\simeq .2$). As for σ^-, the K^{*o} values are all non-zero being small ($\simeq .14$) upto $-t \simeq .15$ and then start increasing with increasing $-t$; while the K^{*+} values are small and consistent with zero for $-t \gtrsim .2$. In the absence of absorption (Regge cuts) non-zero values for σ^- in the case of K^{*o} would indicate that UNP vector exchange is non-negligible ; whereas small values of σ^- for K^{*+} would indicate UNP vector exchange to be unimportant.

6.4.4 <u>Different exchange model descriptions of $K^+n \rightarrow K^{*o}(892)p$: $\hookrightarrow K^+\pi^-$</u>

The steepness of the $K^{*o}(892)$ differential cross section suggests the dominance of the t-channel one-particle exchange process. From our study of the decay distribution we noted that π exchange is the dominant one in this case. The proximity of the pion pole to the physical $-t$ region clearly shows the importance of the Born term. But the simple Born term propagator does not give us fast falling cross section with $-t$ as demanded by the data. Consequently, various modifications have been made to the simple formula out of which emerges many refined one pion exchange (OPE) models. In the following paragraphs, we shall describe in brief the essential features of the following three models and then compare the experimental results with their predictions:

a) OPE model modified by t-dependent form factors (as used by Durr-Pilkuhn[58]) to take care of the fact that the exchanged pion is off the mass shell.

b) OPE model modified by absorption correction due to other open inelastic channels.

c) OPE model where the exchanged pion is Reggeized.

a) OPE model with Dürr-Pilkuhn form factors(OPEDP):

The contribution of the one pion exchange diagram (fig. 22a) is given by[59]:

$$\frac{d^2\sigma}{dt\,dM^2} = \frac{1}{32\pi^2 k^2 s}\left[T_{K^*\pi K}(M,t)\right]^2 \frac{1}{(t-m_\pi^2)^2}\left[T_{p\pi n}(t)\right]^2 \qquad (6\text{-}20)$$

where k = K^+n c.m. momentum of the incident K^+ particle (mass m_k),

s = square of the total c.m. energy,

t = square of the four-momentum transfer between the K^+ and the $K\pi$ system of effective mass M.

Dürr and Pilkuhn have chosen the suitable kinematical vertex factors $\left|T_{K^*\pi K}(M,t)\right|^2$ and $\left|T_{p\pi n}(t)\right|^2$ to take care of the fact that the exchanged pion is not on the mass shell. The baryonic vertex factor after some convenient approximation is[58]:

$$\left[T_{p\pi n}\right]^2 = G^2\,|t|\,\frac{R_{p\pi n}^{-2} + (m_p-m_n)^2 - m_\pi^2}{R_{p\pi n}^{-2} + (m_p-m_n)^2 - t}$$

where $G^2/4\pi = 29.2$ and $R_{p\pi n}$ is a parameter which is defined as the radius of interaction. The other vertex $K^+\pi^- \to K^+\pi^-$ is overwhelmingly P-wave in the $K^*(892)$ region; so we have one parameter R_{K^*} for P-wave and hence

$$\left| T_{K^*\pi K} \right|^2 = M \left(\frac{q_t}{q}\right)^2 \frac{1 + R_{K^*}^2 q^2}{1 + R_{K^*}^2 q_t^2} \; q \, \sigma(M)$$

where $q(q_t)$ is the momentum of the exchanged pion taken on(off) shell in the $(K^+\pi^-)$ rest frame. $\sigma(M)$ is the on-shell $K^+\pi^-$ elastic scattering cross section and is parameterized by a P-wave Breit-Wigner distribution in the $K^*(892)$ region:

$$\sigma_{BW}^{P}(M) = \frac{4}{9} \frac{12\pi}{q^2} \cdot \frac{M_o^2 \, \Gamma^2(M)}{(M^2 - M_o^2)^2 + M_o^2 \Gamma^2(M)}$$

with energy dependent width $\Gamma(M)$. $M_o = 0.895$ GeV; $\Gamma_o = .055$ GeV. The factor 4/9 in the expression comes from the isospin $\frac{1}{2}$ component of the elastic scattering amplitude ($A(K^+\pi^- - K^+\pi^-)$).

In addition to the Durr-Pilkuhn form factors, a slowly varying dynamical form factor $G_W^2(t) = [(2.3 - m_\pi^2)/(2.3 + t)]^2$ suggested by Wolf[60] has also been used.

The results of the calculation with a constant background (estimated as $\sim$12% of the P-wave at its maximum) are shown in fig. 22b. The dash-dotted curve is obtained by using the values of the parameters R_{K^*} and $R_{p\pi n}$ as 1.3 and 2.7 $(GeV/c)^{-1}$ respectively[41]. As can be seen the model describes the data rather nicely in shape and magnitude near small $-t$ values — but at larger $-t$, the experimental distribution appears to fall off more rapidly with increasing production angle than the model would predict.

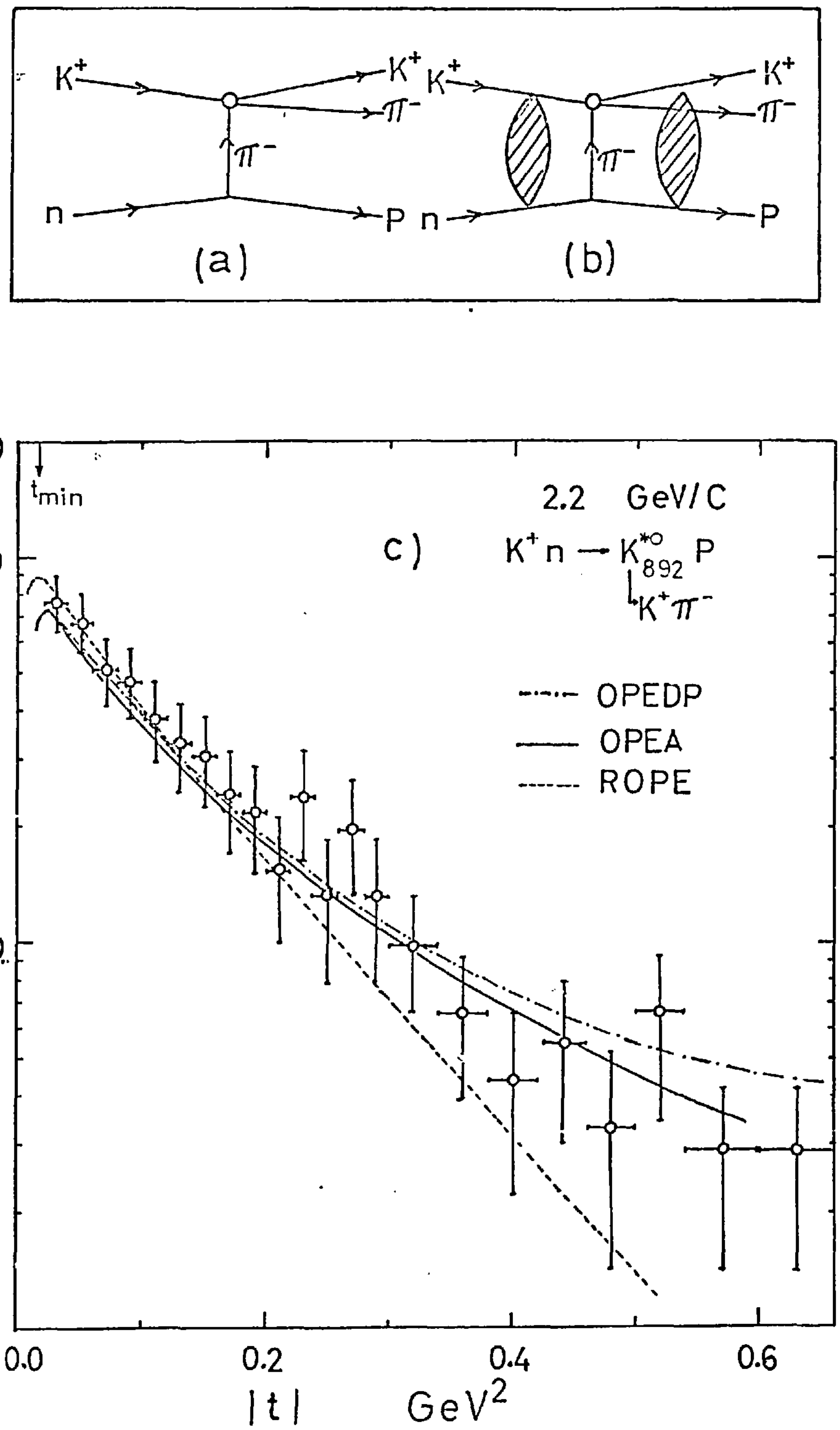

K+
K+
π−
π−
n
P
(a)
K+
K+
π−
π−
n
P
(b)
20
10
1.0
0.1
t_{min}
2.2 GeV/C
c)
$K^+ n \to K^{*0}_{892} P$
$\downarrow K^+ \pi^-$
OPEDP
OPEA
ROPE
dσ/dt (mb/GeV²)
0.0
0.2
0.4
0.6
|t| GeV²

FIGURE 22.

b) Absorption modified OPE model (OPEA):

Here we shall describe the production as well as decay of the resonance by means of the simple OPE model but with the inclusion of absorptive corrections. Since $K^+n \to K^+\pi^-p$ is a part of the total cross section of the initial K^+n particles, the competing channels will absorb part of the initial wavefunction — final state will also be similarly absorbed. We will see immediately how absorption substantially reduces the contribution of the low partial waves to the reaction, collimates significantly the momentum transfer distributions and reduces the overall cross section.

K. Gottfried and J.D. Jackson[61] presented a formulation which incorporates the absorptive effects in a simple phenomenological way. The basic assumption of the model is that the modified partial wave amplitude for the reaction $i \to f$ is

$$M^J_{fi} = (S^J_{ff})^{\frac{1}{2}} B^J_{fi} (S^J_{ii})^{\frac{1}{2}} \qquad (6\text{-}21)$$

where B is the unmodified Born amplitude for the reaction, S_{ii} and S_{ff} are the elastic scattering S-matrix elements in the initial and final states. The diagonal S-matrix elements are obtained from elastic scattering data. The choice of S is

$$S^J \simeq 1 - C.\ \mathrm{EXP}\left[-\gamma(J-\tfrac{1}{2})^2\right] \quad (= e^{2i\delta_1})$$

Here J is the total angular momentum and C measures the amount by which the lowest partial waves are absorbed and is given by

$$C_i = \sigma^i_T/4\pi B_i \quad ; \quad \gamma_i = \tfrac{1}{2}(k_i B_i^{\frac{1}{2}})^{-2}$$

where σ_T = total cross section; B_i = slope of the forward elastic angular distribution; k_i = centre of mass momentum. The choice of the final state parameters are[61]: $C_f = 1.0$, $\gamma_f = 0.75\ \gamma_i$ corresponding to total absorption of the lowest partial waves and a larger radius of interaction in the final state. The absorption parameters were calculated using the K^+p elastic scattering data (since no information is available on B from K^+n data) and the K^+n total cross section at 2.2 GeV/c : $C_i = 1.0$ and $\gamma_i = 0.18$. The values of coupling constants used are: $g^2_{K^*\pi^-K^+}/4\pi = 1.5$; $G^2_{p\pi^-n}/4\pi = 29.2$. With the values of the parameters given above, we have calculated using the exact summation of partial waves[62] the predictions of absorptive OPE contribution to the differential cross section and the density matrix elements of $K^+n \to K^{*o}(892)p$, $K^{*o} \to K^+\pi^-$ at 2.2 GeV/c.

The solid curve in fig. 22b shows that OPEA gives a good description of the momentum transfer distribution of the reaction under consideration. The density matrix elements in the Gottfried-Jackson frame are also plotted in fig. 23 with the prediction of the model. As can be seen it gives a reasonable description of ρ_{00} and Re ρ_{10} elements. But there is disagreement between the experimental values of $\rho_{1,-1}$ and the prediction particularly for $-t \gtrsim 0.15$ GeV^2. Similar disagreement has been reported by other experiment —- even the π-Regge-pole including A_2 exchange fails to agree with $\rho_{1,-1}$[43]. One should note here that $\rho_{1,-1}$ is the difference between the natural and unnatural parity exchange of spin $\geqslant 1$ contribution to K^{*o} — this fact along with the fact that $\rho_{1,-1}$ is compatible with zero when averaged over the whole

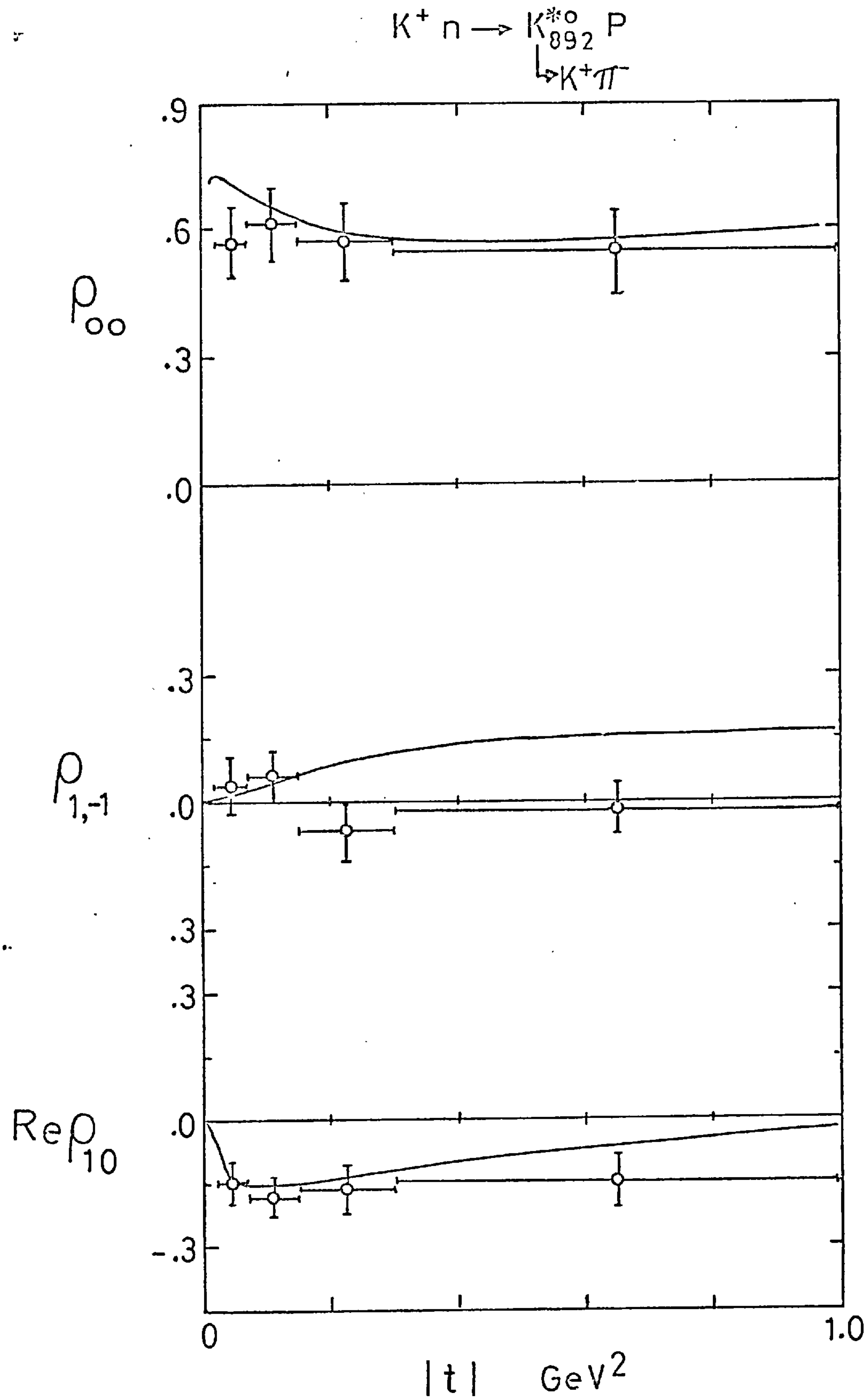

FIGURE 23.

t-range considered may indicate that the UNP and NP exchanges of spin $\geqslant 1$ occur in equal amounts i.e. in addition to A_2 (NP) there may be A_1 or B (UNP) exchange as well.

The apparent success of the OPEA model in describing the production and decay of $K^{*o}(892)$ is due to the fact that the unitarity is enforced by the complete elimination of the unphysical contribution in the low partial waves.

c) Reggeized OPE model (ROPE):

The differential cross section for pion exchange in $K^+n \to K^{*o}_{892}p$ $(K^{*o} \to K^+\pi^-)$ can also be written as[63]:

$$\frac{d\sigma}{dt} = \frac{2}{3}\,\frac{\pi}{sk^2}\,\frac{g^2}{4\pi}\,\frac{G^2}{4\pi}\cdot q_t^2\left[(m_n - m_p)^2 - t\right]\left|\frac{1}{t - m_\pi^2}\right|^2 \qquad (6\text{-}22)$$

The presence of branching factor 2/3 is due to the relative abundance of the $K^+\pi^-$ and $K^o\pi^o$ decay mode. s, k, q_t are defined as in section 6.4.4a.

We Reggeize the above expression by replacing the pion propagator $1/(t-m_\pi^2)$ by[64]:

$$\pi\alpha'(0)\,\frac{1 + e^{-i\pi\alpha}}{2\,\mathrm{Sin}\,\pi\alpha}\,\frac{(1+2\alpha)(1+2\alpha/3)\,\Gamma(\alpha+\frac{1}{2})}{\Gamma(\frac{1}{2})\,\Gamma(\alpha+1)}\left(\frac{s-u}{2s_o}\right)^{\alpha}$$

where the exchanged pion trajectory is lying on an evasive Regge trajectory. The trajectory is $\alpha=\alpha'(0)(t-m_\pi^2)$ with $\alpha'=1.1$ $(\mathrm{GeV/c})^{-2}$ and $2s_o = 1.08\ \mathrm{GeV}^2$.

The result of the calculation using the model is shown as a dashed curve in fig. 22c. The prediction of the model is seen to be too steep compared to the data. This rather poor agreement specially at larger -t shows that the Regge pole model, which has met with some success at higher energies, is not expected to be so good at lower energies.

6.4.5 Comparisons between the reactions $K^+n \to K^{*0}(892)p$ and $K^-p \to \overline{K^{*0}}(892)n$:

The reactions $K^+n \to K^{*0}(892)p$ $(K^{*0} \to K^+\pi^-)$ and $K^-p \to \overline{K^{*0}}(892)n$ $(K^{*0} \to K^-\pi^+)$ are related by line reversal and only T=1 object/objects contribute in the t-channel. Hence it is interesting to compare some properties of these two reactions.

In fig. 24 we compile the cross section of the above two reactions at various incident beam momenta and in table XII the values of slopes, B of $d\sigma/dt$ distributions of the two reactions at small $-t$ are also shown. Although a direct comparison of slopes of two different K^{*0} reactions at different energies is impossible because of the difference in the t-range used for determining B, but nevertheless it is still useful for the purpose of rough comparisons. From a quick look at the table, it is found that K^{*0} is steeper than $\overline{K^{*0}}$. This is quite surprising because if only π-meson exchange occurs (and the evidence is that π is dominant) then their cross sections should be of equal magnitudes. But if absorption is considered, then the lowest partial waves will be absorbed with the result that the flatter parts of the $d\sigma/dt$ distributions are decreased in size — and hence $d\sigma/dt$ distributions peak more sharply forward. We expect $K^-p \to \overline{K^{*0}}(892)n$ to be absorbed more because the initial K^-p has total cross section bigger than the K^+n cross section. So one would have expected

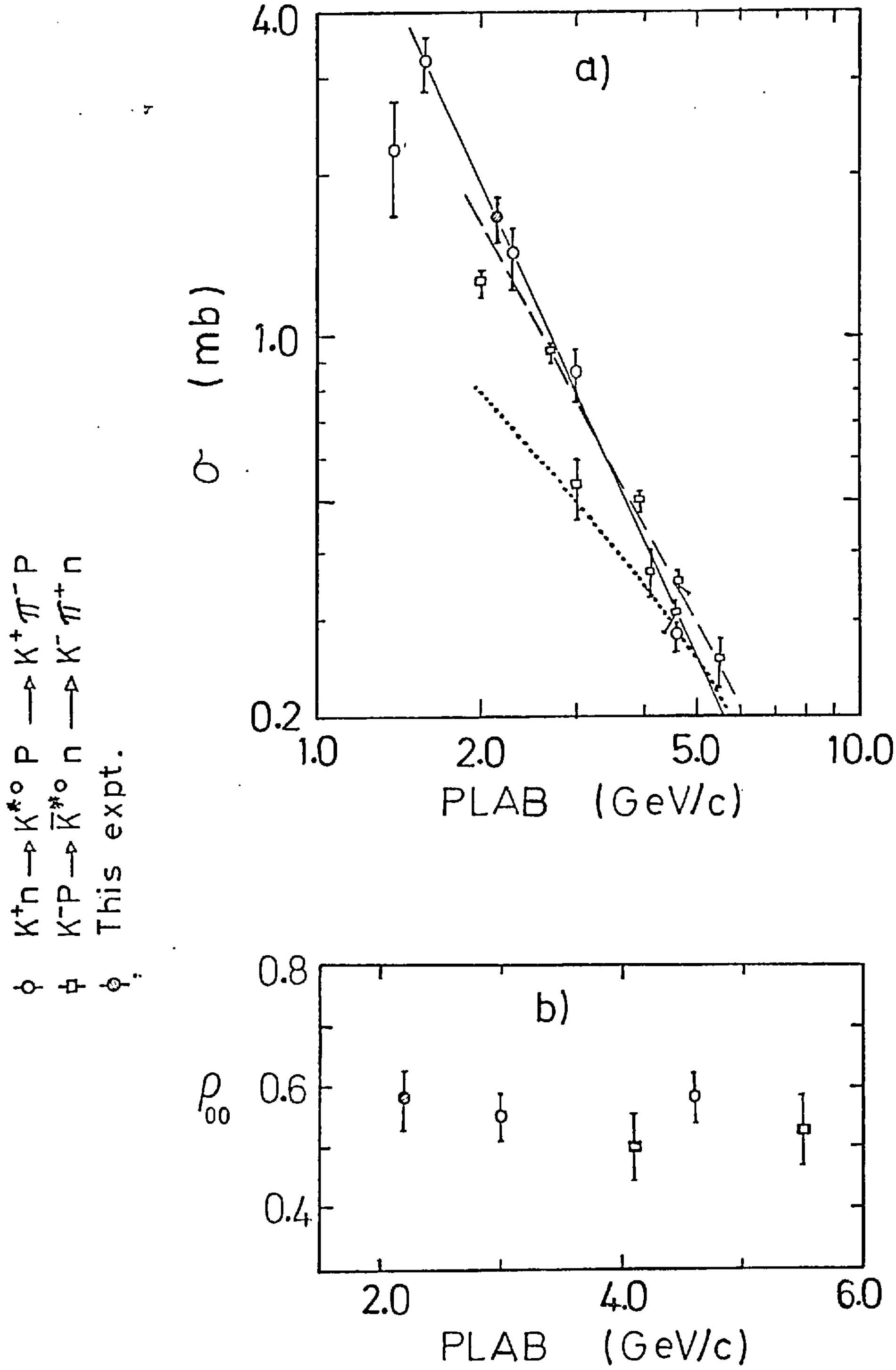

a)
b)
σ (mb)
4.0
1.0
0.2
1.0
2.0
5.0
10.0
PLAB (GeV/c)
ρ_{00}
0.8
0.6
0.4
2.0
4.0
6.0
PLAB (GeV/c)
$K^+n \rightarrow K^{*o} P \longrightarrow K^+\pi^- P$
$K^-P \rightarrow \bar{K}^{*o} n \longrightarrow K^-\pi^+ n$
This expt.

FIGURE 24.

Table XII. Survey of slopes of $d\sigma/dt$ distributions.

Reactions	Momentum (GeV/c)	t-interval (GeV^2)	Slope, B (GeV^{-2})	Reference
$K^+n \to K^{*o}_{892}p$, $\hookrightarrow K^+\pi^-$	2.0	.04 - .4	$7.09 \pm .27$	65
	2.2	.02 - .4	$7.1 \pm .4$	This Exp.
	3.0	.04 - .32	$8.1 \pm .7$	41,42
	4.6	$.02 \leq t' \leq .3$	$9.2 \pm .5$	42
	9.0	.02 - .4	7.8 ± 1.4	43,42
	12.0	.025- .3	$8.8 \pm .7$	44,42
$K^-p \to K^{*o}_{892}n$, $\hookrightarrow K^-\pi^+$	2.0	.04 - .4	$4.66 \pm .15$	65
	3.9	.01 - .4	$5.5 \pm .3$	Calc. by the author using data of refs. [46,52]
	4.6	.005- .4	$5.3 \pm .4$	
	5.5	.003- .38	$4.9 \pm .5$	
	10.1	$.0 \leq t' \leq .4$	$6.1 \pm .5$	66
	14.3	.00 - .4	7.0 ± 1.1	67

$K^-p \to K^{*o}(892)n$ to have a smaller cross section and a larger slope than $K^+n \to K^{*o}(892)p$.

The solid line in fig. 24a is obtained using $\sigma = 8.6 \times P_{lab}^{-2.15}$ and the other two curves are the predictions of the absorption modified pion exchange calculations for the two reactions. These calculations roughly agree with the data and that the experimental $\bar{K}^{*o}$ cross sections lie below that of K^{*o} . This difference becomes smaller and smaller as the energy increases. In fig. 24b we show the variation of the density matrix element ρ^J_{oo} as a function of incident beam momentum for the two reactions. They are same within experimental errors.

Now in order to understand the smaller slopes of $\bar{K}^{*o}$ momentum transfer distribution relative to that of K^{*o}, we compare in table XIII, the slopes at small $-t$ of $d\sigma/dt$, $\rho^J_{oo}d\sigma/dt$ and $\rho^H_{oo}d\sigma/dt$ of K^{*o}, $\bar{K}^{*o}$ and ρ^o (ρ^o in $\pi^- p \to \rho^o n$ is an example of typical OPE process) productions. From the table one can see that the small slope of $d\sigma/dt$ distribution of $\bar{K}^{*o}$ compared to that of K^{*o} is associated with the dominance of $\rho_{11}d\sigma/dt$ at large $-t$. G.C. Fox et al.(52) recently explained this difference in shape of K^{*o} and $\bar{K}^{*o}$ production in terms of interference between strong absorptive correction to the π-Regge pole and a ρ-Regge pole. Here π-ρ interference contribution is destructive for K^{*o} and constructive for $\bar{K}^{*o}$ production.

Table XIII. Comparison of slopes, B of $d\sigma/dt$, $\rho^J_{oo}d\sigma/dt$ and $\rho^H_{oo}d\sigma/dt$ distributions for K^{*o}_{892}, $\bar{K}^{*o}_{892}$ and ρ^o_{765} productions respectively.

Distribution	SLOPES, B (at small -t)			
	ρ^o	K^{*o}		$\bar{K}^{*o}$
	8.8 GeV/c ref. [52]	2.2 GeV/c This Exp.	4.6 GeV/c ref. [41] (t')	5.5 GeV/c ref. [52]
$\frac{d\sigma}{dt}$	$10.9 \pm .5$	$7.1 \pm .4$	$9.2 \pm .5$	$4.75 \pm .5$
$\rho^J_{oo}\frac{d\sigma}{dt}$	$10.9 \pm .6$	$7.2 \pm .8$	$9.8 \pm .7$	$7.40 \pm .8$
$\rho^H_{oo}\frac{d\sigma}{dt}$	13.6 ± 1.0	$8.2 \pm .9$	$10.9 \pm .7$	12.10 ± 1.0

6.4.6 K^* production from the T=0 K^*N state:

Using the individual $K^*(892)$ cross section measured in this experiment, we obtain the total cross section for K^* production from the isospin zero K^*N state from:

$$\sigma_0(K^+N\to K^*N) = 3\left[\sigma(K^+n\to \underset{\hookrightarrow K^+\pi^-}{K^{*o}}p)+\sigma(K^+n\to \underset{\hookrightarrow K^o\pi^+}{K^{*+}}n)-\tfrac{1}{2}\sigma(K^+p\to \underset{\hookrightarrow K^o\pi^+}{K^{*+}}p)\right] \quad (6\text{-}23)$$

The cross section thus calculated at 2.2 GeV/c is $\sigma_0 = 5.7\pm.7$ mb. The same relation (6-23) applies to differential distributions as well and hence will be used to obtain the production and decay angular distributions of the K^* formed from the T=0 state. In fig. 25a we show the $d\sigma/dt'$ distribution at 2.2 GeV/c. Comparing this with one of the component reactions $K^+n\to K^{*o}p$, we observe that $K^+n\to K^{*o}(K^+\pi^-)p$ dominates the data but the distribution of K^* from the T=0 state is found to be more forward peaked than any of the other reactions. This can also be seen by fitting the experimental $d\sigma'/dt'$ distributions between $0 \leq |t'| \leq .42$ GeV^2 to the form:

$$\frac{d\sigma'}{dt'} = A\, e^{Bt'} \quad \text{where} \quad \begin{array}{l} \sigma' = \sigma(K^+n\to \underset{\hookrightarrow K^+\pi^-}{K^{*o}}p) \\ \sigma' = \frac{1}{3}\sigma(K^+N\to K^*N) \end{array}$$

The fitted values of A and B for the two distributions are $A=8.0\pm1.1$ mb/GeV^2, $B=7.1\pm.6$ GeV^{-2} and $A=9.9\pm1.2$ mb/GeV^2, $B=7.8\pm.8$ GeV^{-2} respectively.

In fig. 25b,c we present the decay angular distributions ($\cos\theta_J$ and Φ) for the K^* from the T=0 state. The Cosine of the Jackson angle is mainly $\cos^2\theta_J$ and Φ (within errors) is roughly consistent with being flat. The rather large value

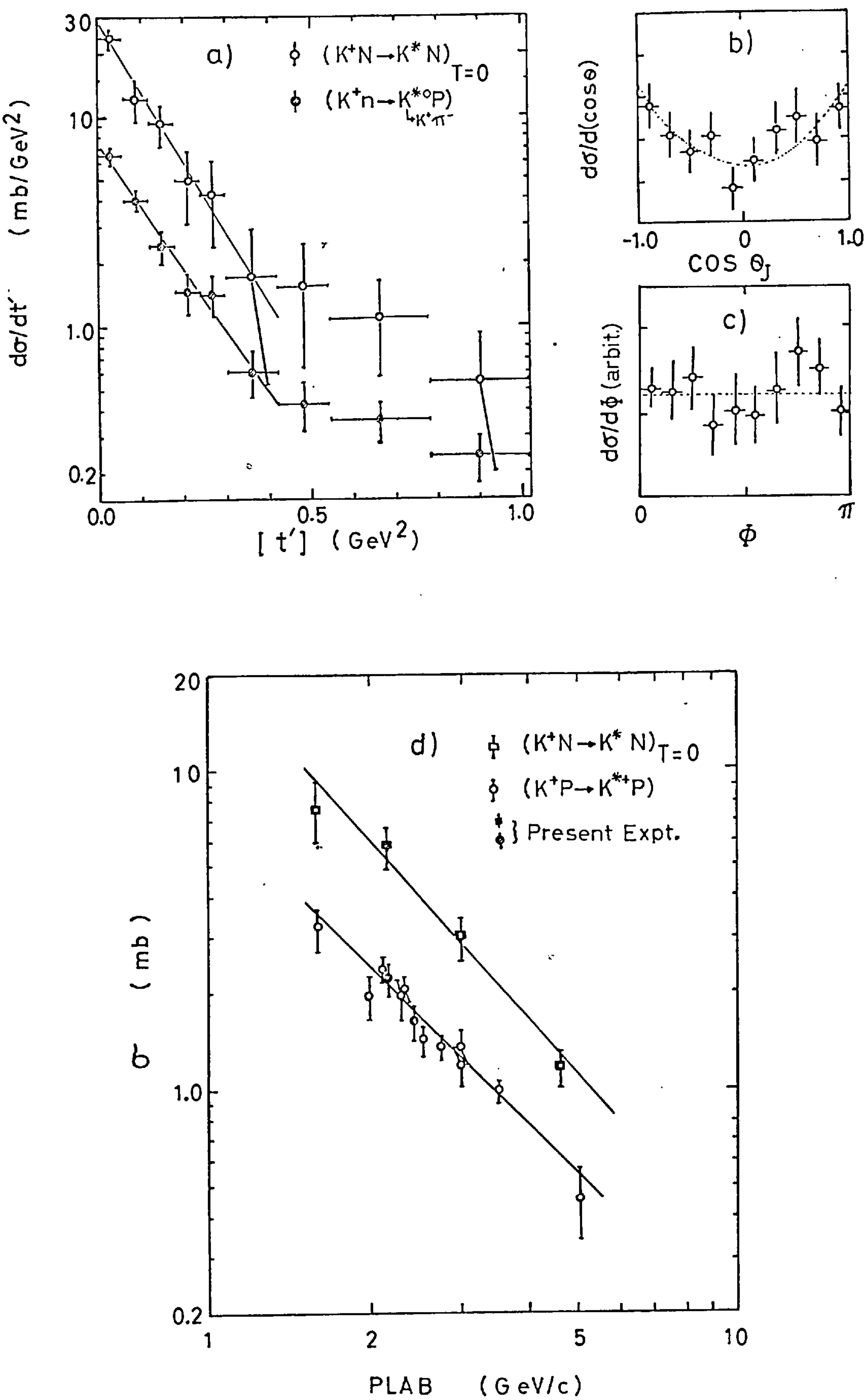

a)
(K⁺N→K* N)T=0
(K⁺n→K*°P) ↳K⁺π⁻
dσ/dt′ (mb/GeV2)
[t′] (GeV2)
b)
dσ/d(cosθ)
COS θJ
c)
dσ/dΦ (arbit.)
Φ
d)
(K⁺N→K* N)T=0
(K⁺P→K*⁺P)
} Present Expt.
σ (mb)
PLAB (GeV/c)

FIGURE 25.

of ρ_{00} = .64 (averaged over the entire t region) and all the above features of this K^* production and decay compared to pion dominant K^{*o} production indicates that we have purer pion exchange here than in the component K^{*o} production. The observation was also made at lower energies[10].

In fig. 25d we show σ_0 as a function of incident beam momentum. The data points at 3.0 and 4.6 GeV/c have been calculated using the cross sections of ref. [41,42] and that at 1.585 GeV/c has been taken from ref. [10]. The errors on the cross sections are increased (by ~50%) to allow for the uncertainties in the deuterium cross sections. For comparison the total K^* cross sections from the T=1 K^+p state (σ_1) are also shown in the same figure. This comparison is interesting because the production mechanisms of these two reactions are quite different — the T=1 production is mainly through vector (ω) exchange whereas the T=0 production, as noted above, is due primarily through pion exchange. By fitting each set of cross sections to the form $\sigma = A\, P_{lab}^{-n}$, we get A = 7.6±1.1 mb, n= 1.64±.15 (χ^2/ND = 6.2/11) for σ_1 whereas the corresponding numbers for σ_0 are (22.8±1.2) mb and (1.92±.17) (χ^2/ND = 3.8/2) respectively. Inspite of the limited number of data points for σ_0, it can be seen that in the energy range considered σ_0 falls faster than σ_1 as expected and thus contradicts the earlier observation made by Hirata et. al.[10] that they have roughly the same energy dependence. But it should be pointed out here that more data for σ_0 are needed to arrive at a strong conclusion about the energy dependence. Our two more new data points for σ_0 at 2.45 and 2.7 GeV/c will certainly help towards this end.

6.5 Δ^{++} production and decay:

The isospin 3/2 $\Delta(1230)$ can only be produced abundantly from the T=1 KN initial state. We have some production of F-wave $N^*(1688)$ in the $K^+n \to K^0\pi^+n$ final state, but the small number of $N^*(1688)$ events do not permit an useful analysis. So we consider here only $\Delta^{++}(1230)$ events produced in the reaction $K^+p \to K^0 \Delta^{++} \to K^0\pi^+p$ where the events are selected with $(p\pi)$ effective mass between 1.18 and 1.28 GeV.

a) Production angular distribution:

The production angle (measured with respect to the incoming proton) is defined in the same manner as discussed in section 6.4 and the $K^+p \to K^0 \Delta^{++}$ events in the peak region are used to define the shape of the angular distribution. The experimental production angular distributions are shown in fig. 26. The smooth lines on the plots represent the curves obtained when the data were fitted with Legendre polynomials of order $n_{max} = 4$ at both momenta. The normalized coefficients obtained by the method of moments are given in table XIV and

Table XIV. Legendre polynomial coefficients for $\Delta^{++}(1230)$.

A_n/A_o	P = 2.2 GeV/c	P = 2.45 GeV/c
A_1/A_o	1.83 ± 0.13	1.91 ± 0.13
A_2/A_o	1.73 ± 0.20	1.90 ± 0.20
A_3/A_o	$.56 \pm 0.29$	$.99 \pm 0.30$
A_4/A_o	$-.42 \pm 0.34$	$.18 \pm 0.33$

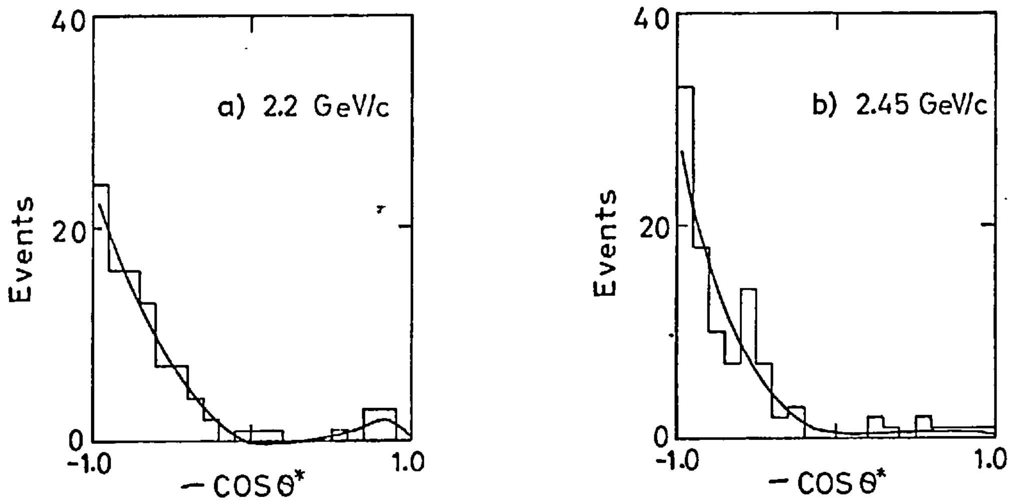

FIGURE 26.

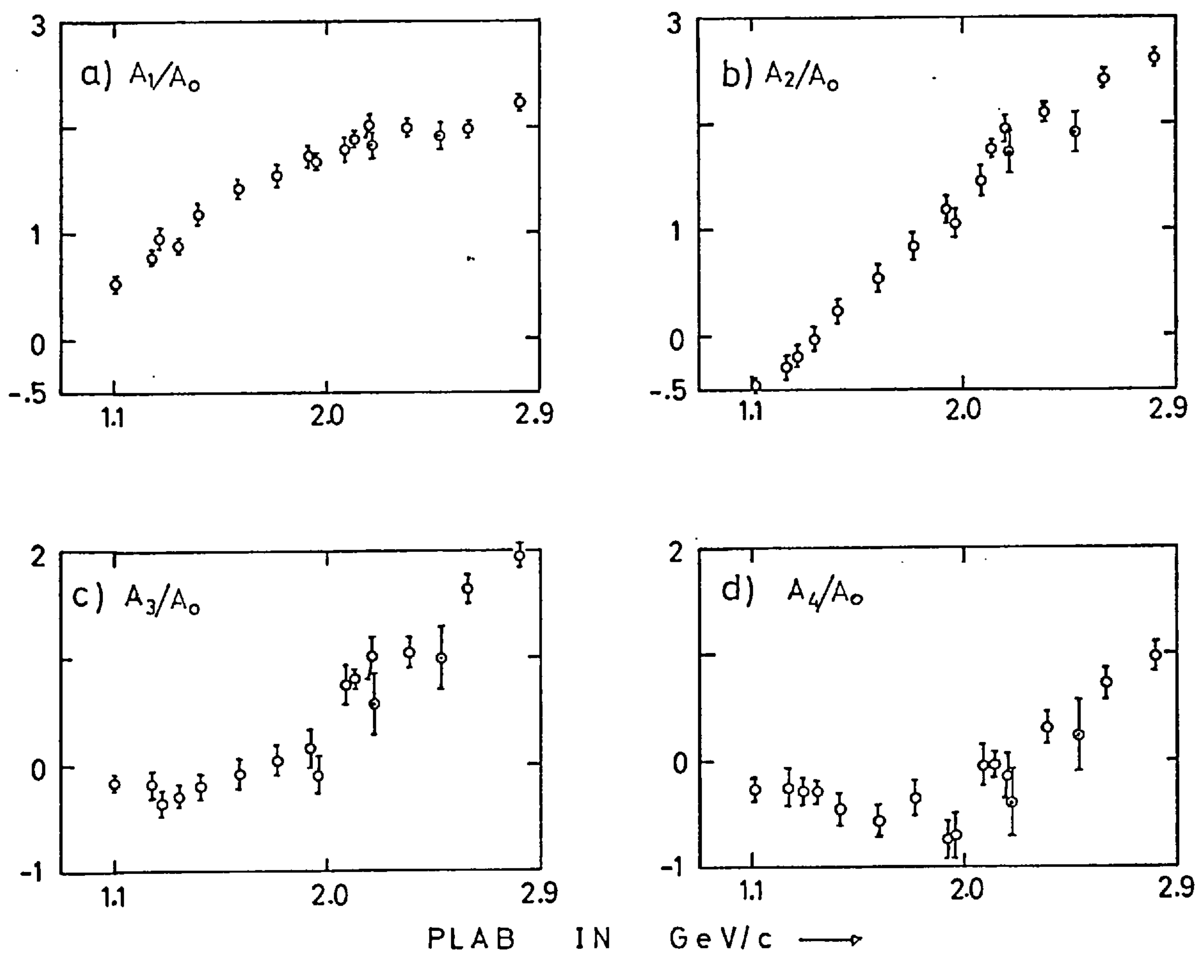

FIGURE 27.

also shown in fig. 27 together with the data available at nearby energies. The momentum variation of the coefficients is found to be smooth over the energy region although the A_4 coefficient has a slight kink at about 2 GeV/c.

<u>dσ/dt' distribution</u>:

In fig. 28 we show the momentum transfer distributions for the $\Delta^{++}(1230)$. As defined before $|t'| = |t-t_m|$; $|t_m|$ is the minimum kinematically allowed value of $|t|$. We observe that for $|t'|$ close to zero, the differential cross section decreases with decreasing $|t'|$. This apparent turnover does not seem to be due to the scanning bias as we do not expect it to happen for even the forward most Δ^{++} events since the other outgoing tracks K^0 and π^+ are always obvious even when the proton track is not. Similar vanishing of dσ/dt' (in fact more rapid) has also been observed by other experiments using hydrogen bubble chamber[39,69,70].

We have fitted the differential cross section to a function of the form $A\,e^{B|t'|}$. The fitted values for A and B at 2.2 GeV/c for $|t'| \leq 1.0$ GeV^2 are; $A = 3.5 \pm 1.2$ mb/GeV^2, $B = 2.4 \pm .5$ GeV^{-2}. The data at 2.45 GeV/c can not be fitted to a single function of the form $A\,e^{B|t'|}$ over the whole $|t'|$ region because there seems to be a change of slope at large $|t'|$. A fit upto $|t'| = .55$ GeV^2 gave $A = 2.6 \pm 1.2$ mb/GeV^2 and $B = 3.5 \pm .7$ GeV^{-2}.

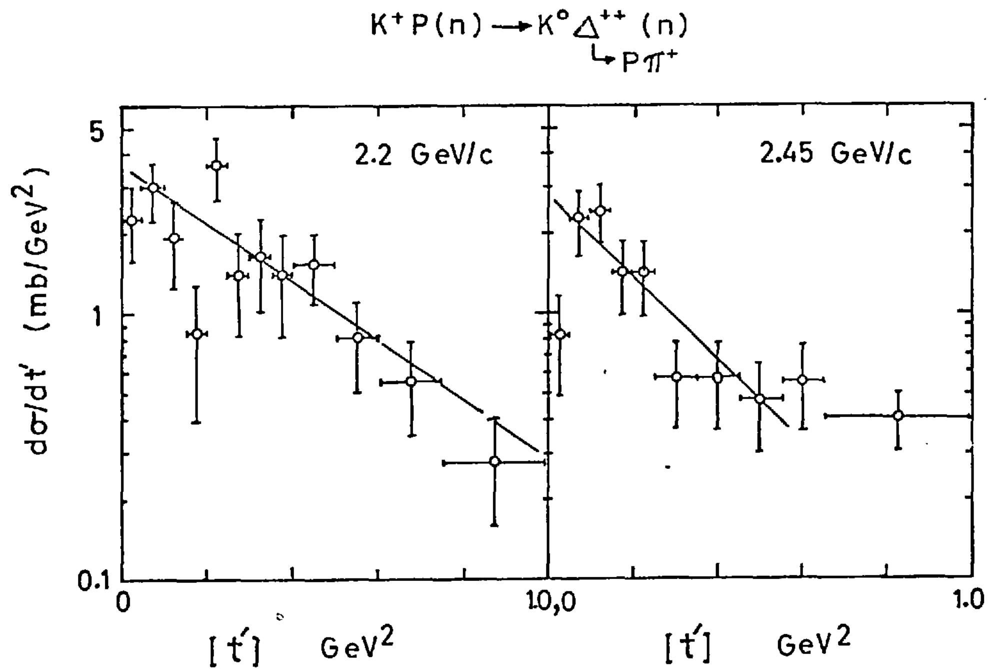

FIGURE 28

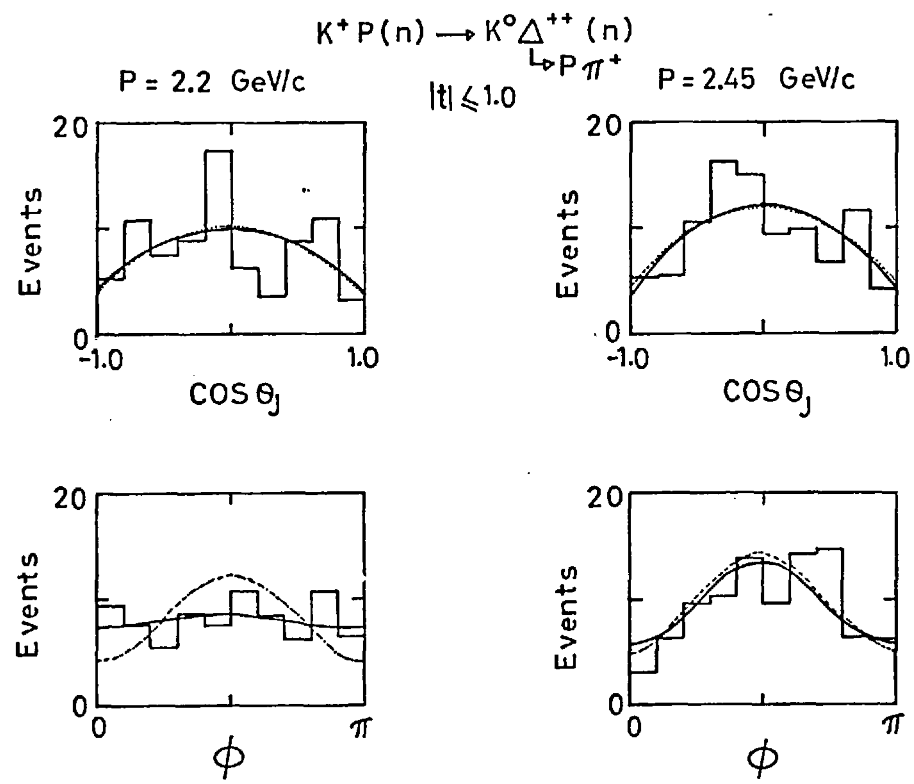

FIGURE 29.

b) Δ^{++} decay distribution:

In fig. 29 we show the $\text{Cos}\Theta$ and Φ distributions of the $\Delta^{++}(1230)$. The problem of the $K^*-\Delta$ overlap region has been tackled by the mass conjugation technique (described earlier) to simulate Δ^{++} production in the overlap region.

The Φ distribution is again shown folded in accordance with the parity-imposed symmetry of the decay. The solid curves superimposed both on the $\text{Cos}\Theta$ and Φ distributions are obtained with the measured density matrix elements using the method of moments.

In the absence of knowledge of the spin alignments of the target and decay protons, it is not possible to determine the seven independent parameters of the Δ^{++} density matrix, we can only measure ρ_{33}, Re $\rho_{3,-1}$ and Re ρ_{31} from the decay angular distribution. The decay distribution has the form:

$$W(\text{Cos}\Theta,\Phi) = \frac{3}{4\pi}\left[\frac{1}{6}(1+4\rho_{31})+\tfrac{1}{2}(1-4\rho_{33})\text{Cos}^2\Theta-\frac{2}{\sqrt{3}}\,\text{Re}\rho_{3,-1}\text{Sin}^2\Theta\text{Cos}2\Phi - \frac{2}{\sqrt{3}}\,\text{Re}\rho_{31}\ \text{Sin}2\Theta\ \text{Cos}\Phi\right] \tag{6-24}$$

The $\text{Cos}\Theta$ and Φ projections are:

$$W(\text{Cos}\Theta) = \frac{1}{4}\left[(1+4\rho_{33})+(3-12\rho_{33})\ \text{Cos}^2\Theta\right]$$

$$W(\ \Phi\ ) = \frac{1}{2\pi}\left[1+\frac{4}{\sqrt{3}}\,\text{Re}\rho_{3,-1}-\frac{8}{\sqrt{3}}\,\text{Re}\rho_{3,-1}\ \text{Cos}^2\Phi\right]$$

The density matrix elements obtained by the method of moments are shown in table XV. The upper entries correspond to the mass conjugated data whereas/lower ones correspond to the raw data only.

Table XV. Δ^{++} density matrix elements in the Jackson system (P-wave).

Momentum (GeV/c)	-t interval (GeV^2)	ρ_{33}	Re $\rho_{3,-1}$	Re ρ_{31}
2.2	.00-.20	.409±.096 .406±.090	.047±.103 .071±.094	-.072±.095 -.105±.090
	.20-.40	.303±.110 .386±.093	-.107±.115 -.023±.118	.145±.131 .123±.105
	.40-1.0	.368±.076 .477±.067	.151±.128 .216±.111	.028±.109 .032±.080
	.00-1.0	.362±.056 .426±.048	.028±.068 .094±.063	.029±.066 .021±.054
	all -t	.348±.055 .404±.048	.012±.065 .096±.060	.004±.065 -.006±.052
2.45	.00-.20	.425±.094 .420±.071	.020±.085 .162±.081	-.077±.091 -.079±.075
	.20-.40	.090±.091 .175±.100	.256±.120 .305±.109	-.135±.148 .037±.125
	.40-1.0	.503±.063 .466±.069	.279±.089 .278±.095	-.053±.070 -.077±.072
	.00-1.0	.402±.051 .397±.046	.177±.057 .230±.056	-.076±.054 -.059±.049
	all -t	.431±.047 .419±.042	.166±.055 .221±.051	-.065±.050 -.054±.044
S-S prediction		.375	.216	0.0

Stodolsky and Sakurai[71] developed a model using ρ-photon analogy to describe $K^+p \rightarrow K^0 \Delta^{++}(1230)$. Here Δ^{++} production is assumed to occur predominantly via ρ-exchange where the vertex $N\rho\Delta^{++}$ is treated in analogy to the photo-production vertex $N\gamma\Delta$. The latter reaction is known to be dominated by the M1 magnetic dipole transition and the Δ thus produced has only the spin orientations $m = \pm\frac{1}{2}$ normal to the production plane. Translated to the Jackson system the Stodolsky-Sakurai (S-S) predictions on the density matrix elements are shown in table XV. The experimental values of ρ_{33} at both momenta agree reasonably well with the value of .375 for pure ρ-exchange as calculated in the model. Also the observed values of Re ρ_{31} are zero within errors and are compatiable with the prediction. The predicted value of the element Re $\rho_{3,-1}$ shows rough agreement with the data at 2.45 GeV/c but does not agree with the data at 2.2 GeV/c except at high $|t|$ ($|t| \geqslant 0.4$ GeV^2). No further conclusive comments can be made on this element because of the large errors on the experimental Re $\rho_{3,-1}$ points.

The dotted lines shown on the $\text{Cos}\theta_J$ and Φ distributions (fig. 29) are the predictions of the S-S pure ρ-exchange model as normalized to the total number of events in the distributions. These comparisons also show that the model is in reasonable agreement with the Δ^{++} decay angular distributions with the exception of Φ distribution at 2.2 GeV/c.

REFERENCES

1. R.L. Cool et al., Phys. Rev. Letts., 17, 102, (1966)
2. R.J. Abrams et al., Phys. Rev. Letts., 19, 259, (1967)
3. R.W. Bland et al., Phys. Rev. Letts., 18, 1077, (1967)
4. S. Goldhaber et al., Phys. Rev., 142, 913, (1966)
5. F. Bomse et al., Phys. Rev., 158, 1281, (1967)
6. M. Ferro-Luzzi et al., Nuovo Cimento, 36, 1101, (1965)
7. S. Goldhaber et al., Phys. Rev. Letts., 15, 737, (1965)
8. I. Butterworth, Proposal No. 56 RHEL.
9. J.M. Brunet et al., Nucl. Phys., B37, 114, (1972)

10. P.H. Lewis et al., Submitted to Nucl. Phys.

10. A.A. Hirata et al., Nucl. Phys., B33, 525, (1971)
    A.A. Hirata. Ph.D. Thesis, UCRL-20248 (unpublished).
11. G. Giacomelli et al., Nucl. Phys., B37, 577, (1972).
12. G. Thompson. Ph.D. Thesis, RHEL Report HEP/T/13(1971).
13. CERN T.C. Program Library-THRESH write-up. For other program write-ups consult the T.C. Program Librarian.
14. R.C. Strand, Brookhaven internal report G-34 (1963).
15. J.M. Howie, FSD bubble chamber program (full guidance) FGFILT B040 (1969).
16. H. Atherton et al., ANL-7515 (1968).
    A.K.M.A. Islam, I.C. internal physics note (3-3-71).
17. P. Duinker, CERN-DD/DH/69/20.
18. I.O. Skillicorn, Preliminary report on bubble density measurements in the 80" bubble chamber using MK.IIHPD. Brookhaven internal report.
19. G.F. Chew, Phys. Rev., 80, 196, (1950).
    G.F. Chew and G.C. Wick, Phys. Rev., 85, 636, (1952).
20. I.J. McGee, Phys. Rev., 151, 772, (1966).

21. L. Hülthen and A. Sugawara, Handbuch der Physik, Vol. 34, Springer-Verlag, Berlin, 1957.

22. M. Moravcsik, Nucl. Phys.,1, 113, (1958).

23. R.L. Glückstern and H.A. Bethe, Phys. Rev., 81,761,(1951).

24. G. Fäldt and T.E.O. Ericson, Nucl. Phys., B8, 1, (1968).

25. G. Lynch, UCRL-19844 (preprint).

26. R.J. Glauber, Phys. Rev., 100, 242, (1955).

27. V. Franco and R.J. Glauber, Phys. Rev., 142, 1195,(1966).

28. R.L. Cool et al., Phys. Rev., 1, 1887, (1970).

29. E. Flaminio et al., Compilation of cross sections. CERN/HERA 70-4.

30. B.M. Schwarzchild, Ph.D. Thesis,UCRL-17572 (unpublished).

31. G. Benson, University of Michigan Report COO-1112-4(1966). Also see ref. 30 .

32. R.G. Glasser, Naval Research Lab. Report-5667,p15, (1961).

33. I. Shmushkevich, Dokl. Akad. Nauk., SSSR 103, 235, (1955). Also see ref. 9 .

34. J.D. Jackson, Nuovo Cimento, 34, 1644, (1964).

35. F. James and M. Ross, CERN MINUIT long write-up (10.6.71).

36. R. Dolen et al., Phys. Rev., 166, 1768, (1968).

37. J.G. Asbury et al., Phys. Rev. Letts., 23, 194, (1969).

38. S.C. Loken et al., CALT-68-334, Sub. to Phys. Rev.

39. E. Lesquoy et al., Paper submitted to the Int. Conf. on elementary particles, Amsterdam (1971).

40. See Rapporteur's talk by D.R.O. Morrison. p-237, Proc. of the Lund Int. Conf. on elementary particles (1969).

41. G. Bassompierre et al., Nucl. Phys., B16, 125, (1970).

42. K. Buchner et al., Nucl. Phys., B45, 333, (1972).

43. D. Cords et al., Phys. Rev., 4, 1974, (1971).

44. D.A. Lissauer. Ph.D. Thesis, UCRL-20644 (1971).

45. J. Goldberg et al., Phys. Letts., 30B, 434, (1969).

46. M. Aguilar-Benitez et al., Phys. Rev. Letts., 26, 466(1971)
M. Aguilar-Benitez et al., Phys. Rev., 4, 2583, (1971).

47. For references see R. Mercer et al., Nucl. Phys., B32, 381, (1971).

48. P.E. Schlein. Proc. of the Conf. on ππ and Kπ interactions, Argonne National Laboratory, p-446, (1969).

49. T.G. Trippe et al., Phys. Letts., 28B, 203, (1968).

50. For example see a recent review by T.G. Trippe, LBL-763 preprint (December, 1971).

51. D. Cords et al., Purdue University Report, COO-1428-308 (1972).

52. G.C. Fox et al., Phys. Rev., 4, 2647, (1971). Also see Argonne National Lab. Report ANL/HEP 7143.

53. M.G. Doncel et al., Ecole d'Ete de Gif-Sur-Yvette (1970).

54. P. Eberhard, M. Pripstein, Phys. Rev. Letts.,10, 351(1963).

55. B. Sakita and K.C. Wali, Phys. Rev., 139, 1355, (1965).

56. J.B. Bronzan, F.E. Low, Phys. Rev. Letts., 12, 522, (1964).

57. J.P. Ader et al., Nuovo Cimento, 56A, 952, (1968).

58. H.P. Dürr and H. Pilkuhn, Nuovo Cimento, 40A, 899, (1965).

59. H. Pilkuhn, CERN Yellow Report 65/25 (Vol. 1).

60. G. Wolf, Phys. Rev. Letts., 19, 925, (1967).

61. K. Gottfried and J.D. Jackson, Nuovo Cimento, 33, 735, (1964). J.D. Jackson et al., Phys. Rev., 139, 428, (1965).

62. R. Keyser, CERN Report DD/CO/66/3.

63. J.D. Jackson and H. Pilkuhn, Nuovo Cimento,33,906, (1964).

64. G.S. Abrams and U. Maor, Phys. Rev. Letts,25,621,(1970).

65. R. Poster et al., Paper submitted to the International Conf. on elementary particles, Amsterdam (1971).

66. M. Deutschmann et al., Nucl. Phys., B36, 373, (1972).

67. B. Chaurand et al., Phys. Letts., 38B, 253, (1972).

68. F. Schweingruber et al., Phys. Rev., 166, 1317, (1968).

69. G. Neuhofer et al., Phys. Letts., 39B, 271, (1972).

70. W. De Baere et al., Paper submitted to 14th International Conf. on High Energy Physics, Kiev (1970).

71. L. Stodolsky and J.J. Sakurai, Phys. Rev. Letts., 11, 90, (1963).

ACKNOWLEDGEMENTS

I wish to express my gratitude to Prof. C.C. Butler, FRS for extending to me the research facilities of the physics department; sincere appreciation to Prof. I. Butterworth, Prof. S.J. Goldsack, Dr. S.L. Baker and also to many other members of the department for their teaching and encouragements.

I would like to thank my research supervisor, Dr. D.B. Miller for his continued interest in the work and for reading the manuscript.

Thanks are also due to my collegue Robert Orr who shared my enthusiasm throughout the course of the work and lately to Geoff May with whom I had many useful arguments.

The efforts of the Rutherford Laboratory bubble chamber crews and the skillful works of the scanning and measuring staffs of our group are also gratefully acknowledged.

I also like to thank the department of physics for a research assistantship from January to September, 1972 and to the University of Rajshahi for granting me study leave to enable me to carry out the work.

Last, but by no means least, many thanks to my parents and my wife Shamsunnahar for all their moral support.